Particle surface roughness improves colloidal stability of pressurized pharmaceutical suspensions

Hui Wang, David S. Nobes, Reinhard Vehring*

Department of Mechanical Engineering, University of Alberta, Edmonton, Alberta, Canada

* Corresponding author. Tel.: +1 780 492 5180; Fax: +1 780 492 2378

Email: reinhard.vehring@ualberta.ca

University of Alberta, Department of Mechanical Engineering, 10-269 Donadeo Innovation Centre for Engineering, Edmonton, Alberta, Canada T6G 1H9

Suggested running head: Particle roughness improves pMDI colloidal stability

Abstract

Purpose: The effects of particle size and particle surface roughness on the colloidal stability of pressurized pharmaceutical suspensions were investigated using monodisperse spray-dried particles.

Methods: The colloidal stability of multiple suspensions in the propellant HFA227ea was characterized using a shadowgraphic imaging technique and quantitatively compared using an instability index. Model suspensions of monodisperse spray-dried trehalose particles of narrow distributions (*GSD* < 1.2) and different sizes (*MMAD* = 5.98 µm, 10.1 µm, 15.5 µm) were measured first to study the dependence of colloidal stability on particle size. Particles with different surface rugosity were then designed by adding different fractions of trileucine, a shell former, and their suspension stability measured to further study the effects of surface roughness on the colloidal stability of pressurized suspensions.

Results: The colloidal stability significantly improved ($p < 0.001$) from the suspension with 15.5 µm-particles to the suspension with 5.98 µm-particles as quantified by the decreased instability index from 0.63 ± 0.04 to 0.07 ± 0.01, demonstrating a strongly size-dependent colloidal stability. No significant improvement of suspension stability ($p > 0.1$) was observed at low trileucine fraction at 0.4% where particles remained relatively smooth until the surface rugosity of the particles was improved by the higher trileucine fractions at 1.0% and 5.0%, which was indicated by the substantially decreased instability index

from 0.27±0.02 for the suspensions with trehalose model particles to 0.18±0.01 ($p < 0.01$) and 0.03±0.01 ($p < 0.002$) respectively.

Conclusions: Surface modification of particles by adding shell formers like trileucine to the feed solutions of spray drying was demonstrated to be a promising method of improving the colloidal stability of pharmaceutical suspensions in pressurized metered dose inhalers.

Keywords: Suspension stability, shadowgraphic imaging, particle formation, monodisperse spray drying, surface roughness

1. Introduction

Solid suspensions consisting of solid particles dispersed in a continuous liquid phase have been widely used for drug delivery purposes for various reasons. One of these is that the insolubility of pharmaceutical active ingredients, which has emerged as one of the most challenging issues in the development of new formulations and which can affect the formulation stability and also lead to poor drug bioavailability, can now be circumvented by using solid dispersions (1, 2). The solid suspension system has also been proven to be a good platform for drug loading and controlled drug release (3, 4). Particles suspended in pressurized liquids are ideal for regionally targeted drug delivery in the human respiratory system because they can come into direct contact with the airway upon aerosolization and inhalation (5, 6). Pressurized metered dose inhalers (pMDIs) containing pharmaceutical suspensions are the most widely prescribed form of medication for the treatment of airway diseases such as asthma and chronic obstructive pulmonary disease (7). A pMDI device consists of a metering valve that connects a fixed-volume metering chamber, which is typically filled with drug suspension, to the environment, releasing a burst of fast-evaporating suspension droplets when actuated. For dosing uniformity considerations, the metering valve must release doses of suspensions that are not only consistent in mass but also have a concentration representative of the bulk formulation (8, 9). Pressurized pharmaceutical suspension is the subject of the

50 present study and will be discussed in depth, but many of the concepts presented here can be universally applied to other suspension systems.

Stable suspensions are almost always desired for pharmaceutical applications. However, the suspended particles may destabilize over time mainly through two different mechanisms: particle migration and particle agglomeration. Particle migration by upward creaming or downward
55 sedimentation is caused by buoyancy due to the density difference between the particles and the liquid in which they are suspended. The settling velocity of an individual particle, v_s, with a volume equivalent diameter of d_{ve} or an aerodynamic diameter of d_a can be described by the Stokes' law as (10):

$$v_s = \frac{(\rho_P - \rho_F)g}{18\mu\chi} d_{ve}^2 = \frac{(\rho_T - \rho_F)(1-\phi)g}{18\mu\chi} d_{ve}^2 = (1-\frac{\rho_F}{\rho_T}) \frac{\rho_0 g}{18\mu\chi} d_a^2 \quad (1)$$

where ρ_P is the effective particle density, ρ_F and ρ_T are the density of the fluid and the true density of the suspended particle, ρ_0 is the standard reference particle density at 1000 kg/m^3, ϕ is the porosity
60 of the particle, g is the gravitational acceleration, μ is the dynamic viscosity of the medium, and χ is the dynamic shape factor to account for non-spherical particles. Therefore, particles with a higher true density than the liquid will settle to the bottom of the suspension while particles with a lower true density than the liquid will exhibit upward velocity and eventually accumulate at the top, forming a cream layer. Smaller liquid-particle density difference, structured particles with high porosity, and smaller particles can
65 all help reduce the particle settling velocities and stabilize the suspensions. In real applications, situations involving only individual particles are rarely seen and, for this reason, the effects of agglomeration need to be included in this discussion.

Particle agglomeration, which is also known as flocculation or aggregation, is a combined effect of both attractive and repulsive forces present in the suspension system. The forces between particles in
70 colloidal systems are usually described by the classic Derjaguin-Landau-Verwey-Overbeck (DLVO) theory (11), in which attractive van der Waals forces and repulsive double-layer forces are considered. The van

der Waals forces between macroscopic particles are caused by the collective inter-molecular forces from the interacting particles, and they are one of the driving forces for particles to collide and remain as aggregates upon collision. For two perfectly spherical particles of radii R_1 and R_2, the macroscopic Van der Waals force, F_{VDW}, can be described by (11):

$$F_{\mathrm{VDW}} = -\frac{A_{\mathrm{H}}}{6D^2}\left(\frac{R_1 R_2}{R_1 + R_2}\right) \quad (R_1, R_2 \gg D) \tag{2}$$

in which A_{H} is the Hamaker constant that depends on the materials of the two interacting particles. D is the minimum separation distance of the two particles at which the attractive and repulsive molecular forces are balanced, and its values are substance-dependent with a typical value of 0.4 nm. Therefore, larger particles will show stronger attraction forces. In a suspension system, the larger particles also demonstrate higher collision frequencies because of their larger cross-section area and higher settling velocities. The collision frequency can be further enhanced by the stronger attractive van der Waals forces between larger particles, leading to the growth of the large particles or agglomerates through the attraction of the other particles and consequently faster settling velocities.

Surfaces of the suspended particles can also become charged through various mechanisms, such as ionization or dissociation of surface groups, adsorption or binding ions from solution, and then the net surface charges are balanced by a layer of counterions, forming a diffuse electric double-layer (11). Particles with similarly charged surfaces repel each other electrostatically when approaching each other, causing the suspensions to stabilize. However, the repulsive electrostatic forces originating from the electric double-layers are usually considered insignificant in preventing particles from aggregating in non-aqueous suspension systems where the liquid phases have low conductivities and dielectric constants, as is the case for pharmaceutical suspensions contained in pressurized metered dose inhalers (12, 13). Therefore, suspension-based pMDIs with non-aqueous propellants are mainly governed by the attractive van der Waals forces and are inherently unstable. It is also because of the nonpolar nature of the

propellants that particle-particle interaction forces usually obtained in air are expected to be useful for pressurized suspension systems as well.

Unstable suspensions in pharmaceutical applications can cause serious issues. For example, in respiratory drug delivery, collective particle migration by creaming or sedimentation can lead to large variations between delivered drug doses from the metering valve, while particle aggregation can cause the size distribution of suspended drug particles to deviate from the optimum respirable range towards the larger end and eventually affect both the amount and the site of drug deposition in the airways (14, 15). It has also been demonstrated in the literature that the dose uniformity of pMDIs can be directly related to the stability of applied drug suspensions (9). This stability issue is the exact reason why patients prescribed pMDI medications are instructed to shake the canisters 'vigorously' before actuation and why failure to do so accounts for most of the incorrect use of inhalation devices (16).

Various approaches have been developed to improve the colloidal stability of pharmaceutical suspensions for better performance. According to Eqn.(1), hollow-porous particles by increasing the particle porosity ϕ (17, 18) and nanosuspensions by reducing the size of suspended particles d_{V} (19, 20) have been two of the most commonly used strategies to minimize the settling velocities of suspended particles and achieve stable suspensions. Particles with hollow-porous structures allow the propellant to permeate freely into the particles, minimizing the particle-liquid density difference and eventually reducing their settling velocities. Nanosuspensions are colloidal dispersions of nanoparticles that either have low settling velocities or may never completely settle because of the counteracting effect of Brownian motion (21). Propellant blends with densities close to the true densities of suspended particles have also been demonstrated to be able to stabilize suspensions (22, 23).

Polymeric surfactants are also commonly used to introduce steric repulsion forces between particles to stabilize suspensions (24). The surfactants are usually amphiphilic non-ionic polymer molecules with long tails that can absorb onto the surface of the drug particles and form a molecular layer of barrier that

prevents the particles from approaching each other and thereby, leads to stabilized suspensions. Commonly used surfactants in pMDI suspensions include lecithin, oleic acid, and sorbitan trioleate because of their relatively good solubility in the propellant. Unfortunately, the mandated switch from chlorofluorocarbon propellants to the "ozone-friendly" hydrofluoroalkane (HFA) propellants over the past 20 years has resulted in unexpected formulation challenges because of the incompatibility between the HFA propellants and traditional surfactants (25). Such incompatibility is expected to become more of an issue as newer propellants with lower global warming potential are actively developed in the pharmaceutical industry (15).

Despite the various approaches that have been developed to improve the colloidal stability of suspensions, the impact of particle morphology, including surface roughness, on suspension stability has received relatively little study. For dry powder inhalers, it has been demonstrated that the increased microparticle surface roughness was able to significantly reduce the particle adhesion and eventually improve their in vitro aerosolization performance (26). The adhesive and cohesive forces between particles have been measured using atomic force microscopy and correlated to the stability of corresponding suspensions (27-29). A study carried out by D'Sa et al. (30) demonstrated that spray-dried particles designed to contain greater numbers of internal void structures resulted in larger specific surface area, weaker inter-particle forces, and eventually suspensions with better physical stability in a model propellant. Recently, it has also been shown that rugosity is a major factor determining the cohesiveness of particles (31). The cohesion forces between microparticles of differing roughness were measured and compared with various theoretical models, proving that surface roughness is the dominant factor affecting the cohesion forces between microparticles. This is because for real particle interactions, the protrusions and indentations on the particle surfaces that are larger than intermolecular spacings but smaller than the particle sizes can cause the actual interaction force to deviate significantly from the

theoretical prediction described in Eqn.(2), which assumes particles with perfectly smooth surfaces. A modified version is described in Eqn.(3),

$$F_{\mathrm{VDW}} = -\frac{A_{\mathrm{H}}}{6D^2}\sum_{k=1}^{N}\left(\frac{r_1 r_2}{r_1 + r_2}\right) \quad (r_1, r_2 \gg D) \tag{3}$$

where r_1 and r_2 stand for the radii of the $k\mathrm{th}$ of the N total interacting asperities from two separate particles, shows that the van der Waals forces between two imperfect particles can be significantly reduced by the particle surface roughness as $\left(\frac{R_1 R_2}{R_1 + R_2}\right) \gg \sum_{k=1}^{N}\left(\frac{r_1 r_2}{r_1 + r_2}\right)$ for particles without elastic deformation, which is the case for particles in suspensions and are in loose contact (14). Therefore, particles with high surface roughness will become orders of magnitude less cohesive. Since surface roughness can significantly reduce the attractive forces between two interacting particles, we hereby investigate the suitability of stabilizing pharmaceutical suspensions by intentionally introducing different levels of surface roughness to the suspended particles.

Studying the stability of suspensions with conventionally manufactured, polydisperse particles is complicated because the various size-dependent particles properties—e.g., settling velocity (10), optical properties (32), and level of deaggregation upon agitation (33)—can make it relatively difficult to analyze the effects of each individual factor on the suspension stability. To avoid the potential complication introduced by polydisperse particles, for the first time, with the help of a monodisperse spray drying technique, we modify the surface properties of the particles, in particular the rugosity, to study the effects of surface roughness on the colloidal stability of pressurized pharmaceutical suspensions. Findings of this work can be used as an effective approach to improve the colloidal stability of, but not limited to, pressurized pharmaceutical suspensions.

2. Materials and methods

2.1. Materials

Trehalose is a disaccharide that can be spray dried into spherical, solid particles (34). D-(+)-trehalose dihydrate (177613, Fisher Scientific Co., Ottawa, ON, Canada) was first dissolved in demineralized water to prepare feed solutions for subsequent spray drying of monodisperse particles. Trileucine is a surface-active amino acid that has been used to modify the morphology of spray-dried particles to produce low-density and non-cohesive particles for dry powder inhalers (35). The crystalline trileucine used for feed solution preparation in this study was obtained directly from the supplier (BCBP2254V, Sigma-Aldrich Corp., St. Louis, MO, USA).

2.2. Methods

2.2.1. Monodisperse spray drying

The experimental setup for monodisperse spray drying includes a custom-designed micro-jet atomizer (36) integrated with a custom laboratory scale spray dryer (37). As shown in the schematic in **Fig.1**, the micro-jet atomizer was used to generate monodisperse droplets of feed solutions. Briefly, a pressurized liquid solution was supplied to the nozzle head from the feed line and fed through a micro-orifice to form a liquid micro-jet. Since the random breakup of liquid jets due to the surface tension usually leads to polydisperse droplets, a piezoelectric ceramic ring (105261, Meggitt A/S, Denmark) was attached to the nozzle head to force regular disintegration of the liquid jet into monodisperse droplets (38). The piezoelectric transducer was driven by a function generator (DS340, Stanford Research Systems, CA, USA) supplying square waves with peak-to-peak voltage of 20 V and frequencies ranging from 120 kHz to 160 kHz. The dispersing gas supplied through the orifice cap was used to disperse the droplet chain to avoid droplet collisions. A more detailed description of the atomizer can be found elsewhere (36). The generated monodisperse droplets were then dried in a lab-scale spray dryer and the resulting particles collected

using a stainless-steel cyclone. Detailed spray drying parameters are listed in **Table 1**. The selected 30 µm micro-jet orifice in this study can be used to produce droplets in the range of 50 µm – 65 µm (36), depending on the liquid properties, piezoelectric ceramic driving frequency, pressure difference across the orifice, etc. The drying gas flow rate and drying temperature were set to ensure that the droplets were completely dried, and the cut-off size of the cyclone was smaller than the dried particles. A time-of-flight aerodynamic particle sizer (3321, TSI, Shoreview, MN, USA) was used in-line to check the monodispersity of dried particles during the spray drying process and to measure the aerodynamic size distributions of the produced particles (37). All collected particles were dried in a vacuum desiccator to remove any residual moisture before preparation of pressurized suspensions for subsequent stability analysis.

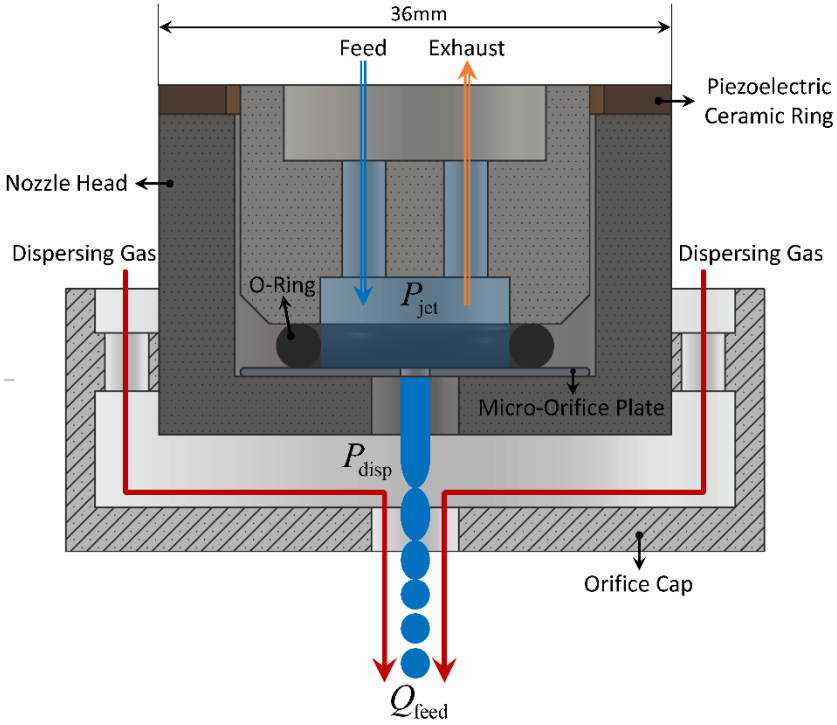

Fig.1.

Table 1. Parameters used for monodisperse spray drying

Spray-drying parameter	Value
Micro-jet pressure	500±50 kPa
Feed solution flow rate	0.8±0.1 mL/min
Micro-orifice diameter	30 µm

Inlet temperature	70 °C
Outlet temperature	52±0.5 °C
Disperser orifice diameter	3.0 mm
Dispersing gas pressure	240 kPa
Drying gas flow rate	600 L/min
Piezoelectric driving frequency	120 - 160 kHz

2.2.2. Particle design

Monodisperse solid model particles with similar surface morphology but of different sizes were first needed to study the effects of particle size on the suspension stability. Particles with different surface rugosity and of similar size were then designed to further study the effects of surface roughness on the colloidal stability of pressurized suspensions. The theory of particle formation during spray drying (34, 39) was used to determine the compositions and process conditions required to achieve these targets.

During the drying process of solution droplets, a dimensionless Peclet number such that:

$$Pe_{\mathrm{i}} = \frac{\kappa}{8D_{\mathrm{i}}} \tag{4}$$

which is a ratio of the solvent evaporation rate, κ, to the diffusion rate of solute, D_{i}, and is usually used as an indicator to predict the final particle morphology. The Peclet number can be directly used to derive the surface enrichment for each component E_{i}:

$$E_{\mathrm{i}} = \frac{c_{\mathrm{s,i}}}{c_{\mathrm{m,i}}} \approx 1 + \frac{Pe_{\mathrm{i}}}{5} + \frac{Pe_{\mathrm{i}}^2}{100} - \frac{Pe_{\mathrm{i}}^3}{4000} \quad (0 \le Pe_{\mathrm{i}} \le 20) \tag{5}$$

which is defined as the ratio of the surface concentration, c_{s}, to the mean droplet concentration, c_{m}, with good accuracy for relatively low Peclet numbers (< 20). More substantial discussion of the relation between the Peclet number and surface enrichment can be found elsewhere (40). Depending on the nature of the solute, once a critical concentration, $c_{\mathrm{c,i}}$, e.g., saturation concentration or solubility ($c_{\mathrm{sol,i}}$) for crystallizing systems, component true density ($\rho_{\mathrm{t,i}}$) for non-crystallizing systems, at the droplet surface is reached, the droplet solidification process will be triggered. The time it takes for each

component to reach the critical concentration at the droplet surface, $\tau_{c_{c,i}}$, depends on the droplet drying time, τ_D, and the ratio of these time scales can be defined in terms of the surface enrichment, E, and initial concentration, c_0 as:

$$\frac{\tau_{c_{c,i}}}{\tau_D} = \left[1 - \left(\frac{c_{0,i} \bullet E_i}{c_{c,i}}\right)^{\frac{2}{3}}\right] \quad (6)$$

in which the droplet drying time, τ_D, depends on the initial droplet diameter, d_0, and evaporation rate of the liquid phase, κ, as $\tau_D = d_0^2 / \kappa$.

Surface composition and morphology of particles produced in the spray drying process can therefore be predicted according to Eqn.(4), (5), and (6). A high Peclet number solute usually leads to high surface enrichment, early surface saturation, and subsequently hollow particles. Depending on the properties of the shell, the hollow particles may buckle or collapse to form wrinkled particles. The outcome for low-Peclet number systems differs: a component with a low Peclet number and high solubility will produce small surface enrichment throughout the whole droplet lifetime and eventually form homogeneous solid particles, as is the case for trehalose used in the current study. The characteristic time for the droplet to solidify is close to the droplet lifetime, making the dried particle density close to the true density of the solutes. However, for solution droplets with low Peclet number components but also low solubility, e.g., trileucine, the time to saturation, $\tau_{c_{sol},i}$, or true density, $\tau_{\rho_t,i}$, is short compared to the droplet lifetime, τ_D. Hence, the droplet surface becomes supersaturated early, leading to the nucleation of a solid phase and early formation of a surface shell. The shell may also later collapse in the drying process through lack of mechanical strength, forming wrinkled particles.

The two components used in this study, trehalose and trileucine, both have relatively low Peclet numbers ($Pe \approx 1$) under the spray drying conditions listed in **Table 1**. The difference is that trehalose is highly soluble in water with a solubility at 690 mg/mL, while trileucine has a very low solubility at 7 mg/mL. Three

feed solutions of pure trehalose with different concentrations at 1 mg/mL, 5 mg/mL and 30 mg/mL, as listed in **Table 2**, were prepared and spray dried. The characteristic times for trehalose to reach its true density on the droplet surface are indeed close to the droplet lifetime with $\tau_{\rho_{t,Tre}}/\tau_D$ >90% for all the cases. According to the particle formation theory introduced earlier, solid spherical trehalose particles are expected and to be used as model particles.

Feed solutions with a fixed total solids concentration of 5 mg/mL but different trehalose-trileucine ratios of 99.6:0.4, 99.0:1.0, and 95.0:5.0 were also spray dried to introduce difference levels of surface roughness to the dried particles. The case with 0.4% trileucine and 99.6% trehalose corresponds to a special case in which the surface concentration of trehalose reaches its true density almost at the same time as trileucine reaches saturation on the droplet surface, meaning that the particle solidifies at the same time as the trileucine surface concentration reaches supersaturation. As presented in **Table 2**, trileucine reaches its saturation concentration at the end of the droplet drying process at 97.7% of the droplet lifetime, which is right after trehalose reaches its true density at the droplet surface at 97.5% of the droplet life time. Neglecting the effects of trileucine surface activity, trileucine is expected to form a thin film of layer on the surface at the exact time point when trehalose starts to solidify at the surface. Relatively smooth particles with a layered structure are expected for this case. According to the calculation, the other cases with more trileucine are expected to force earlier shell formation and produce particles with more surface rugosity.

Table 2. Feed solutions for monodisperse spray drying with calculated time for trileucine to reach surface saturation normalized by droplet lifetime, time for trehalose to reach true density normalized by droplet lifetime, and calculated true density of the mixture

Feed solution	Trehalose (mg/mL)	Trileucine (mg/mL)	$\tau_{c_{Sol,Tri}}/\tau_D$ (%)	$\tau_{\rho_{t,Tre}}/\tau_D$ (%)	$\rho_{t,mix}$ (g/cm^3)
1	1	-	-	99.1	1.53
2	5	-	-	97.5	1.53
3	30	-	-	91.7	1.53
4	4.98	0.02	97.7	97.5	1.53
5	4.95	0.05	95.7	97.5	1.52

6	4.75	0.25	87.4	97.6	1.50

2.2.3. Morphological and spectroscopic analysis

All monodisperse spray-dried particles before and after suspension in the propellant were analyzed using a scanning electron microscope (EVO M10, Zeiss, Germany) to confirm particle morphology and a custom-designed Raman spectrograph (41) was used to verify the solid state of the dried particles. For electron microscopy, all spray-dried particles were sampled on standard SEM pin mounts (Ted Pella Inc., USA) covered with double-sided adhesive carbon tape as substrates and further sputter-coated with gold nanoparticles (Desk II Sputter Coater, Denton Vacuum, NJ, USA). Collected particles were loaded into the 0.2 µL-cavity of an aluminum sample holder for Raman spectroscopic analysis. The Raman system utilized a 671 nm diode-pumped laser (Ventus 671, Laser Quantum, UK) with a maximum power of 500 mW. All measurements were conducted under a nitrogen atmosphere at room temperature (21 ± 1 °C) and in dry conditions (< 3% RH). Raw materials received from the manufacturers were measured directly as the reference materials for crystalline leucine and trileucine, and spray dried trileucine and trehalose were used as their corresponding amorphous reference materials.

2.2.4. Particle size measurement

A time-of-flight aerodynamic particle sizer (APS) was used in-line during the spray drying processes to measure the size distributions of the dried particles. The particle sizer was set to operate at a standard flow rate of 5 L/min, taking a 20 s-measurement every 5 minutes. Volume equivalent diameter distributions of the spray-dried pure trehalose particles were also measured by SEM image analysis assuming perfectly spherical particles and fitting the particle edges using circles (ImageJ 1.52d, NIH, MD, USA). More than 300 particles for each of the spray-dried trehalose batches were counted and measured to generate their corresponding count based cumulative particle diameter distributions, a method possible only when the geometric standard deviation (*GSD*) of the particle size distribution is small.

Aerodynamic particle size distribution and volume equivalent diameter distributions were compared to confirm monodispersity and correct size measurement for dried particles.

2.2.5. Specific surface area measurement

To quantitatively compare the difference of surface roughness between the spray-dried powders, their specific surface areas were measured using a 7-point BET (Brunauer–Emmett–Teller) (42) method (Model ASIQCU000-5, autosorb iQ, Quantachrome Instruments, FL, USA). For each test, 0.2-0.4 g of monodisperse spray-dried powder was first loaded into a sample cell (O.D. = 6 mm) and degassed at 50 °C for 30-120 minutes. Since relatively small specific surface areas were expected for the tested powder samples due to the lack of internal void space, krypton (M.W. = 83.80 g/mol) was used as the adsorbate gaseous phase and was assumed to have a single-molecule cross-sectional area of 20.5 $Å^2$. The krypton physisorption analysis was then conducted for a relative pressure (P / P_0) range of 0.05-0.35 at the boiling temperature of liquid nitrogen at -196 °C.

In addition to the specific surface area, the adsorbent-dependent BET constant was also determined. The BET constant is known to be directly related to the adsorption energy for the first adsorbed layer and its value is an indication of the magnitude of the adsorbent/adsorbate interactions (42). Therefore, the BET constant in this study was used as a secondary evidence to support that the surface compositions of the formed particles were as predicted by the theory of particle formation during spray drying.

2.2.6. Pressurized suspensions

Pressurized suspensions of the monodisperse spray-dried particles were prepared by weighing 50 mg ± 2 mg of the dried powders into a glass vial, crimping an aluminum metering valve (DF30, Valois Pharma, NY, USA) onto the glass vial, and then using a benchtop pMDI production station (2005/21, Pamasol Willi Mäder AG, Switzerland) to pressure-fill 22.0 g ± 0.5 g of HFA-227ea propellant (UN3296, Mexichem Fluor Inc., UK) through the valve into the vial. The glass vials used for stability measurement are custom-designed round, flat-bottomed borosilicate glass vessels (Adams & Chittenden Scientific Glass, CA, USA)

measuring 75.5 mm in height and 27.5 mm in outer diameter, and featuring a 900 kPa pressure rating, with good transmissivity.

2.2.7. Suspension stability measurement

Suspension stabilities of the particles in propellant HFA-227ea were measured using a shadowgraphic imaging method developed by Wang et al. (43). Briefly, the technique acquires high-resolution sequential images of suspensions contained in transparent glass vials in a bright field and performs post image processing to extract the time (t) dependent change of transmission intensity (T) at different heights (h) along the suspension. The normalized relative transmission profiles, $\Delta T_{t,h}^{\mathrm{N}}$, are then calculated as

$$\Delta T_{t,h}^{\mathrm{N}} = \frac{\Delta T_{t,h}}{\Delta T_{t,h}^{\mathrm{Max}}} = \frac{T_{t,h}^{\mathrm{a}} - T_{t_0,h}^{\mathrm{a}}}{T_{\mathrm{Clear}}^{\mathrm{a}} - T_{t_0,h}^{\mathrm{a}}} \tag{7}$$

in which $\Delta T_{t,h}$ is the relative transmission profiles for the change of absolute transmission, $T_{t,h}^{\mathrm{a}}$, relative to the initial transmission profile, $T_{t_0,h}^{\mathrm{a}}$. $\Delta T_{t,h}$ is then normalized by its maximum value, $\Delta T_{t,h}^{\mathrm{Max}}$, which is the difference between the transmission for clear propellant, $T_{\mathrm{Clear}}^{\mathrm{a}}$, and the initial transmission of the sample being tested, $T_{t_0,h}^{\mathrm{a}}$. The normalized relative transmission profiles, $\Delta T_{t,h}^{\mathrm{N}}$, provide semi-quantitative information about the whole destabilization processes with abundant local details. In addition, by integrating each of the normalized relative tranmission profiles, $\Delta T_{t,h}^{\mathrm{N}}$, according to:

$$\sigma(t) = \int_{h=0}^{h=1} \left| \Delta T_{t,h}^{\mathrm{N}} \right| \tag{8}$$

a single parameter, termed the instability index, $\sigma(t)$, is derived to account for the overall transmission changes during the suspension destabilization processes and can therefore be used to quantitatively compare and rank-order the stabilities of different samples. The instability index, $\sigma(t)$, is a dimensionless number ranging from 0 for extremely stable samples to 1.0 for suspensions that destabilize completely to clear liquid at a time t, and its derivative $d\sigma(t)/dt$ indicates the rate of destabilization.

In this study, stabilities of all the suspensions were measured within the same day of propellant filling to avoid the effects of moisture ingress on the suspended particles. Immediately before each stability measurement, the suspensions were agitated for 30 s in an external small-scale ultrasonic bath (M1800H, Fisher Scientific Comp., Ottawa, ON, Canada) to redisperse the suspended particles and break up any aggregated particles. The suspension tester was set to acquire shadowgraphic images at a frame rate of 0.5 Hz and an exposure time of 0.50 ms. The backlight LED was operated at a driving current of 1.0 A with a pulse width of 1.0 ms. The stabilities of all suspensions were measured for 30 min immediately after the ultrasonic agitation. The settings and operating procedures were kept consistent for all the suspension stability measurements. Three suspension samples were prepared for each batch of spray-dried particles and each suspension was measured three times.

3. Results and discussion

3.1. Morphological and spectroscopic analysis

SEM images of particles produced under different conditions are shown in **Fig.2**. This figure highlights that uniform and spherical trehalose particles were produced using the monodisperse spray drying technique. Because of the low Peclet number of trehalose and its high solubility in water, these particles were expected to be solid inside with little or no internal void space, and with a density close to the true density of trehalose (44). With the micro-jet orifice kept the same for all the spray-dried batches, and the feed solution concentration increased from 1 mg/mL to 30 mg/mL, the diameters of the resultant particles also increased as designed.

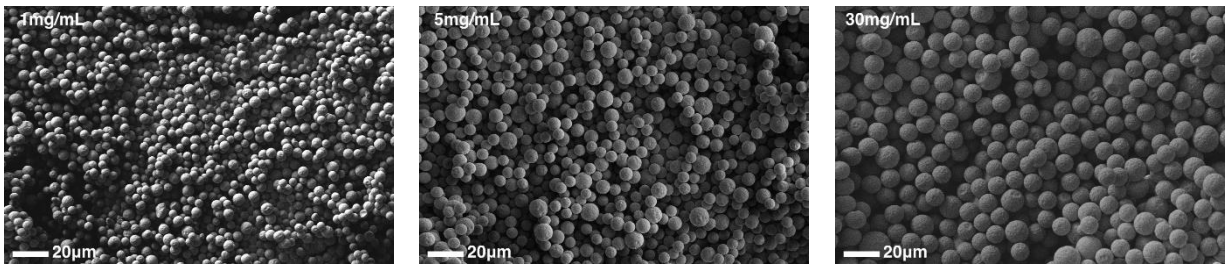

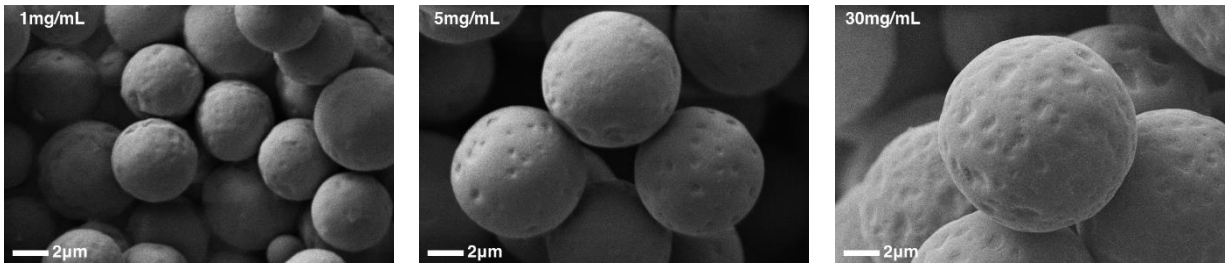

Fig.2.

Because of the low Peclet number and low solubility of trileucine, the addition of trileucine changed the morphologies of the spray-dried particles significantly as expected, as shown in **Fig.3**. These results prove that trileucine caused early surface enrichment and shell formation during the drying process of the monodisperse solution droplets. Starting from the spherical particles formed from the pure trehalose solution at the top of the figure, the particles become more wrinkled the more trileucine is added, a result similar to those observed in the literature (35). However, the special case of feed solution with 0.4% trileucine and 99.6% trehalose produced particles that were generally smooth with only a slightly increased rugosity, a result different from what has been reported and proving that the strategy to have trileucine and trehalose precipitate at roughly the same time to form a layered surface structure was successful. For the cases with 1.0% and 5.0% trileucine, trileucine shells were formed much earlier in the particle formation processes and collapsed later due to lack of mechanical strength, causing the particles to be more rugose, as planned. Theory according to Boraey and Vehring (40) allows a rough estimate of shell thickness assuming that all the trileucine is on the surface. The thickness was estimated to be on the order of 10 nm, which Raman results later confirmed to be amorphous. Therefore, it is plausible that this thin shell had enough residual mobility to fold when formed initially and collapsed in the subsequent drying processes. No significant morphology changes were found for the particles extracted from the propellant, SEM images shown in **Fig.A2**, proving that no dissolution or disruption of the particles occurred during the timeframe of the stability measurement.

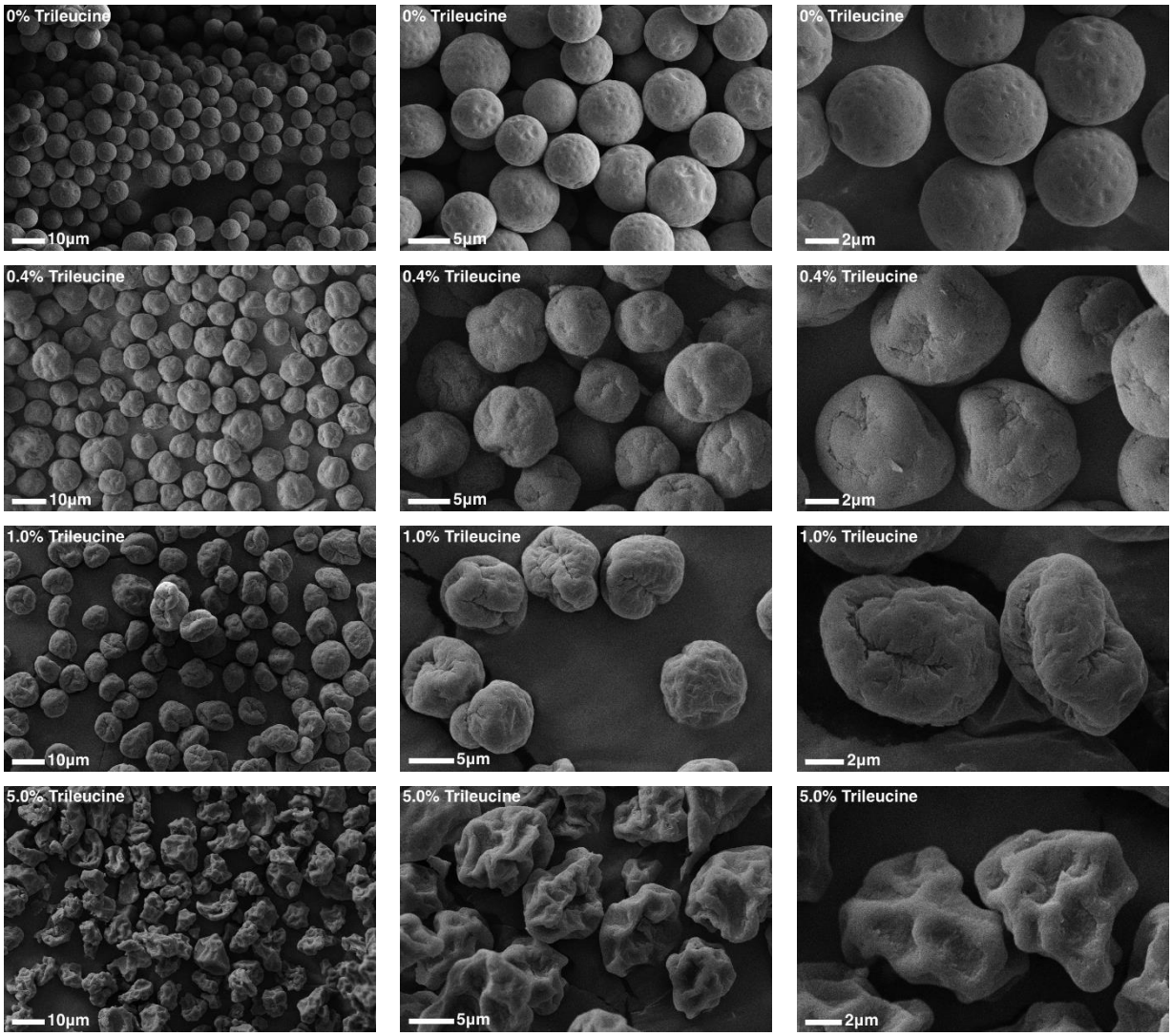

Fig.3.

The results of solid phase analysis by Raman spectroscopy are shown in **Fig.4**. Reference Raman spectra of amorphous (a-Tre) and crystalline (c-Tre) trehalose show different features in the displayed spectral region (70 – 1600 cm^{-1}, 2800 – 3200 cm^{-1}). For the first time, to our knowledge, the Raman spectra of amorphous (a-Leu_3) and crystalline (c-Leu_3) trileucine are also presented and compared. In general, crystalline materials have sharper and better-defined peaks because of the more isolated vibrational energy levels of their molecular bonds, while the Raman peaks are broadened due to the higher degree of disorder in amorphous materials (45, 46). In comparison with the reference spectra of both amorphous

and crystalline trehalose, a 100% amorphous state was confirmed for the three batches of spray-dried pure trehalose presented in **Fig.2**. Because of the low concentration of trileucine in the spray-dried trehalose-trileucine particles, a subtraction process was used for the solid-state identification. As a demonstration, the bottom trace in **Fig.4** is a residual spectrum after subtracting amorphous trehalose from the spectrum of the spray-dried sample with 95% trehalose and 5% trileucine. The residual spectrum is similar in shape to the reference spectrum of amorphous trileucine, and no trace of crystalline trehalose or trileucine can be found, proving the completely amorphous state of trehalose and trileucine in the dried particles. The solid state of trehalose and trileucine in the other cases was similarly determined to be 100% amorphous.

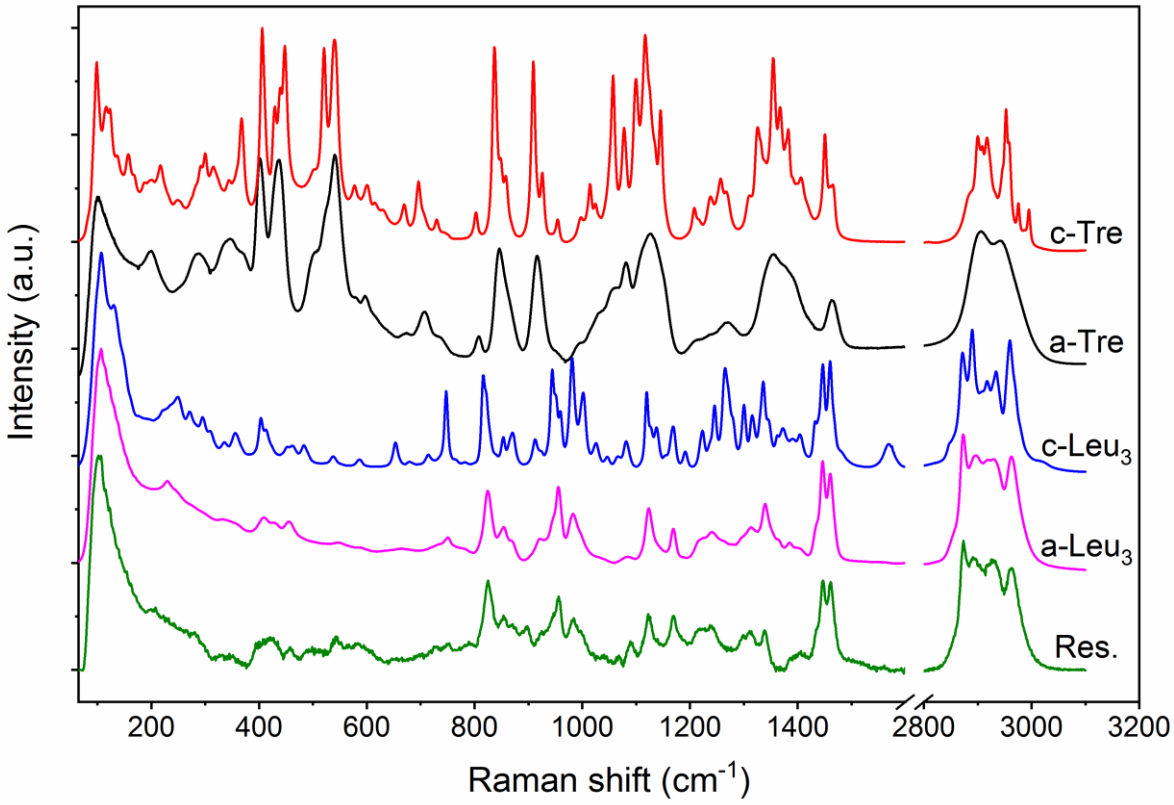

Fig.4.

3.2. Size distributions of spray-dried particles

Three typical mass-based aerodynamic particle size distributions measured by the in-line particle sizer for the feed solutions with different initial concentrations are presented in **Fig.5**. These were in good agreement with the monomorphic particles observed from the SEM morphological analysis, all having narrow geometric standard deviations (*GSD* < 1.2), meaning that the dried trehalose particles were uniform and monodisperse. It is known that aerodynamic diameter, d_a, of spray-dried particles is related to the feed solution concentration, c_0, such that

$$d_a = \sqrt[6]{\frac{\rho_P}{\rho_0}} \bullet \sqrt[3]{\frac{c_0}{\rho_0}} \bullet d_0 \tag{9}$$

in which ρ_P, ρ_0, and d_0 are the particle density, unit density, and initial droplet diameter respectively. As designed, the three different batches of spray-dried trehalose showed very distinct mass median aerodynamic diameters (*MMAD*), and the final particle size increased with the trehalose solution concentration.

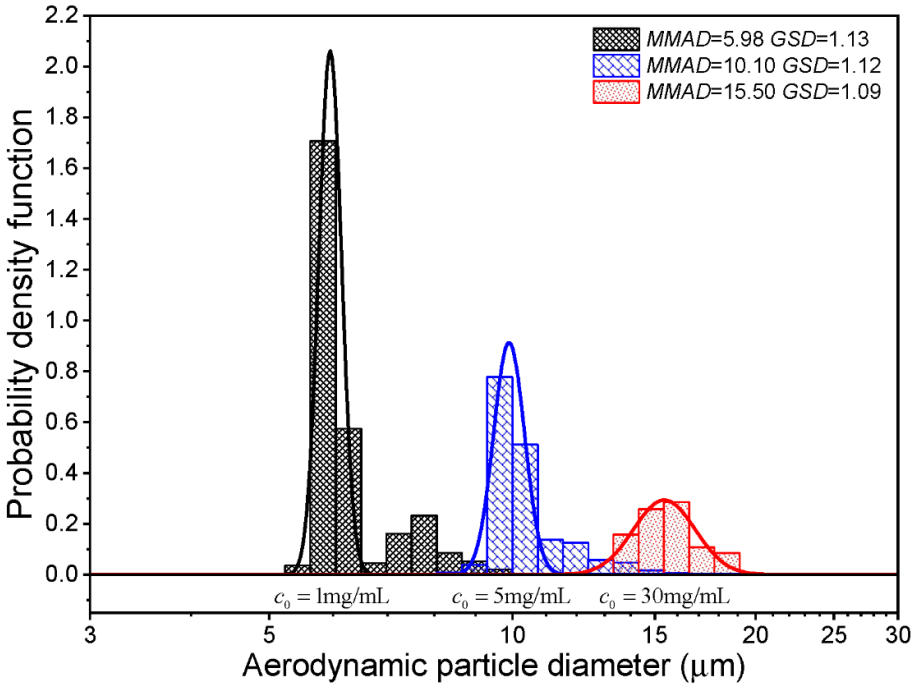

Fig.5.

Fig.6 shows the cumulative distributions of the measured trehalose volume equivalent diameters and fittings of the data with a least square regression method. All three cases also had good monodispersity with *GSD* < 1.2, which is in a good agreement with the results of direct aerodynamic size measurement. According to the central limit theorem, the obtained volume equivalent diameters after measuring more than 300 particles for each sample were within small intervals (±0.11, ±0.15, ±0.16) around the population median diameters with a high confidence level (99%), making this method of assessing the particle size distributions feasible. The count-based median volume equivalent diameters were compared to the APS-measured *MMAD* by first converting the volume equivalent diameter, d_{ve}, to aerodynamic diameter, d_{a}, according to Eqn.(1) assuming that the particle density was the same as the trehalose true density. The calculated aerodynamic diameter was thus equivalent to the count median aerodynamic diameter, *CMAD*. The *CMAD* was then used to calculate the *MMAD* using the Hatch-Choate Eqn.(10) (47), which is practical only for monodisperse or near monodisperse particles. Otherwise, a large bias error will be inevitable with this method for particles with a large *GSD* unless a very large number of particles are measured. Uncertainties of the calculated *CMAD* and *MMAD* were estimated by assuming that the particle density is within ±5% of its true density and the measured geometric standard deviation has a 10% uncertainty.

$$MMAD = CMAD \cdot \exp(3\ln^2 \sigma_g) \tag{10}$$

The comparison in **Table 3** shows that the calculated *MMAD* based on the volume equivalent diameter was close to the *MMAD* measured directly by the APS, indicating that the spray-dried particles were indeed monodisperse and their particle size distributions were correctly measured separately. These findings also mean that there was little or no void space, as expected. Using the particle size measured for the dried particles and a simple relation of solute mass conservation, the initial droplet diameters were also calculated to be within the predicted droplet size range of 50 μm – 65 μm. The asymmetrical and

bimodal shape of the distributions indicating the existence of exceptional sized particles is observed in both **Fig.5** and **Fig.6**, and is a known phenomenon likely caused by doublets, triplets, etc., due to droplet coalescence in the spray. However, these larger particles caused by the droplet coalescence are negligible in their count-based size distributions and are expected to settle much faster than the particles with primary sizes, hence their effects on the suspension stability measurements are expected to be minor.

Table 3. Comparison of particle size distributions measured using different methods

d_{ve} (µm)	σ_g	d_{ve} confidence interval (99%)	d_a (*CMAD*) ± δ (µm)	*MMAD*-Calc. ± δ (µm)	*MMAD*-APS (µm)	d_0 (µm)
5.10	1.14	0.11	6.31 ± 0.21	6.65 ± 0.57	5.98	58.8
8.12	1.16	0.15	10.04 ± 0.33	10.74 ± 1.01	10.10	54.7
13.52	1.13	0.16	16.72 ± 0.48	17.49 ± 1.37	15.50	50.2

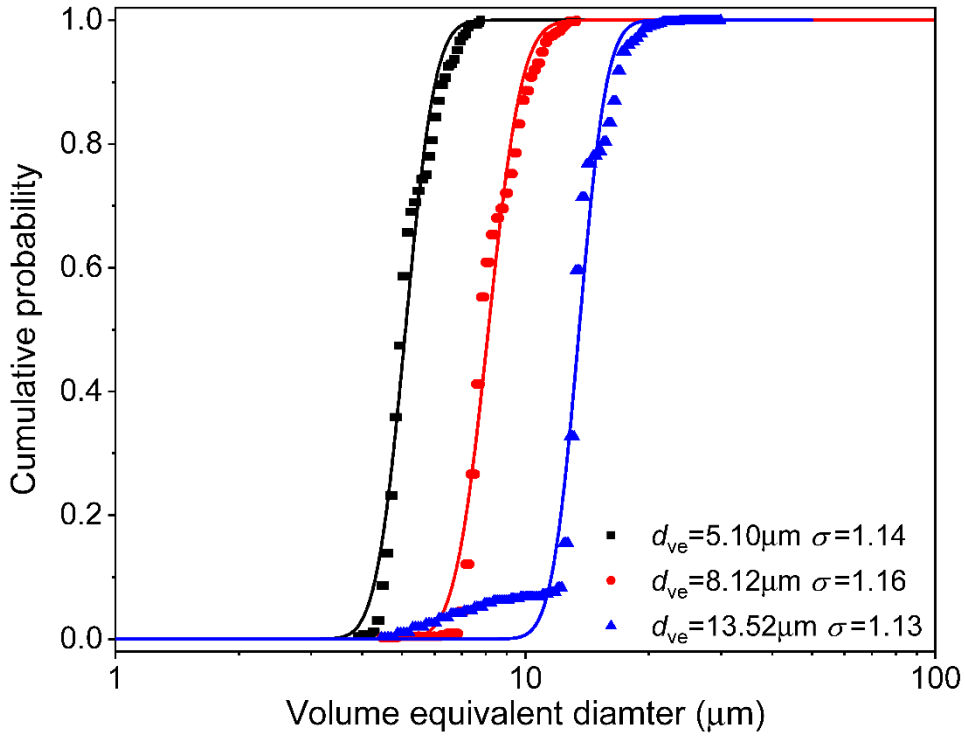

Fig.6.

Aerodynamic particle size distributions for the spray-dried formulations with different trehalose-trileucine ratios are presented in **Fig.7**. All batches show good monodispersity with narrow geometric standard

deviations (*GSD* < 1.2). The four batches of particles with the same solids concentration show similar mass median aerodynamic diameters. A slight shift of the *MMAD* towards the lower end from 10.1 μm to 8.7 μm is also observed. This is because particles with a higher level of rugosity lead to lower particle density, and therefore smaller aerodynamic diameters, according to Eqn.(9). Overall, particles with different surface rugosity and similar size were successfully produced as designed.

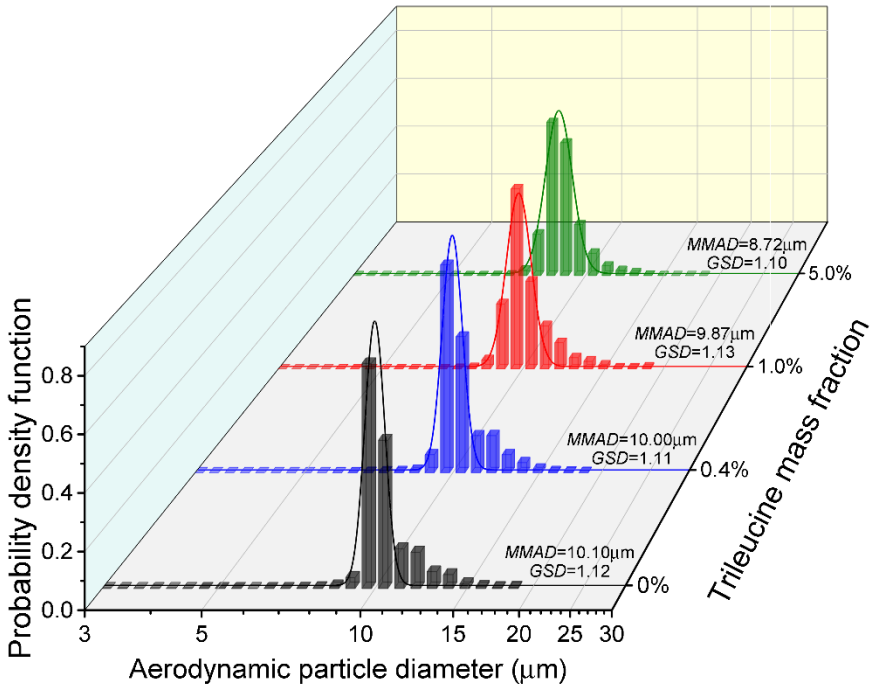

Fig.7.

3.3. Specific surface area analysis

In addition to the qualitative particle roughness information provided by the SEM images, specific surface areas of the monodisperse spray-dried powders were measured to provide quantitative confirmation. Shown in **Fig.8** is a comparison of the surface rugosities for the spray-dried formulations with different trileucine concentrations. The real specific surface area (A_r) was directly measured from the BET method, and the geometric specific surface area (A_g) for each sample was calculated based on the particle size presented in **Fig.7** and assuming perfectly spherical and smooth particles for all the four cases. The surface

rugosity for the pure trehalose sample is slightly higher than 1.0, which is expected and is likely to be caused by the particles not being perfectly monodisperse and smooth spheres. On the other hand, the rugosity being close to the theoretical value of 1.0 in turn proves a good monodispersity of the dried particles.

The specific surface area slightly increased from 0.45±0.02 m^2/g for the pure trehalose particles to 0.51±0.01 m^2/g and 0.55±0.01 m^2/g for the cases with 0.4% and 1.0% trileucine respectively, and further significantly increased to 1.28±0.04 m^2/g with higher trileucine concentration at 5.0%, which corresponds to a surface rugosity that is almost three times higher than the pure trehalose particles, proving that highly-rugose particles were produced. These results also agree with our prediction by the particle formation theory as well as SEM images that the particles gained higher level of rugosity slowly when a small fraction of trileucine was added just enough to form a thin film, while the increase of surface roughness become more significant when the shells formed much earlier in the particle drying process upon the addition of more trileucine, the shell former.

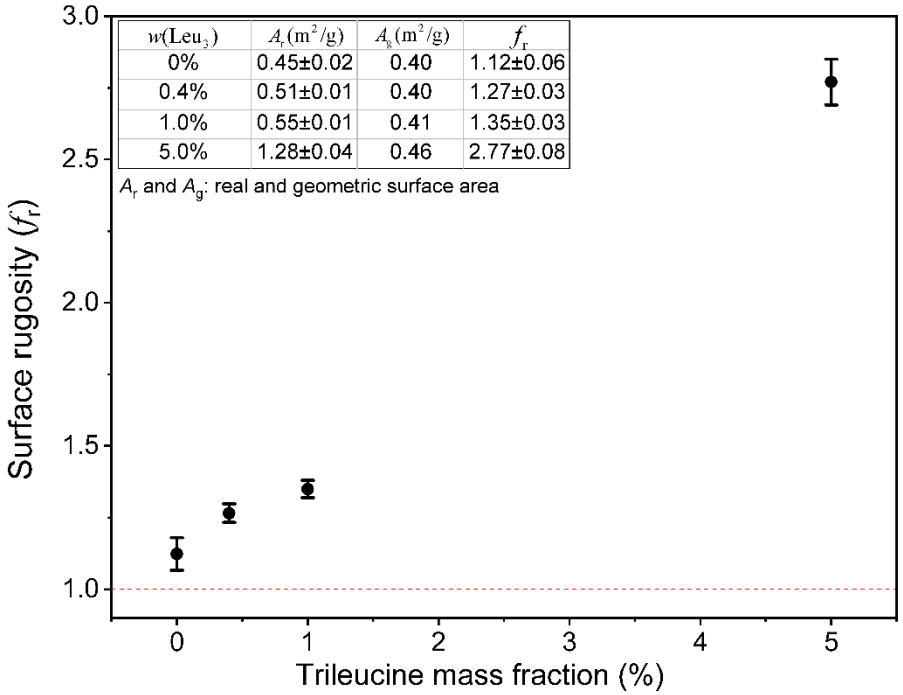

Fig. 8.

Along with the specific surface area, the BET constant that is directly related to adsorbent-adsorbate interaction energy for the first layer was also determined. Therefore, in the current study, the BET constants are indicators of the surface compositions of the formed particles. The BET constants for the samples with 0.4%, 1.0% and 5.0% trileucine were determined to be close at 13.7±0.6, 9.7±0.6, and 11.2±0.7 respectively, indicating similar surface compositions. However, the BET constant for the pure trehalose sample was determined to be different from the other three samples at 23.3±0.6. This is an indication that trileucine indeed accumulated on the particle surfaces as designed.

3.4. Effects of particle size on the suspension stability

To study the effects of particle diameter, the stabilities of suspensions with monodisperse trehalose particles of different sizes but the same concentration at 0.23% (w/w) were first measured and compared. Three suspensions were prepared for each batch of spray-dried particles and each suspension sample was measured three times for 30 min immediately after ultrasonic agitation. As their normalized relative transmission profiles show in **Fig.9**, the time-dependent transmission intensity changes over the entire height of the suspensions. Along the height axis, the profiles start at the bottom of the vial, at a normalized height of 0, and end at the top of the suspension, at a normalized height of 1. Intensity of the transmission change is also a normalized value in the range of 0 to 1. The suspensions with small, medium, and large trehalose particles destabilized very differently during the 30min-observation time. In all cases, a thin layer of settled particles was detected at the bottom of the vial, indicated by the reduced transmission intensities close to the normalized height of 0. Different levels of clarification were observed for the three different suspensions, and the level of clarification after 30 min increased substantially from less than 10% for small particles (d_a =6.0 μm) to about 60% for large particles (d_a =15.5 μm). The clarification processes occurred uniformly across the whole suspension for all the cases indicated by the simultaneously increasing transmission intensities over the whole suspension sample.

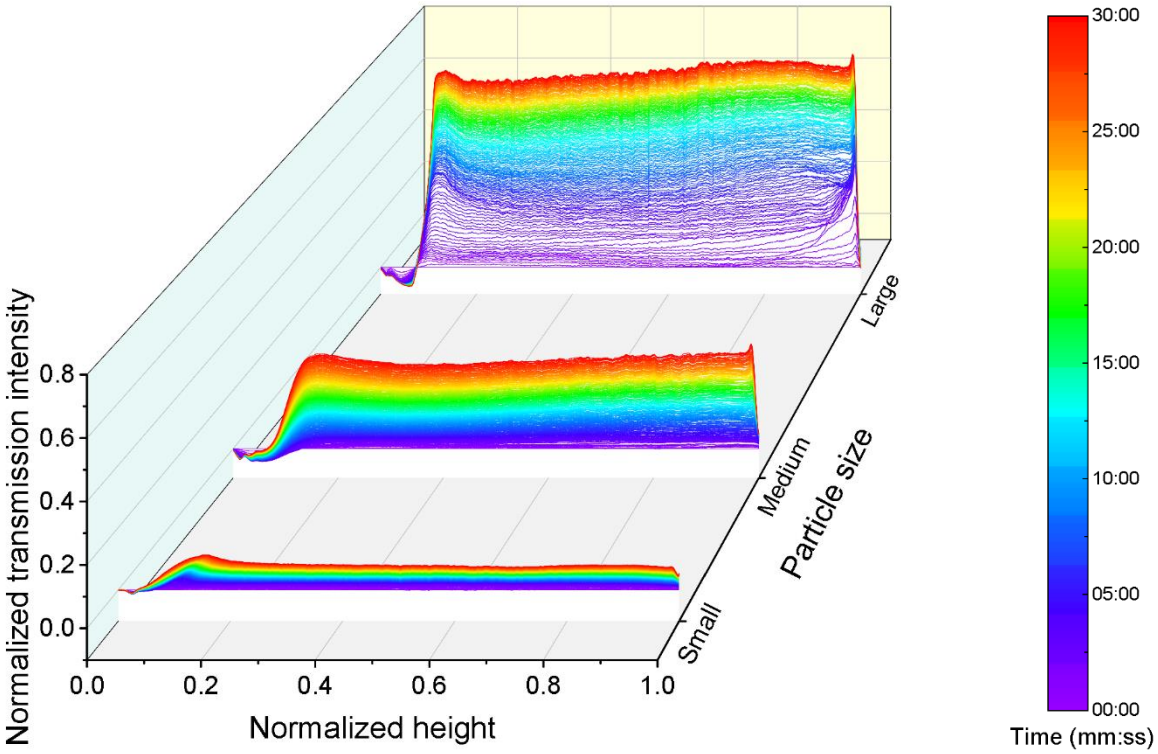

Fig.9.

Plotted in **Fig.10** are the corresponding instability indices described in Eqn.(8) for the suspensions with monodisperse trehalose particles of different sizes. Each data point corresponds to a shadowgraphic image acquired at a specific time point, and the high temporal resolution (0.5 Hz) of the suspension tester enables monitoring and comparison of the suspension stability at any time point of the destabilization process. There is a clear trend of decreasing suspension stability when the suspended particles become larger. In combination with the transmission profiles shown in **Fig.9**, the lower level of clarification for the suspension with small particles corresponds to the lower instability index plot in **Fig.10**, and vice versa. Based on the slopes of the plots, the destabilization process for the sample with large particles started rapidly from the beginning of the measurement, while the other two samples experienced slower transitions. After 30 minutes of observation, the rate of destabilization for large particles started to slow down and the instability index approached 0.7. However, the destabilization processes for the other two samples were still ongoing at the end of the observation period and showed little sign of slowing.

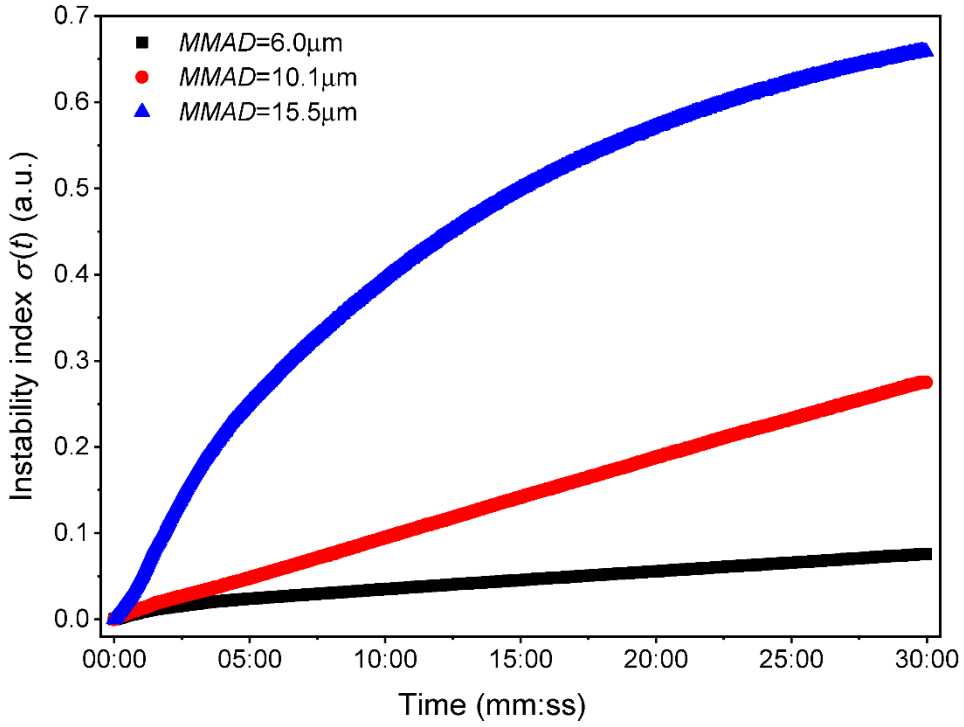

Fig.10.

To quantitatively illustrate the dependence of suspension stability on particle diameter, final instability indices at the end of the 30 min stability measurement, $\sigma(t = 30\,\mathrm{min})$, are presented in **Fig.11**. The extra point at (0, 0) represents a virtual suspension sample with infinitely small particles, which will therefore be extremely stable and show no transmission changes at all; hence, the constant instability index at 0. The error bar for each data point stands for the variation between the three repeated measurements for each suspension sample. All are relatively small, proving reproducible stability measurements. A certain level of cross-sample variation can be also observed between the suspensions containing particles of the same size, shown as the three data points for each particle diameter. Nevertheless, the instability index strongly depends on the diameter of suspended particles and demonstrated that the larger the particles the less stable the suspensions become. The suspensions with particles smaller than 5 μm remain relatively stable for at least 30min. However, increasing particle sizes beyond 5 μm will greatly impact the stability of the corresponding suspensions, and this can be explained by much faster settling velocities for

the larger particles according to Eqn.(1), in which settling velocity is proportional to d_a^2. However, the question remains whether or not aggregation plays a role. This question will be addressed in the next section.

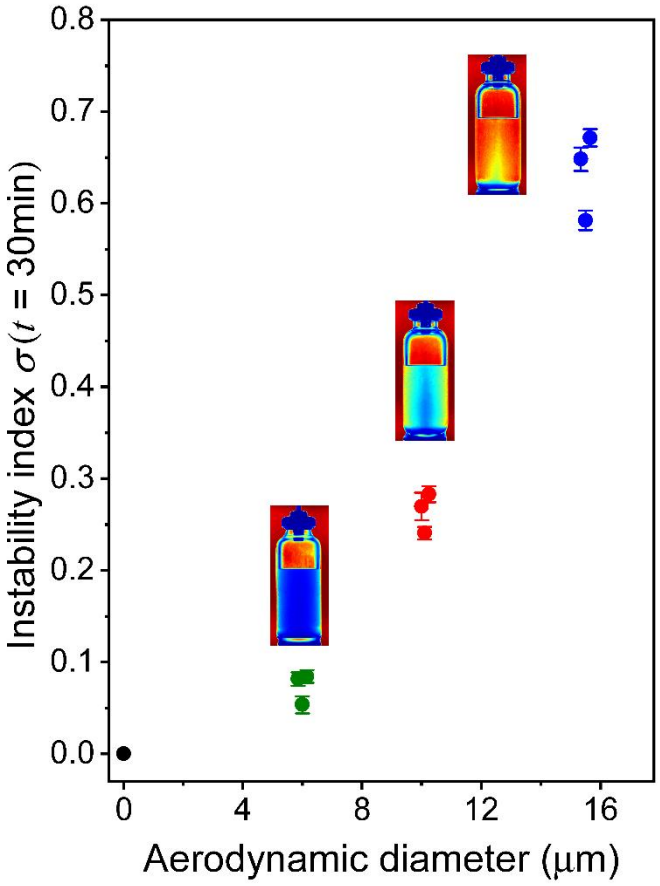

Fig.11.

3.5. Improved suspension stability with surface modification

The stability of the suspensions with particles exhibiting different levels of rugosity were also measured, and their normalized relative transmission profiles are presented in **Fig.12**. Similar to the suspensions of pure trehalose, a layer of settled particles was observed in all cases, as indicated by the reduced transmission intensity at the bottom, and the top portions of the suspensions all clarified to a certain extent after 30 minutes. The formulations with 0.4% trileucine destabilized similarly ($p > 0.1$) to the

suspension with pure trehalose, and the difference started to become significant ($p < 0.01$) when the fraction of trileucine was increased to 1.0%. The formulation with 5.0% trileucine is the most distinctive case, showing little change over the 30 min measurements and thus manifesting a significantly improved ($p < 0.002$) suspension stability.

According to Eqn.(1), particles with similar true densities and aerodynamic diameters should have close settling velocities and produce suspensions with similar colloidal stabilities. However, some of the suspensions tested here showed significantly different stabilities, proving that particle aggregation is making the difference in the destabilization process of the different suspensions. Considering that all the suspensions have the same concentration and the particles have a similar frequency of collision, it must be the changes in cohesive forces, either through surface energy or surface roughness, that is causing the different level of aggregation. Based on our earlier discussion of the theory of particle formation and also the work of Lechuga et al. (35), trileucine is likely to be on the surface of the particles in all the formulations with 0.4%, 1.0%, and 5.0% trileucine. However, only an insignificant stability improvement ($p > 0.1$) was observed for the suspensions with 0.4% trileucine when compared to the suspension of pure trehalose, indicating that surface composition of the particles is not the main factor here. This, leaves surface roughness as the only factor significantly affecting the suspension stability. It has been shown that surface roughness of microparticles is indeed the most important factor in determining the inter-particle cohesive forces (31, 48), and the change in suspension stability become significant when short-range roughness increases, as in the cases with 1.0% and 5.0% trileucine.

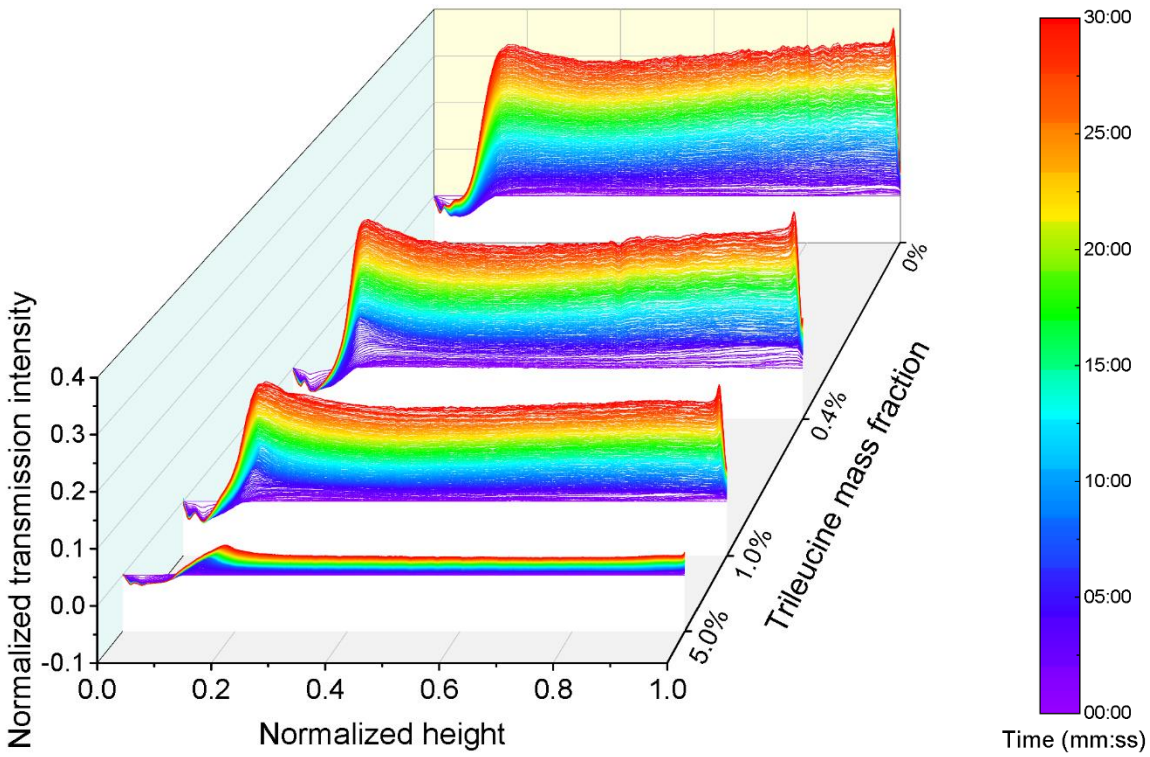

Fig.12.

In accordance with the transmission profiles, typical instability index plots for the different formulations in **Fig.13** also show different rates of destabilization as indicated by their different slopes. By comparison, the suspension with pure trehalose particles exhibiting relatively spherical and smooth surfaces destabilized the fastest. The instability index goes beyond 0.25 after 30 minutes of observation. As more trileucine was added to the formulation and the dried particles became more rugose, the suspension stability improved gradually. The 5.0% trileucine – 95.0% trehalose case that showed the best suspension stability corresponded to the most highly corrugated particles and remained stable for the entire 30 minutes. The final instability index at 30 min stayed below 0.03, which is much lower than the other cases.

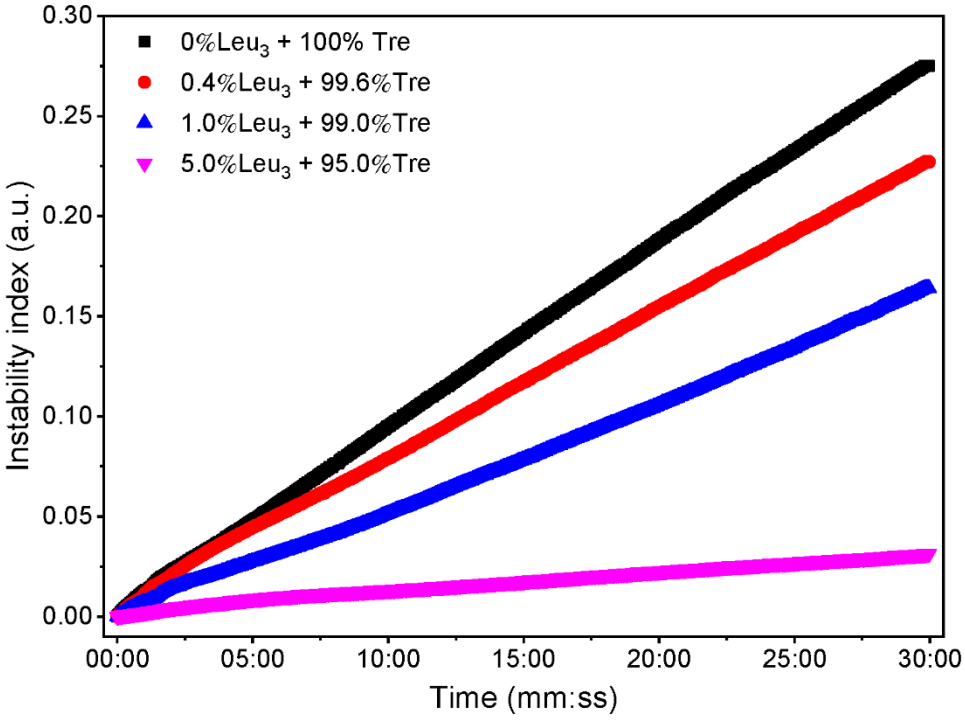

Fig.13.

A quantitative stability comparison between the suspensions is shown in **Fig.14** with the corresponding final instability indices at 30 min, $\sigma(t = 30\,\mathrm{min})$, plotted against trileucine mass fraction. The change in surface roughness caused by a small amount of trileucine in 0.4% already makes a difference in the stability of the corresponding suspensions. When the trileucine concentration was increased to 1.0% and 5.0%, the suspension stability was significantly improved by the increased surface rugosity and the instability index dropped substantially from 0.27±0.02 to 0.18±0.01 ($p < 0.01$) and 0.03±0.01 ($p < 0.002$) respectively. This result further proves that aggregation plays a major role in the settling of pure trehalose particles and is not just a factor of density difference and particle size. It is likely that the particles aggregate and settle with a larger volume equivalent diameter of the aggregate.

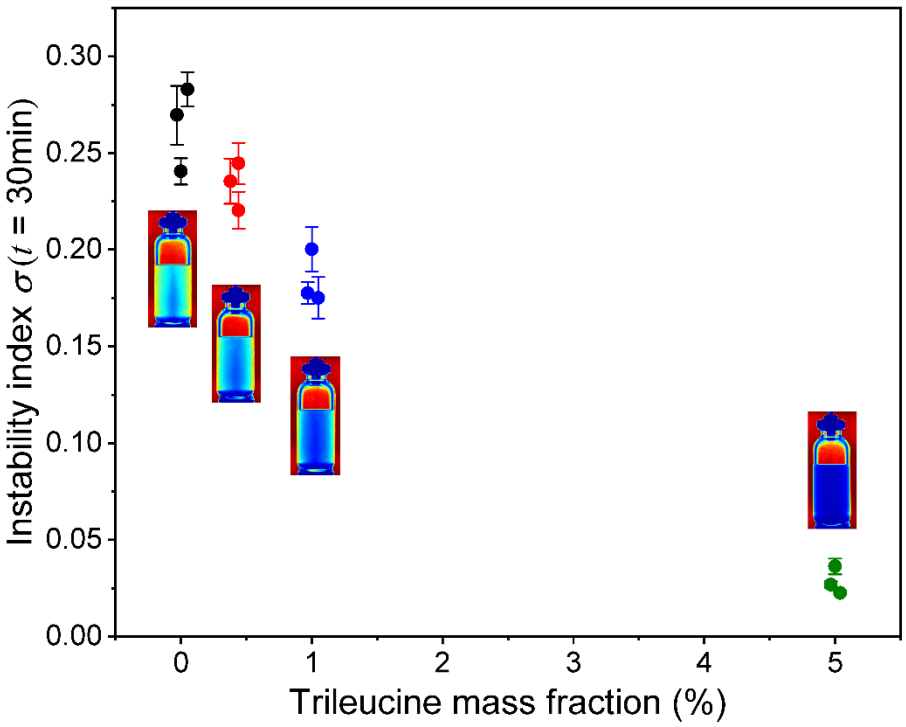

Fig.14.

Taking into consideration the change of instability index that could be caused by their slightly different particle sizes as detected and shown in **Fig.7**, the instability indices for the relatively smaller particles with 0.4% and 1.0% trileucine were expected to be slightly lower—in the range of 0.27±0.02—assuming that the dependence of suspension stability on particle size plotted in **Fig.11** is applicable in this case. However, the decrease in the instability index from the suspension with pure trehalose particles to the suspension with 0.4% and 1.0% trileucine is much more substantial than what might be caused by particle size difference. It is more obvious that the case with 5.0% trileucine, whose final instability index at 30 minute was 0.03±0.01, is even more stable than the suspension case with much smaller pure trehalose particles (*MMAD* = 5.98 μm), whose 30 min-instability index was 0.07±0.01, as shown in **Fig.11**. In comparison with the specific surface area measurement presented in **Fig.8**, the trend of improved suspension stability agrees well with the trend of increased rugosity, which is directly related to particle surface roughness,

demonstrating that that the increased surface roughness is indeed playing an important role in stabilizing the suspensions.

The significant improvement to suspension stability caused by increased particle surface rugosity can be explained by the weaker van der Waals forces of rough-surfaced particles than of particles with smooth surfaces both in air (26, 31) and propellant (30) as outlined earlier. When the particles become more corrugated, the increased surface roughness leads to a substantially reduced contact area between particles as they collide during movement in the suspension. Consequently, the macroscopic inter-particle cohesion forces are also reduced. The reduced cohesion forces in turn lead to lower chances of particle aggregation upon collision. Because of the increased surface roughness, the particles settle individually at a much slower speed with less chance of particle aggregation, and the suspension stability is much improved as a result. There may also be a tendency for the flocs to break up again if they are held together by weak forces, which may limit the maximum floc size.

4. Conclusions

The batch production of monodisperse particles using a custom-designed micro-jet atomizer offers a great opportunity to study the effects of each individual factor on suspension stability without the complications caused by polydisperse particles. For the first time, the effects of particle surface roughness on the stability of pressurized pharmaceutical suspensions are isolated and investigated in this study using monodisperse spray-dried trehalose-trileucine composite particles. The stability trend of the model suspensions of monodisperse trehalose particles with different median diameters demonstrates that the suspension stability can be significantly improved by reducing the sizes of suspended particles, which is expected based on the slower settling velocity of smaller particles. However, flocculation of particles is a key factor in suspension stability. Therefore, factors affecting flocculation, such as suspension concentration and particle cohesiveness in the propellant, need to be monitored carefully. Trileucine with

low solubility and surface activity is an effective shell former, such that a small amount of trileucine (≤ 5.0% w/w) can change the trehalose particle morphology substantially, and the final particle surface rugosity can be significantly improved by spray drying feed solutions with higher trileucine-trehalose ratios. More importantly, the suspension stability of the particles whose surface has been modified by trileucine shows a clear dependence on the surface rugosity of the suspended particles: more corrugated particles lead to more stable suspensions, and all of them are more stable than suspensions containing pure trehalose particles with relatively smooth surfaces. Therefore, in respiratory drug delivery scenarios where the drug particle diameters are restricted within a certain range (1-5 μm) for the best delivery efficiency, increasing the surface roughness of the particles, for example, by using shell formers like trileucine, is potentially a promising technique that can be used to stabilize their suspensions. This approach is likely not very dependent on the type of propellant and does not require use of a surfactant. By avoiding solubility issues with surfactants in novel propellant, this approach could prove highly useful in the transition to more environmentally friendly pMDIs.

Acknowledgments

The authors acknowledge financial support from the Natural Sciences and Engineering Research Council (NSERC) of Canada, the Alberta Ingenuity Fund and the Canadian Foundation for Innovation (CFI). Hui Wang gratefully acknowledges the scholarship support of Alberta Innovates and Alberta Advanced Education.

Appendix

The Brunauer-Emmett-Teller (BET) Method

According to the BET equation A1,

$$\frac{1}{m(\frac{P_0}{P}-1)}=\frac{C-1}{m_0C}(\frac{P}{P_0})+\frac{1}{m_0C} \quad \text{(A1)}$$

where m is the weight of adsorbed gas at a relative pressure P/P_0, m_0 is the weight of adsorbate constituting a monolayer of surface coverage for each unit mass of sample, and C is the BET constant that is indicative of the adsorbate-adsorbent interaction energy, the krypton adsorption isotherm is plotted as $1/m(\frac{P_0}{P}-1)$ against P/P_0, leading to a linearized BET plot shown in **Fig.A1**. From Eqn.(A1), the slope, s, and intercept, i, of the plot can be obtained as:

$$s=\frac{C-1}{m_0C} \quad \text{(A2)}$$

and

$$i=\frac{1}{m_0C} \quad \text{(A3)}$$

The weight of adsorbate gas for a monolayer coverage can therefore be calculated by combining equations (A2) and (A3) that:

$$m_0=\frac{1}{s+i} \quad \text{(A4)}$$

and the BET constant is:

$$C=1+\frac{s}{i} \quad \text{(A5)}$$

Specific surface area of the tested sample, S, can therefore be determined as:

$$S=\frac{m_0N_{\mathrm{A}}A_{\mathrm{cr}}}{M_{\mathrm{Kr}}} \quad \text{(A6)}$$

in which N_A is the Avogadro's constant, A_{cr} and M_{Kr} is the cross-sectional area of a single adsorbate gas molecule and the gas molecular weight respectively. Listed in **Table A1** is the measured data and calculated results.

Table A1. Data used for the determination of particle specific surface area and BET constant

Sample	Slope, s	Intercept, i	R^2	Weight of monolayer, m_0 (mg)	BET constant, C	Specific surface area, S (m^2/g)
0% Tri	3148±20	141±4	>0.999	0.30±0.01	23.3±0.6	0.45±0.02
0.4% Tri	2682±73	211±14	0.996	0.35±0.01	13.7±0.9	0.51±0.01
1.0% Tri	2397±89	275±16	0.992	0.37±0.01	9.7±0.6	0.55±0.01
5.0% Tri	1053±35	103±6	0.993	0.87±0.02	11.2±0.7	1.28±0.02

615

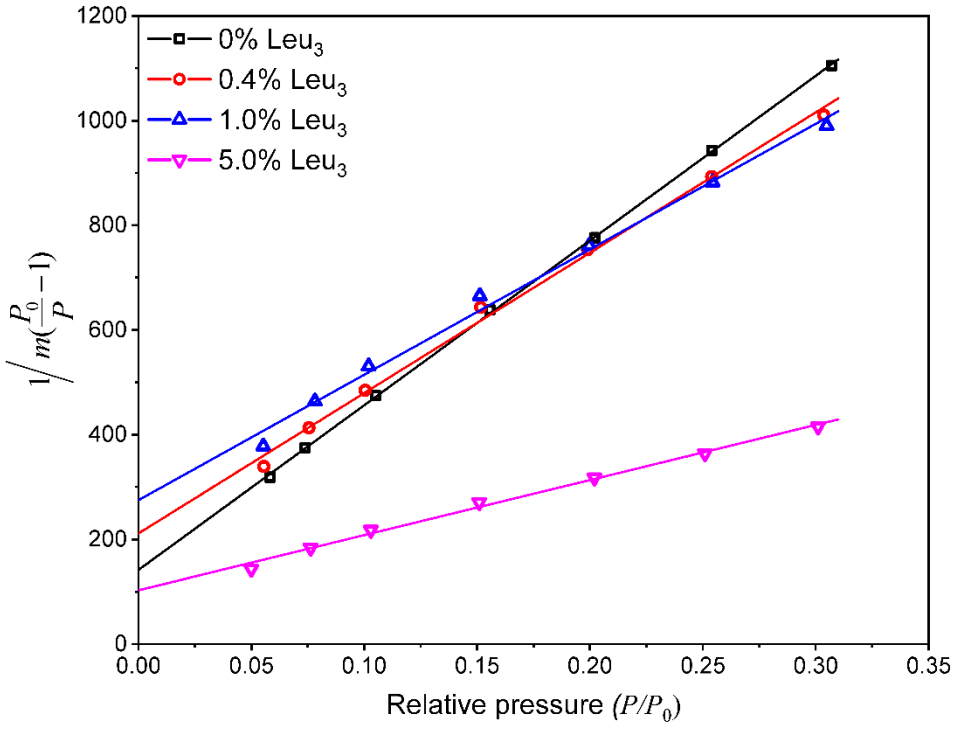

Fig. A1.

Morphology of Particles Extracted From the Propellant

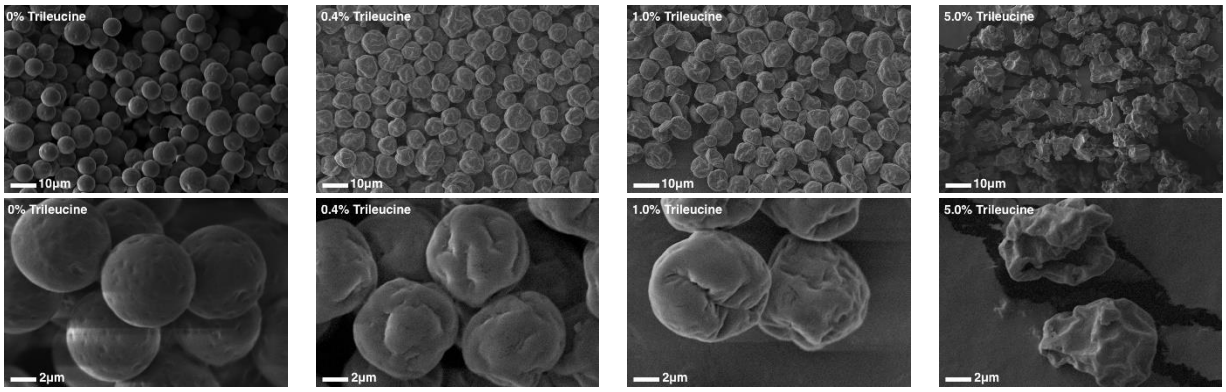

Fig. A2.

References

1. Vasconcelos T, Sarmento B, Costa P. Solid dispersions as strategy to improve oral bioavailability of poor water soluble drugs. Drug Discov Today. 2007;12(23):1068-1075.
2. Kipp J. The role of solid nanoparticle technology in the parenteral delivery of poorly water-soluble drugs. Int J Pharm. 2004;284(1-2):109-122.
3. Huang J, Wigent RJ, Bentzley CM, Schwartz JB. Nifedipine solid dispersion in microparticles of ammonio methacrylate copolymer and ethylcellulose binary blend for controlled drug delivery: Effect of drug loading on release kinetics. Int J Pharm. 2006;319(1-2):44-54.
4. Müller RH, MaÈder K, Gohla S. Solid lipid nanoparticles (SLN) for controlled drug delivery–a review of the state of the art. Eur J Pharm Biopharm. 2000;50(1):161-177.
5. Kleinstreuer C, Zhang Z, Donohue J. Targeted drug-aerosol delivery in the human respiratory system. Annu Rev Biomed Eng. 2008;10:195-220.
6. Heyder J. Deposition of inhaled particles in the human respiratory tract and consequences for regional targeting in respiratory drug delivery. Proc Am Thorac Soc. 2004;1(4):315-320.
7. Ooi J, Traini D, Boyd BJ, Gaisford S, Young PM. Determination of physical and chemical stability in pressurised metered dose inhalers: potential new techniques. Expert Opin Drug Deliv. 2015;12(10):1661-1675.
8. Stein SW, Sheth P, Hodson PD, Myrdal PB. Advances in metered dose inhaler technology: hardware development. AAPS PharmSciTech. 2014;15(2):326-338.
9. Ivey JW, Vehring R, Finlay WH. Understanding pressurized metered dose inhaler performance. Expert Opin Drug Deliv. 2015;12(6):901-916.
10. DeCarlo PF, Slowik JG, Worsnop DR, Davidovits P, Jimenez JL. Particle morphology and density characterization by combined mobility and aerodynamic diameter measurements. Part 1: Theory. Aerosol Sci Technol. 2004;38(12):1185-1205.
11. Israelachvili JN. Intermolecular and surface forces: revised third edition: Academic Press; 2011.

12. Johnson KA. Interfacial phenomena and phase behavior in metered dose inhaler formulations. In. Lung Biology in Health and Disease; 1996. p. 385-415.
13. Rogueda P. Novel hydrofluoroalkane suspension formulations for respiratory drug delivery. Expert Opin Drug Deliv. 2005;2(4):625-638.
14. Finlay WH. The mechanics of inhaled pharmaceutical aerosols: an introduction: Academic Press; 2001.
15. Myrdal PB, Sheth P, Stein SW. Advances in metered dose inhaler technology: formulation development. AAPS PharmSciTech. 2014;15(2):434-455.
16. Arora P, Kumar L, Vohra V, Sarin R, Jaiswal A, Puri M, Rathee D, Chakraborty P. Evaluating the technique of using inhalation device in COPD and bronchial asthma patients. Respir Med. 2014;108(7):992-998.
17. Dellamary LA, Tarara TE, Smith DJ, Woelk CH, Adractas A, Costello ML, Gill H, Weers JG. Hollow porous particles in metered dose inhalers. Pharm Res. 2000;17(2):168-174.
18. Hirst PH, Pitcairn GR, Weers JG, Tarara TE, Clark AR, Dellamary LA, Hall G, Shorr J, Newman SP. In vivo lung deposition of hollow porous particles from a pressurized metered dose inhaler. Pharm Res. 2002;19(3):258-264.
19. Rabinow BE. Nanosuspensions in drug delivery. Nat Rev Drug Discov. 2004;3(9):785.
20. Patravale V, Kulkarni R. Nanosuspensions: a promising drug delivery strategy. J Pharm Pharmacol. 2004;56(7):827-840.
21. Lieberman HA, Rieger MM, Banker GS. Pharmaceutical dosage forms: Disperse systems: Marcel Dekker, New York; 1996.
22. Smyth HD. The influence of formulation variables on the performance of alternative propellant-driven metered dose inhalers. Adv Drug Del Rev. 2003;55(7):807-828.
23. Williams RO, Repka M, Liu J. Influence of propellant composition on drug delivery from a pressurized metered-dose inhaler. Drug Dev Ind Pharm. 1998;24(8):763-770.
24. Wu L, Zhang J, Watanabe W. Physical and chemical stability of drug nanoparticles. Adv Drug Del Rev. 2011;63(6):456-469.
25. Selvam P, Peguin RP, Chokshi U, da Rocha SR. Surfactant design for the 1, 1, 1, 2-tetrafluoroethane− water interface: ab initio calculations and in situ high-pressure tensiometry. Langmuir. 2006;22(21):8675-8683.
26. Adi S, Adi H, Tang P, Traini D, Chan H-k, Young PM. Micro-particle corrugation, adhesion and inhalation aerosol efficiency. Eur J Pharm Sci. 2008;35(1-2):12-18.
27. Young PM, Price R, Lewis D, Edge S, Traini D. Under pressure: predicting pressurized metered dose inhaler interactions using the atomic force microscope. J Colloid Interface Sci. 2003;262(1):298-302.
28. Traini D, Rogueda P, Young P, Price R. Surface energy and interparticle force correlation in model pMDI formulations. Pharm Res. 2005;22(5):816-825.
29. Traini D, Young PM, Rogueda P, Price R. In vitro investigation of drug particulates interactions and aerosol performance of pressurised metered dose inhalers. Pharm Res. 2007;24(1):125-135.

30. D'Sa D, Chan H-K, Chrzanowski W. Predicting physical stability in pressurized metered dose inhalers via dwell and instantaneous force colloidal probe microscopy. Eur J Pharm Biopharm. 2014;88(1):129-135.

31. Baldelli A, Vehring R. Analysis of cohesion forces between monodisperse microparticles with rough surfaces. Colloid Surface A. 2016;506:179-189.

32. Mengual O, Meunier G, Cayré I, Puech K, Snabre P. TURBISCAN MA 2000: multiple light scattering measurement for concentrated emulsion and suspension instability analysis. Talanta. 1999;50(2):445-456.

33. Voss A, Finlay WH. Deagglomeration of dry powder pharmaceutical aerosols. Int J Pharm. 2002;248(1-2):39-50.

34. Vehring R, Foss WR, Lechuga-Ballesteros D. Particle formation in spray drying. J Aerosol Sci. 2007;38(7):728-746.

35. Lechuga-Ballesteros D, Charan C, Stults CLM, Stevenson CL, Miller DP, Vehring R, Tep V, Kuo MC. Trileucine improves aerosol performance and stability of spray-dried powders for inhalation. J Pharm Sci. 2008;97(1):287-302.

36. Azhdarzadeh M, Shemirani FM, Ruzycki CA, Baldelli A, Ivey J, Barona D, Church T, Lewis D, Olfert JS, Finlay WH, Vehring R. An atomizer to generate monodisperse droplets from high vapor pressure liquids. Atomization Sprays. 2016;26(2):121-134.

37. Ivey JW, Bhambri P, Church TK, Lewis DA, Vehring R. Experimental investigations of particle formation from propellant and solvent droplets using a monodisperse spray dryer. Aerosol Sci Technol. 2018:1-15.

38. Sirignano W, Mehring C. Review of theory of distortion and disintegration of liquid streams. Prog Energy Combust Sci. 2000;26(4-6):609-655.

39. Vehring R. Pharmaceutical particle engineering via spray drying. Pharm Res. 2008;25(5):999-1022.

40. Boraey MA, Vehring R. Diffusion controlled formation of microparticles. J Aerosol Sci. 2014;67:131-143.

41. Wang H, Barona D, Oladepo S, Williams L, Hoe S, Lechuga-Ballesteros D, Vehring R. Macro-Raman spectroscopy for bulk composition and homogeneity analysis of multi-component pharmaceutical powders. J Pharm Biomed Anal. 2017;141:180-191.

42. Rouquerol F, Rouquerol J, Sing KS, Llewellyn P, Maurin G. Adsorption by powders and porous solids: principles, methodology and applications: Academic press; 2014.

43. Wang H, Tan P, Barona D, Li G, Hoe S, Lechuga-Ballesteros D, Nobes DS, Vehring R. Characterization of the Suspension Stability of Pharmaceuticals Using a Shadowgraphic Imaging Method. Int J Pharm. 2018;548(1):128-138.

44. Zhang J, Zografi G. Water vapor absorption into amorphous sucrose-poly (vinyl pyrrolidone) and trehalose–poly (vinyl pyrrolidone) mixtures. J Pharm Sci. 2001;90(9):1375-1385.

45. Wang H, Boraey MA, Williams L, Lechuga-Ballesteros D, Vehring R. Low-frequency shift dispersive Raman spectroscopy for the analysis of respirable dosage forms. Int J Pharm. 2014;469(1):197-205.

46. Hédoux A. Recent developments in the Raman and infrared investigations of amorphous pharmaceuticals and protein formulations: A review. Adv Drug Del Rev. 2016;100:133-146.

47. Hinds WC. Aerosol technology: properties, behavior, and measurement of airborne particles. New York: John Wiley & Sons; 2012.

48. Cheng W, Dunn P, Brach R. Surface roughness effects on microparticle adhesion. J Adhes. 2002;78(11):929-965.

Legend to Figures

Fig.1. Schematic of monodisperse micro-jet atomizer.

Fig.2. Morphology of the spray-dried pure trehalose particles shows a high level of sphericity and good monodispersity. Particle size increased with the feed solution concentration.

Fig.3. Morphology of the monodisperse spray-dried particles gradually changed from smooth to highly rugose when the concentration of trileucine was increased from 0% to 5.0%.

Fig.4. Reference spectra of crystalline trehalose (c-Tre), amorphous trehalose (a-Tre), crystalline trileucine (c-Leu_3), and amorphous trileucine (a-Leu_3). Bottom trace is a residual spectrum (Res.) arrived at by subtracting amorphous trehalose from the spectrum of trileucine-modified trehalose particles (95.0%Tre-5.0%Tri), proving the amorphous state for both trehalose and trileucine.

Fig.5. Aerodynamic size distributions of the spray-dried trehalose particles show high monodispersity with narrow distributions (*GSD* < 1.2). The corresponding *MMAD* increased from 6.0 μm to 15.5 μm with increasing feed solution concentrations.

Fig.6. Cumulative volume equivalent diameter distributions of the spray-dried trehalose particles measured directly from the SEM images. The results agree well with the aerodynamic diameter distributions measured by the aerodynamic particle sizer.

Fig.7. Particle size distributions of the spray-dried trehalose-trileucine particles show high monodispersity for formulations with different trileucine mass fractions. The mass median aerodynamic diameters decreased slightly due to the increased particle rugosity caused by the increase in trileucine mass fraction from 0% to 5.0%.

Fig. 8. Surface rugosity ($f_r = A_r / A_g$) of the monodisperse spray-dried particles increased gradually as more trileucine was added to the feed solution. Insert table shows the real and geometric specific surface area used for the calculation of rugosity. Dotted base-line corresponds to a rugosity of 1.0 for perfectly smooth and spherical particles.

Fig.9. Normalized relative transmission profiles of the pressurized suspensions indicate that suspension stability strongly depends on the diameter of suspended particles. The suspension with large particles destabilized much more, and much faster, than those with smaller particles.

Fig.10. Instability index plots for suspensions of different trehalose particles show that larger particles lead to faster destabilization of the corresponding suspension.

Fig.11. Comparison of the final instability indices at 30 min, $\sigma(t = 30\,\mathrm{min})$, for different suspensions shows a strong dependence of suspension stability on particle diameter. Three independent suspension

760 samples were prepared for each group of particles, and each suspension was measured three times for its suspension stability. Inset shadowgraphic images represent end state of the suspension after 30 minutes measurement.

Fig.12. Normalized relative transmission profiles indicate a slower destabilization process as more trileucine is added to the formulation and the suspended particles become more wrinkled.

765 **Fig.13.** Instability index plot for suspensions of particles with different rugosity show that the increased surface roughness by trileucine improves suspension stability and reduces the rate of the destabilization process.

Fig.14. Instability indices $\sigma(t = 30\,\mathrm{min})$ for suspensions with particles of different rugosity. The suspension stability improves as the trileucine mass fraction increases and particles become more
770 wrinkled. Inset shadowgraphic images represent end state of the suspension after 30 minutes measurement.

Fig. A1. Linear region of the krypton adsorption isotherm used for the determination of specific surface area and BET constant

Fig. A2. Images of particles extracted from the propellant showing no significant changes of morphology.

FIG01

Click here to access/download;Figure;FIG01 - Atomizer Schematic.tiff

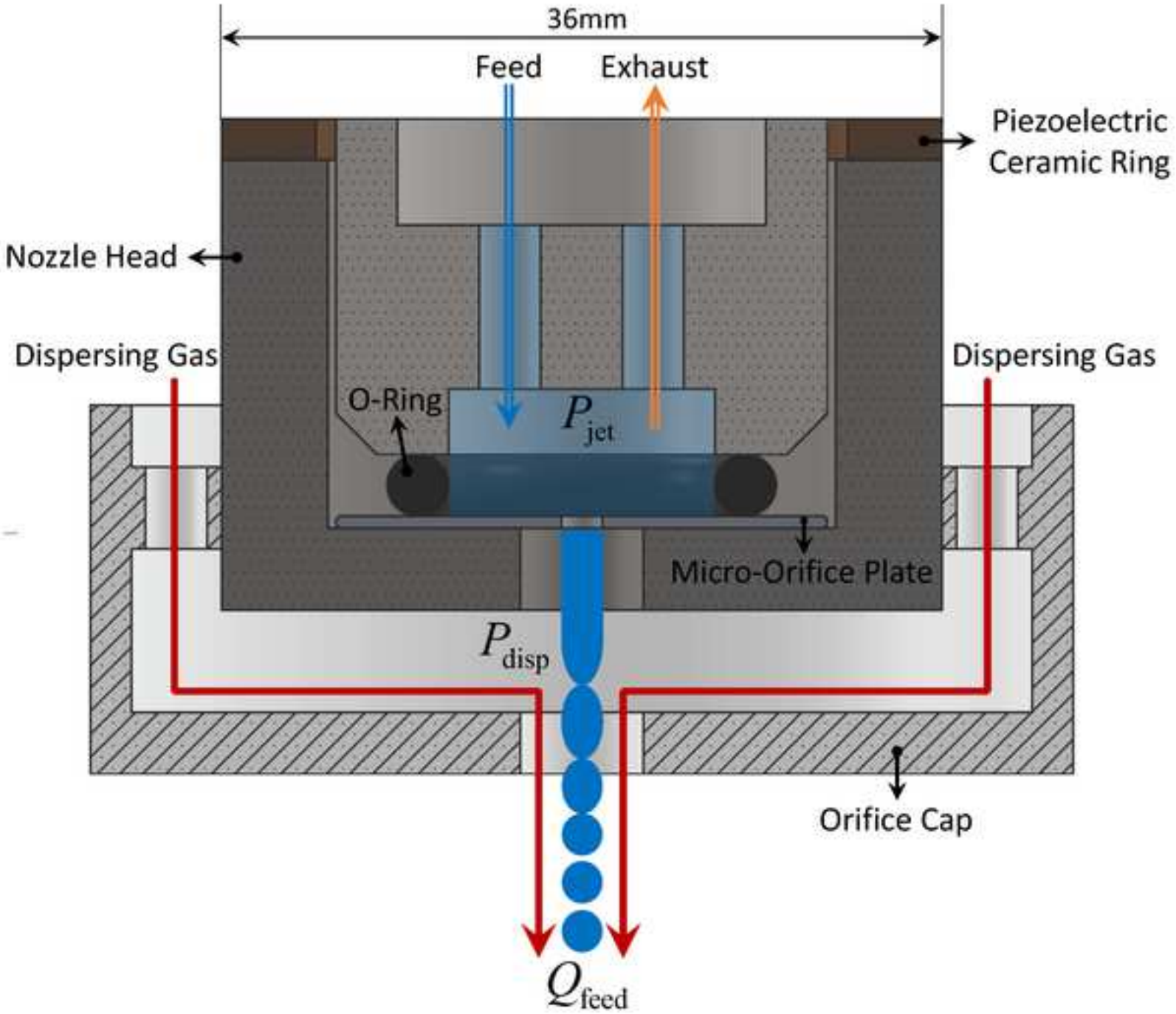

FIG02a1

Click here to access/download;Figure;FIG02a1 - Tre - 1mgmL - LowMag.tif

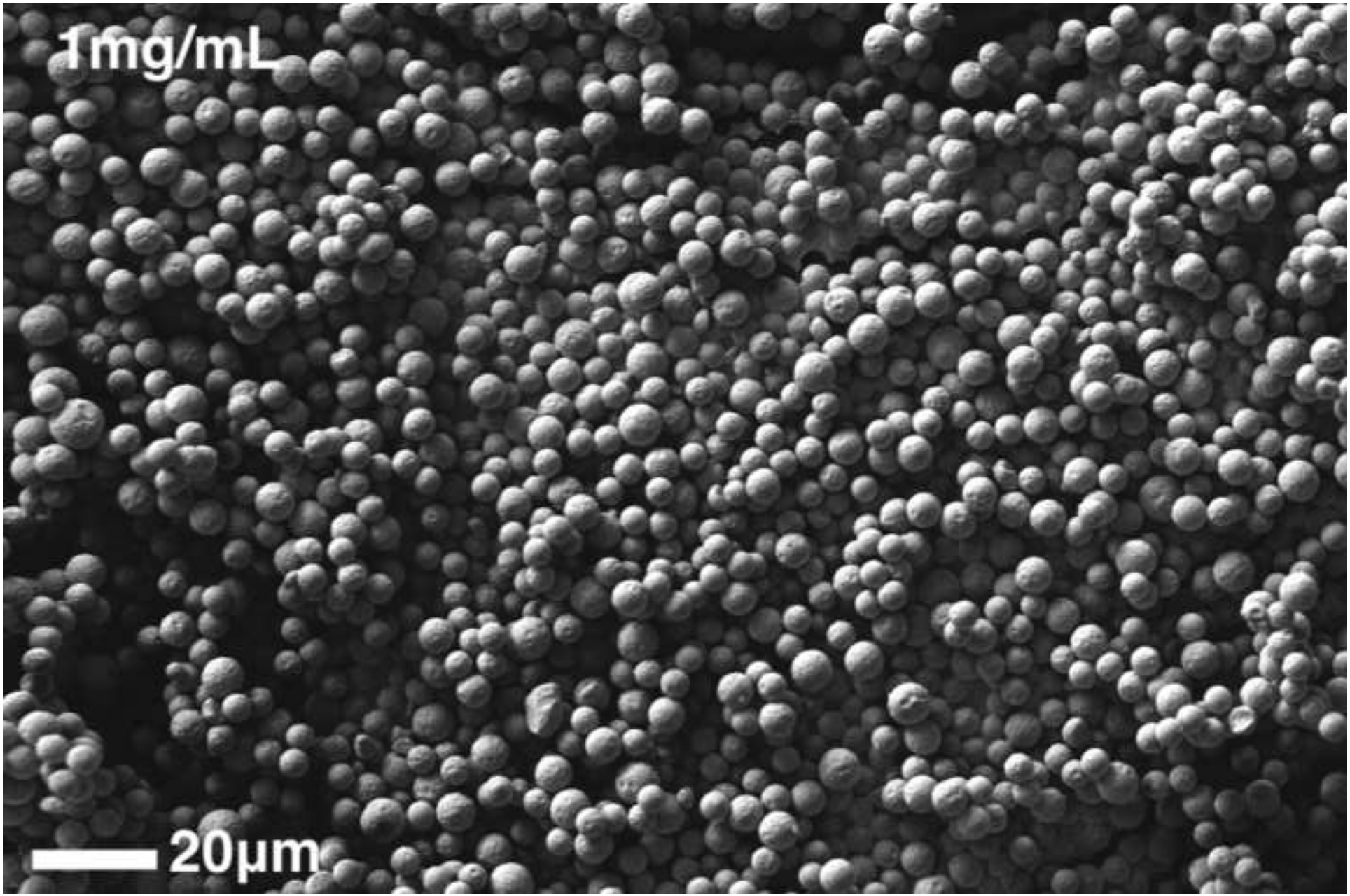

Click here to access/download;Figure;FIG02a2 - Tre - 1mgmL - HighMag.tif

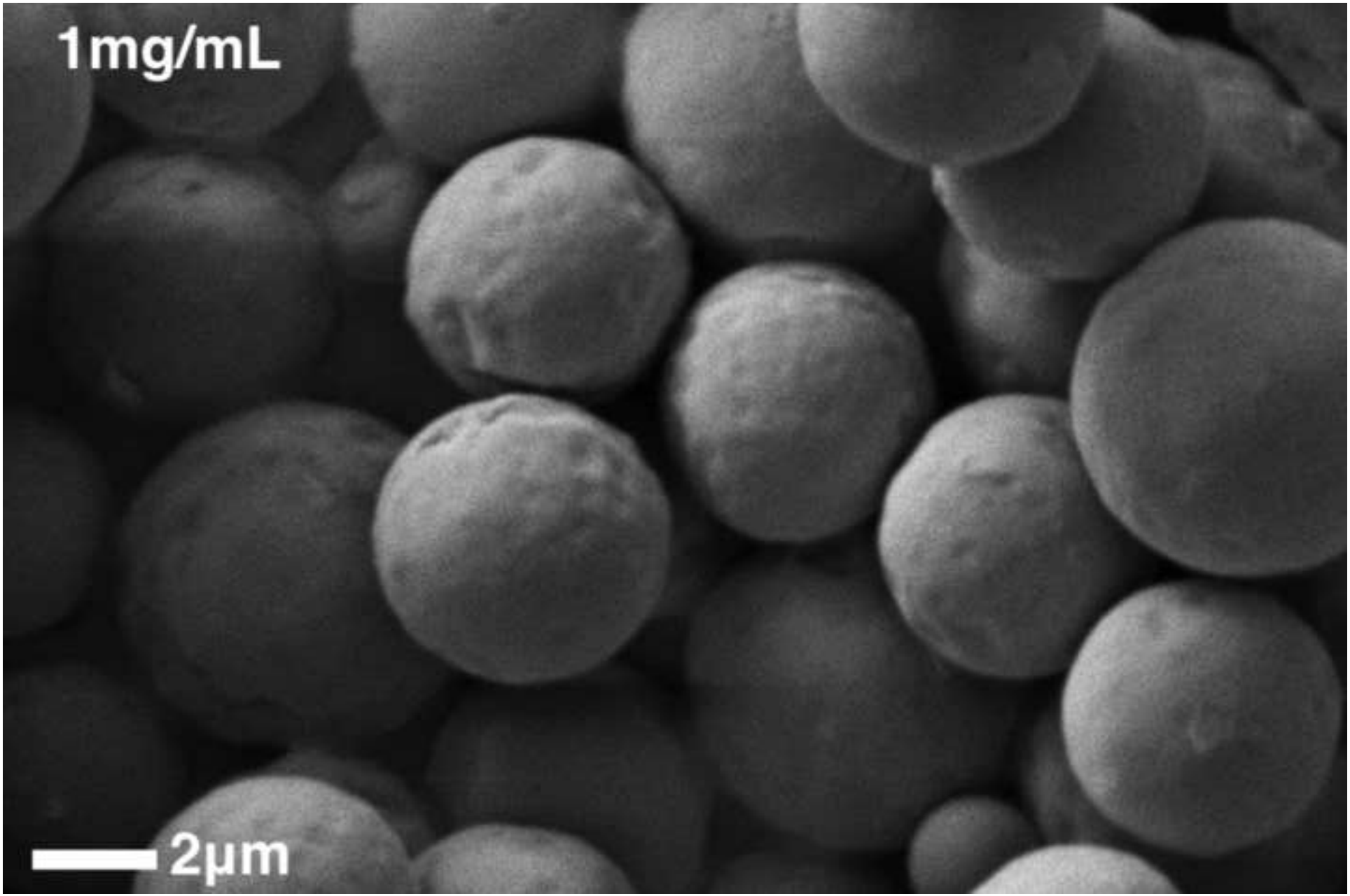

FIG02b1

Click here to access/download;Figure;FIG02b1 - Tre - 5mgmL - LowMag.tif

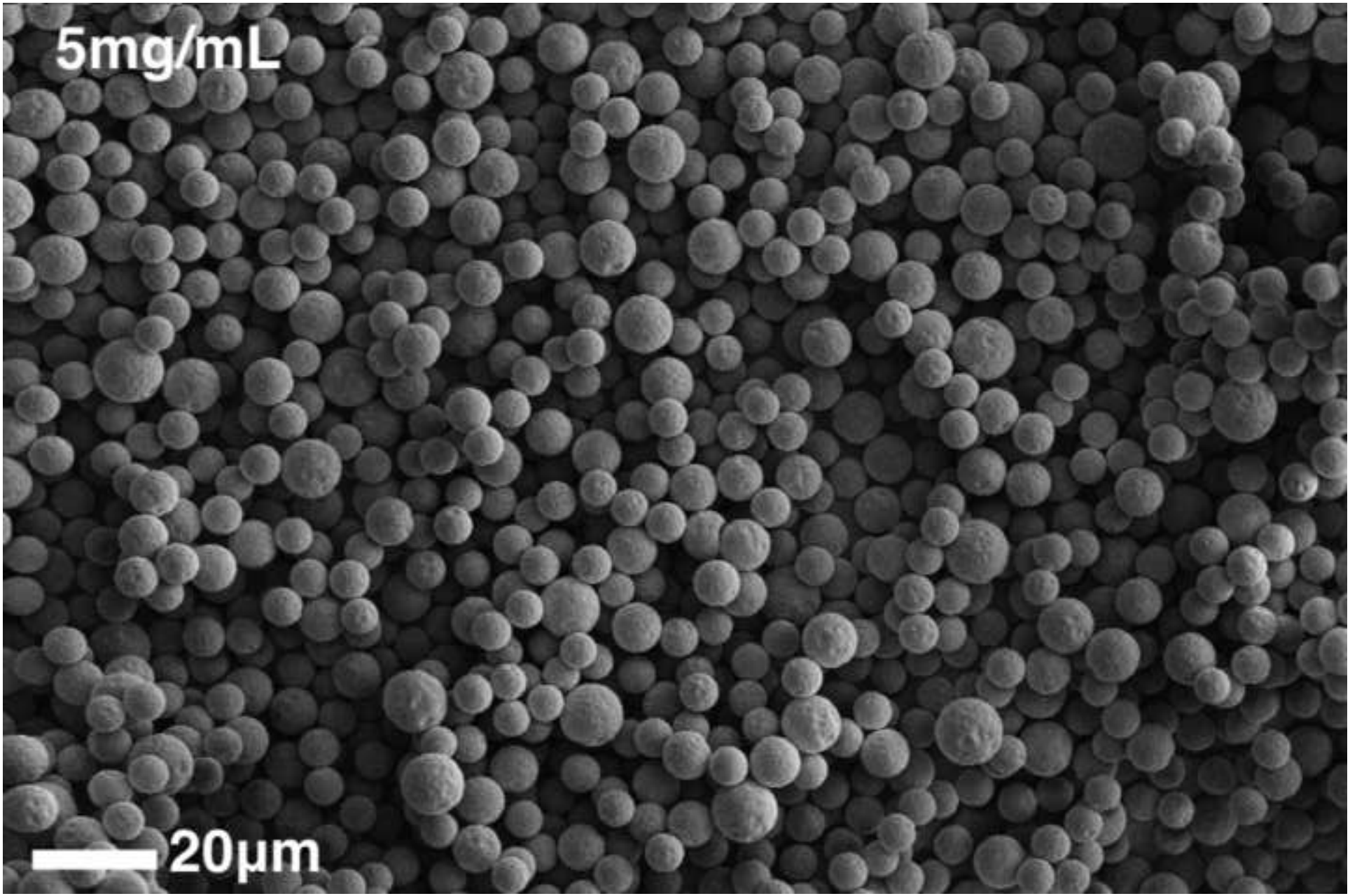

FIG02b2

Click here to access/download;Figure;FIG02b2 - Tre - 5mgmL - HighMag.tif

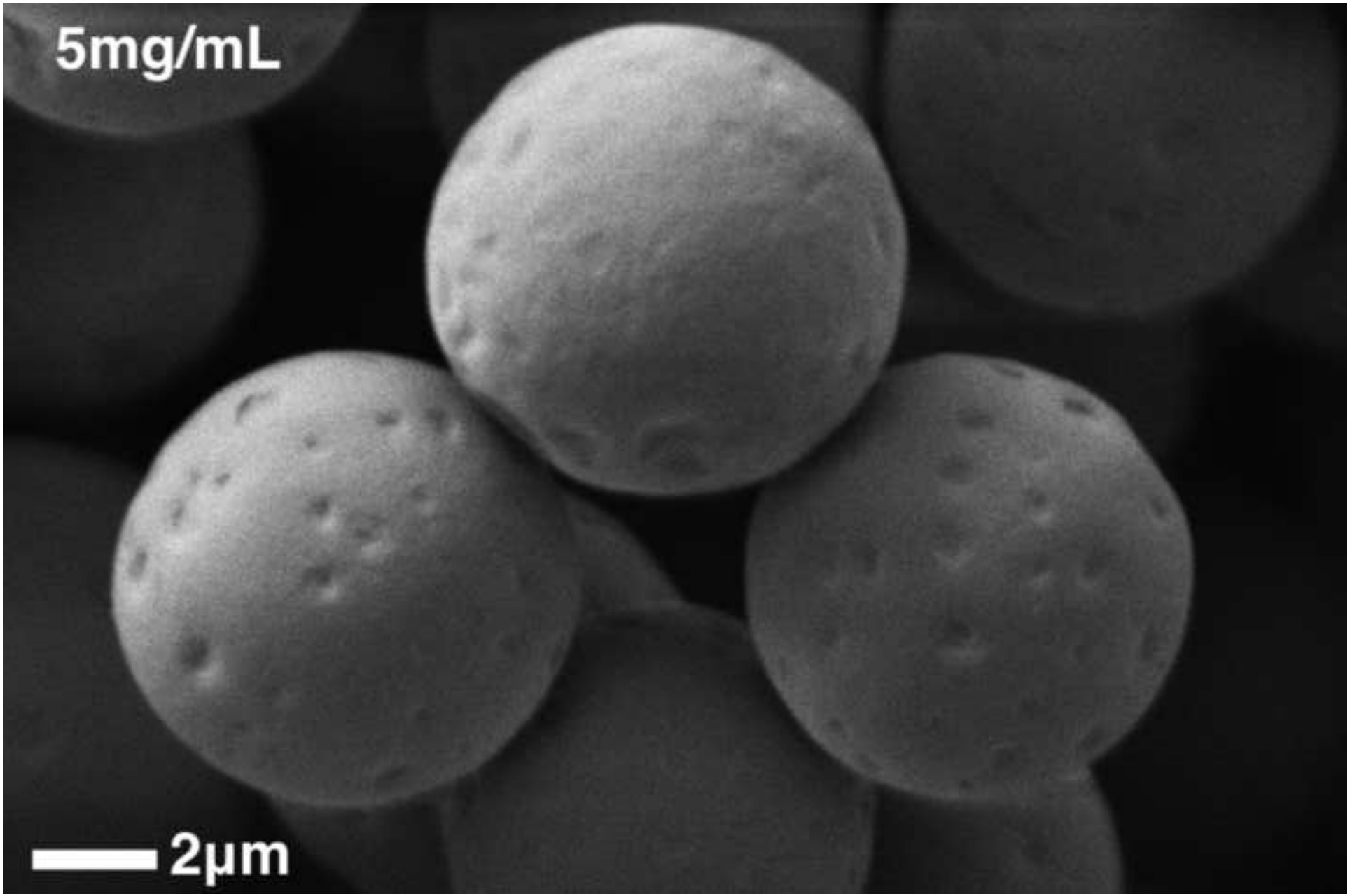

FIG02c1

Click here to access/download;Figure;FIG02c1 - Tre - 30mgmL - LowMag.tif

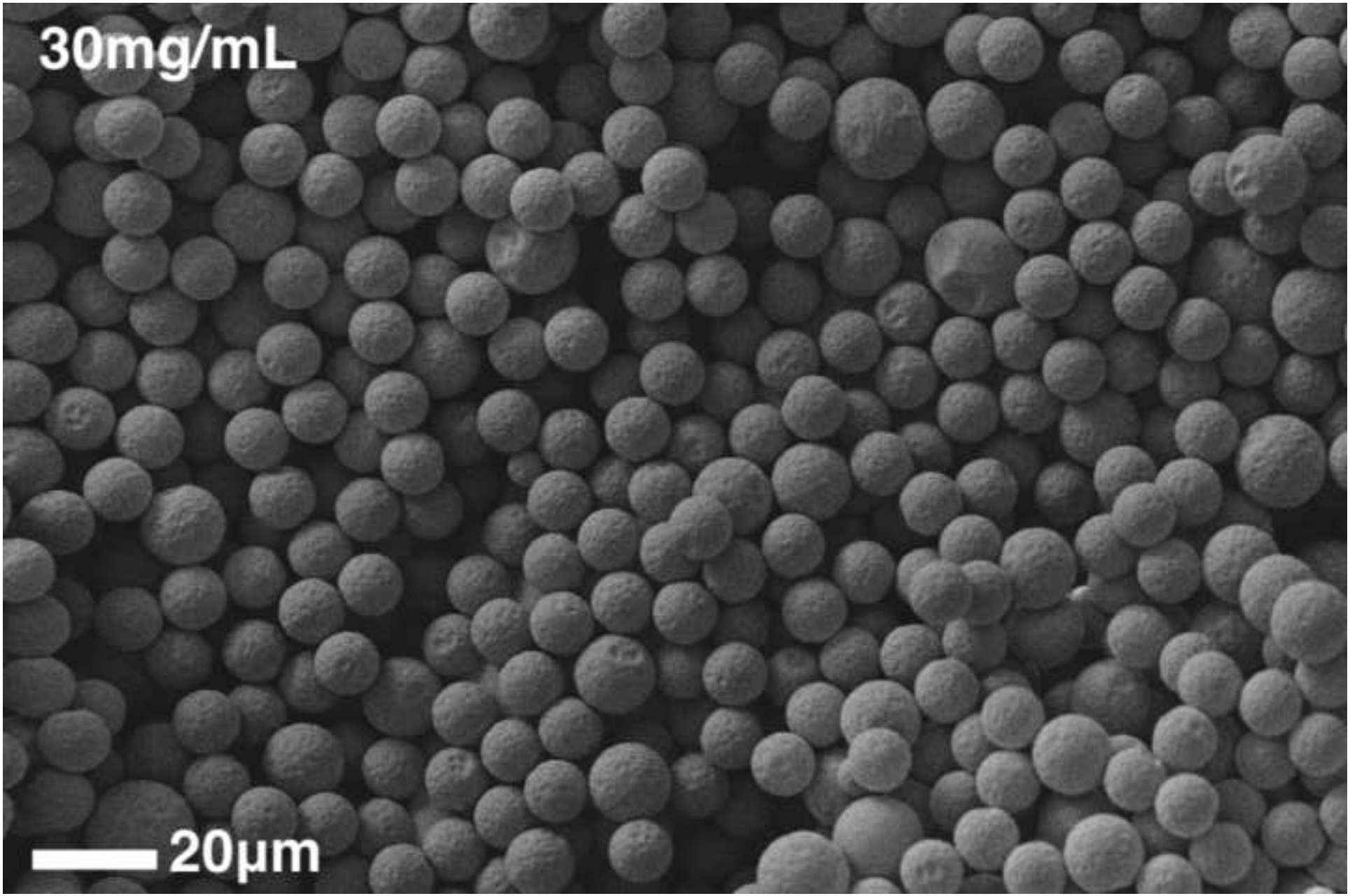

FIG02c2

Click here to access/download;Figure;FIG02c2 - Tre - 30mgmL - HighMag.tif

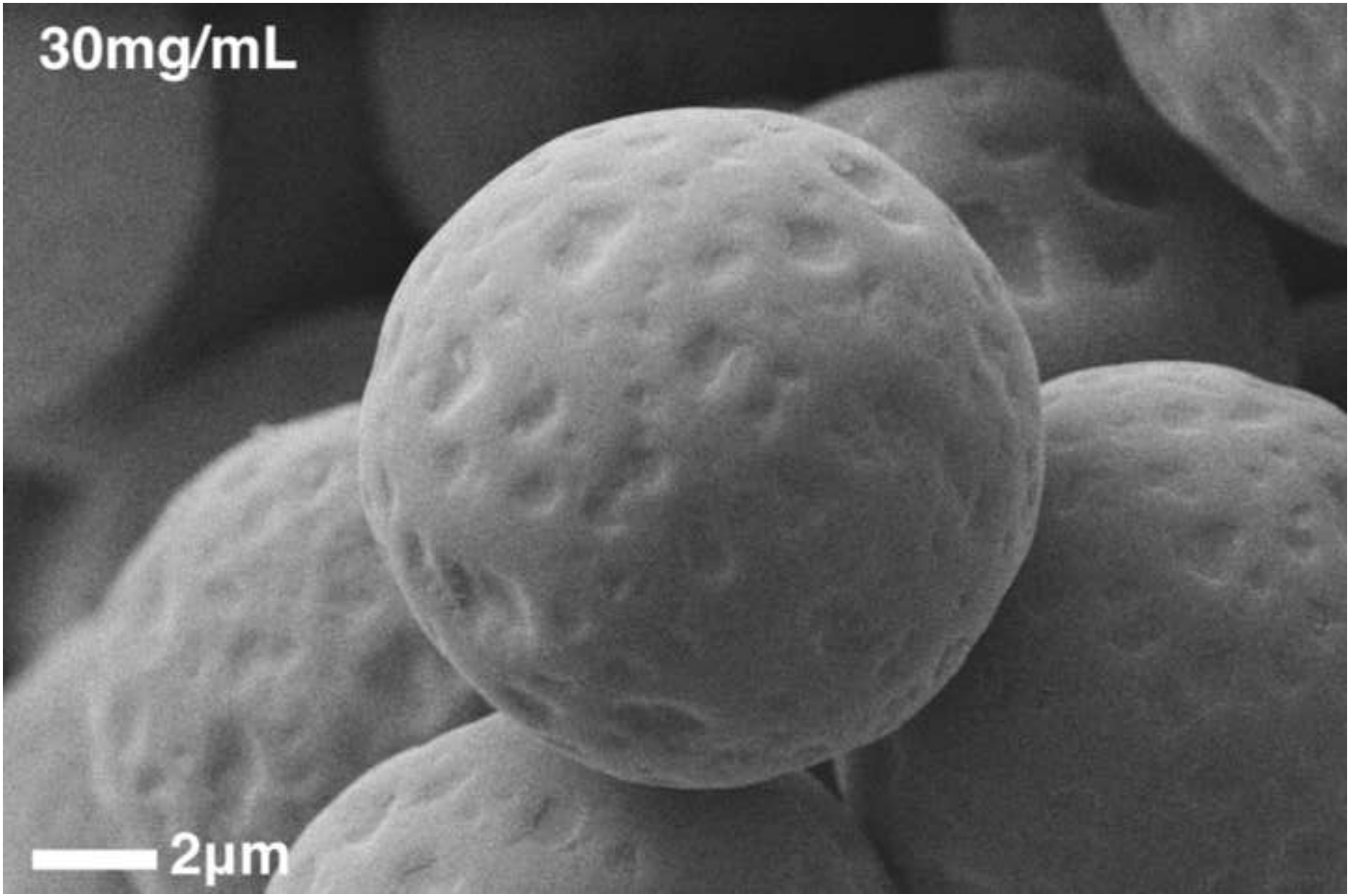

Click here to access/download;Figure;FIG03a1 - Tre-LowMag.tif

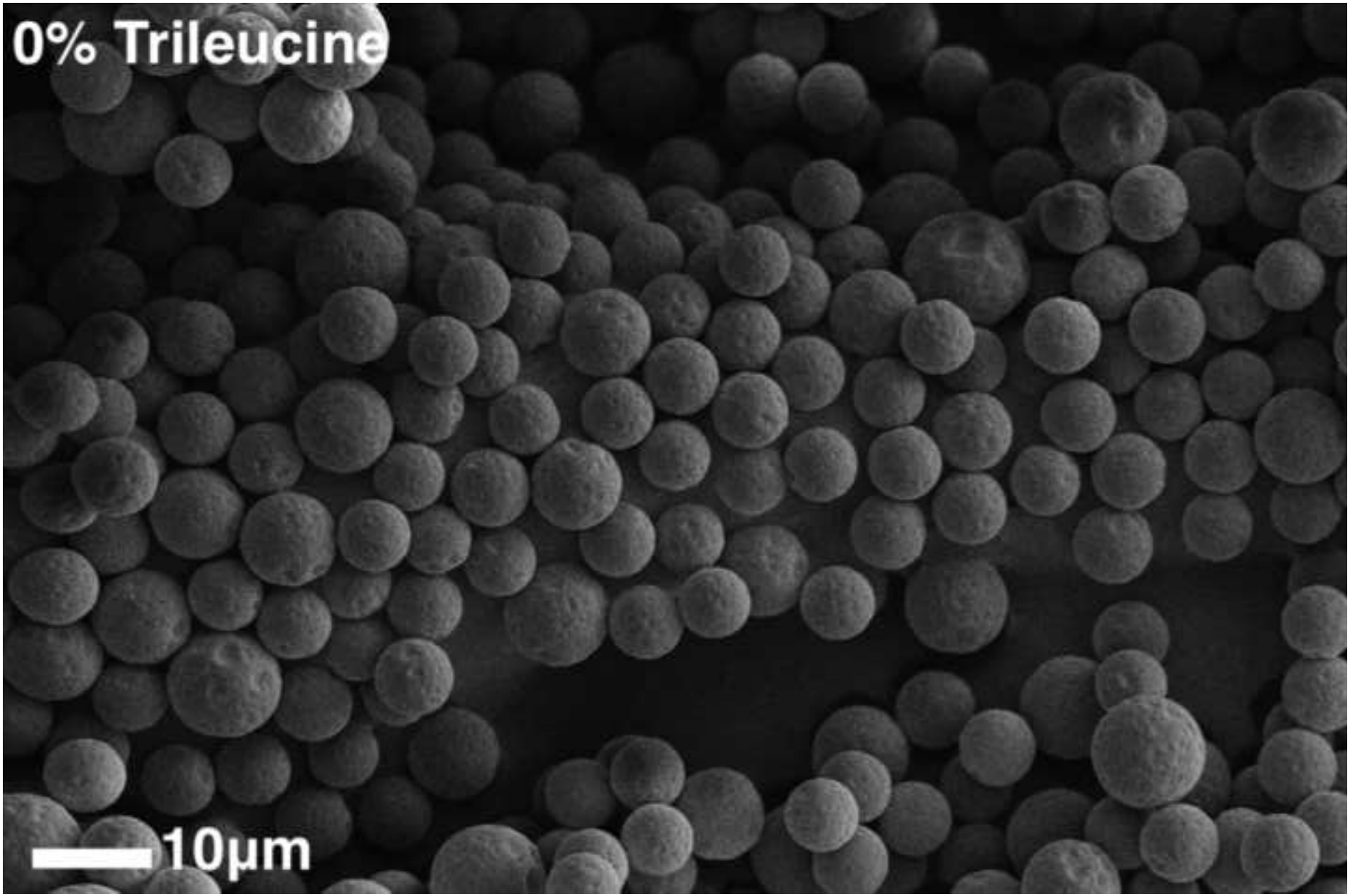

Click here to access/download;Figure;FIG03a2 - Tre-MedMag.tif

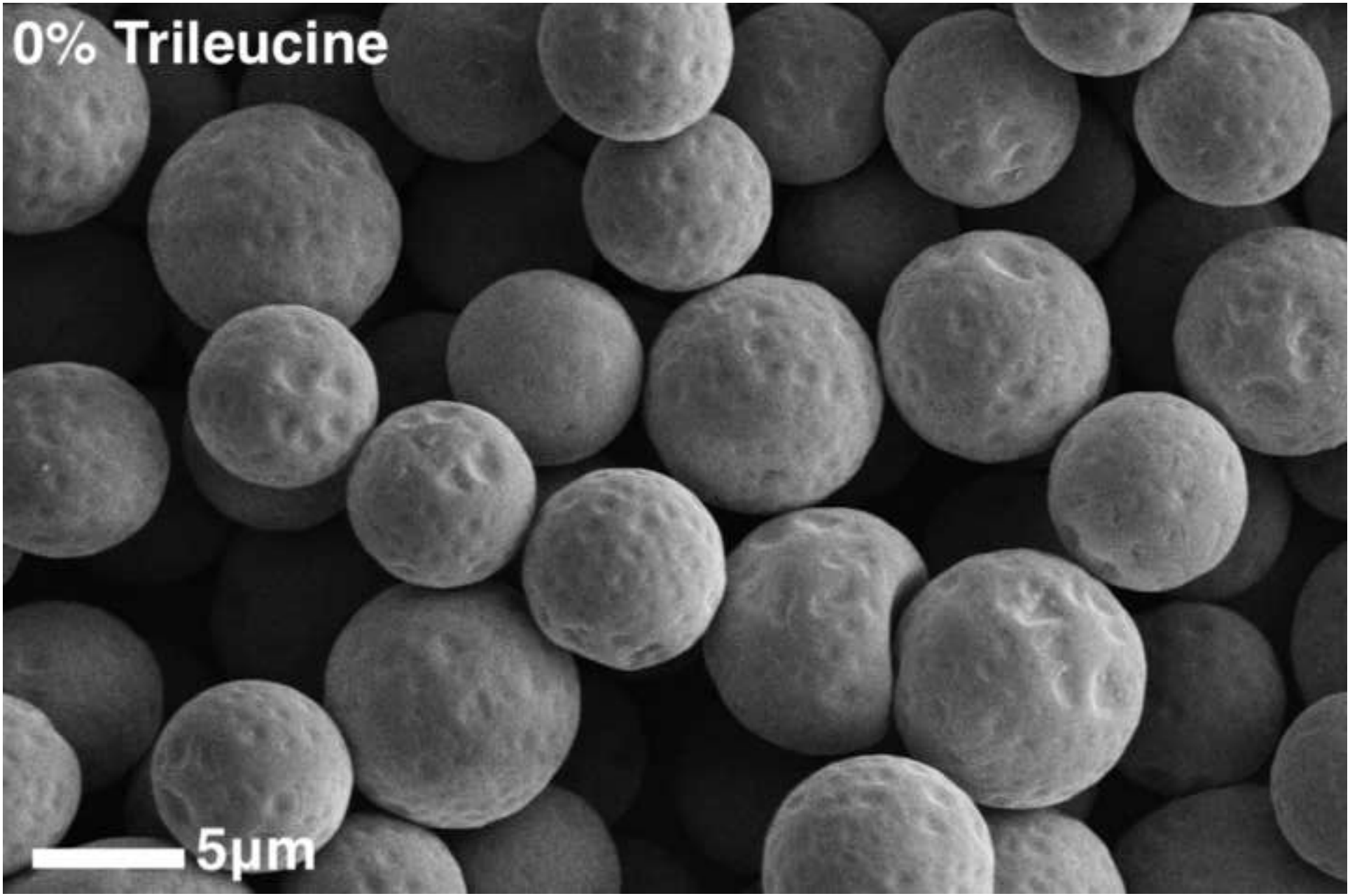

FIG03a3

Click here to access/download;Figure;FIG03a3 - Tre-HighMag.tif

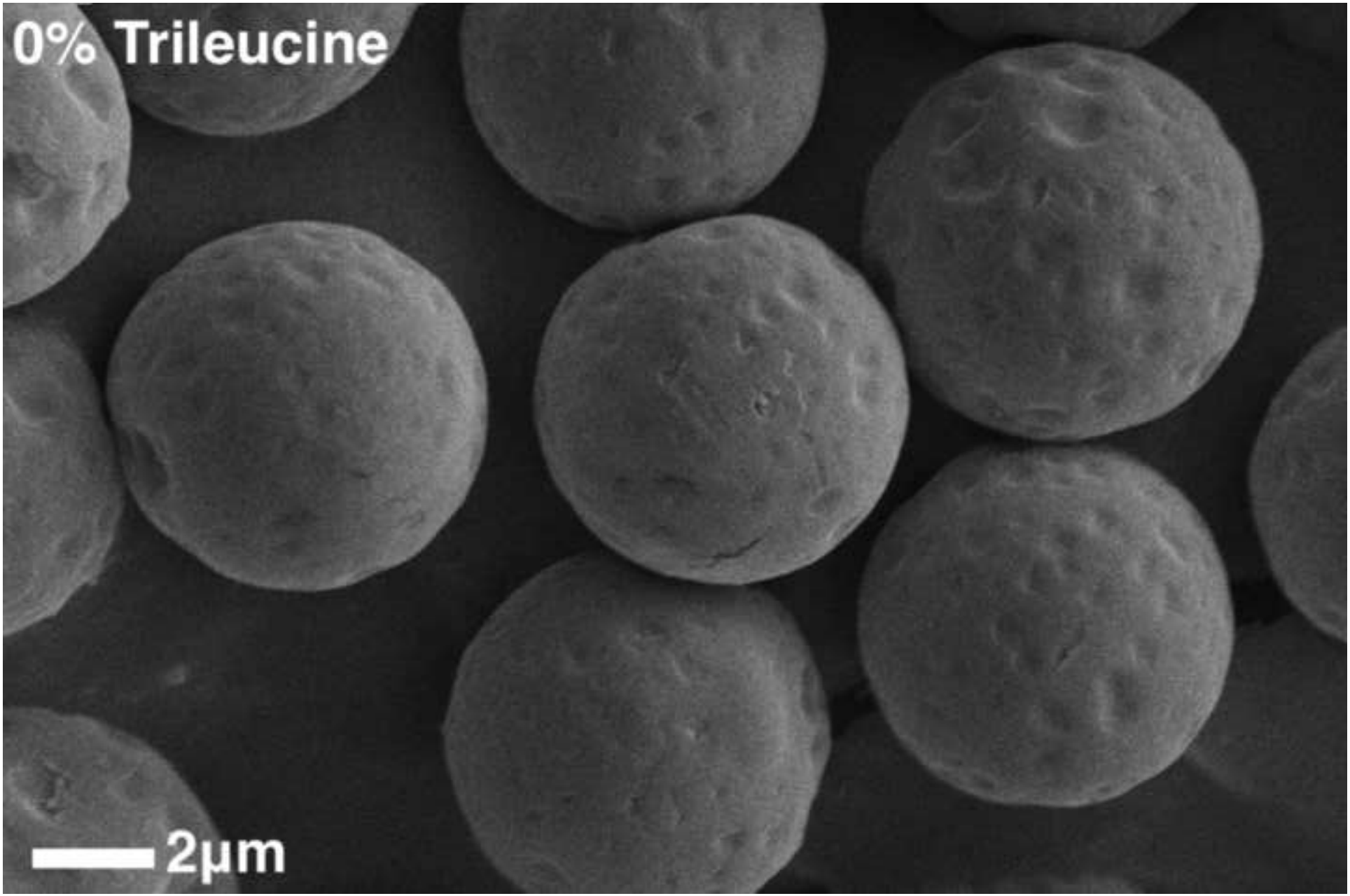

Click here to access/download;Figure;FIG03b1 - 0.4Tri-LowMag.tif

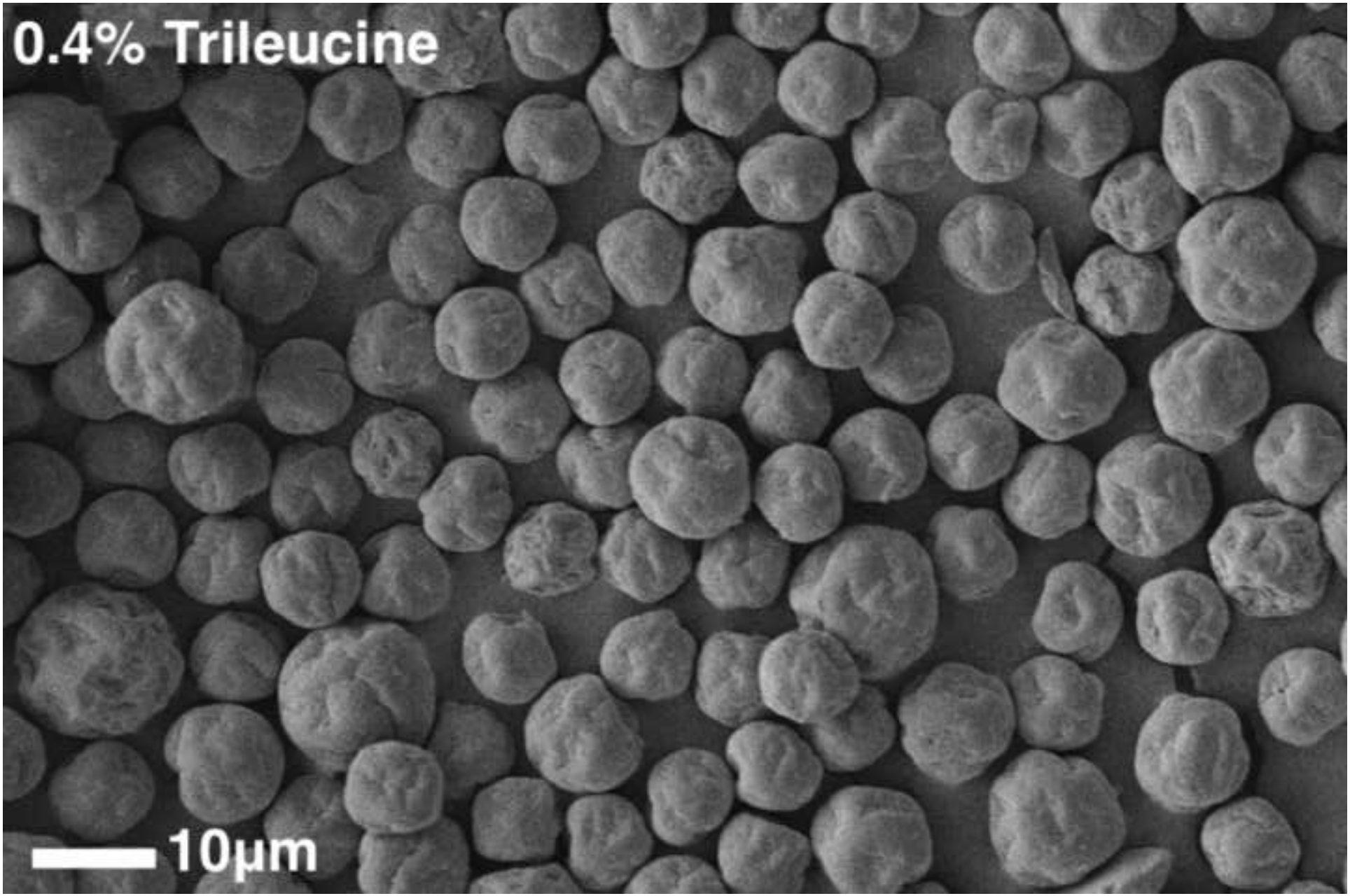

Click here to access/download;Figure;FIG03b2 - 0.4Tri-MedMag.tif

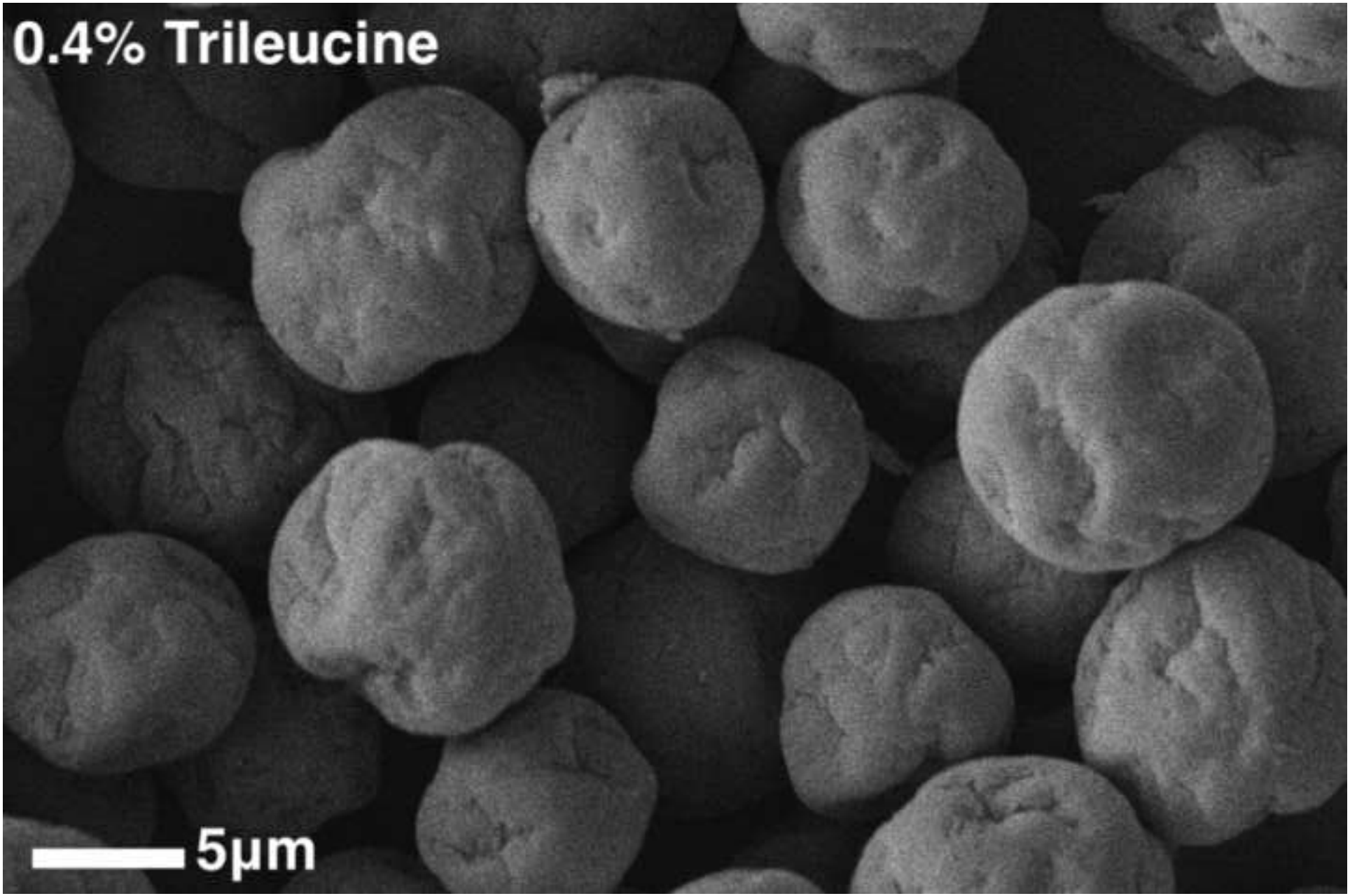

Click here to access/download;Figure;FIG03b3 - 0.4Tri-HighMag.tif

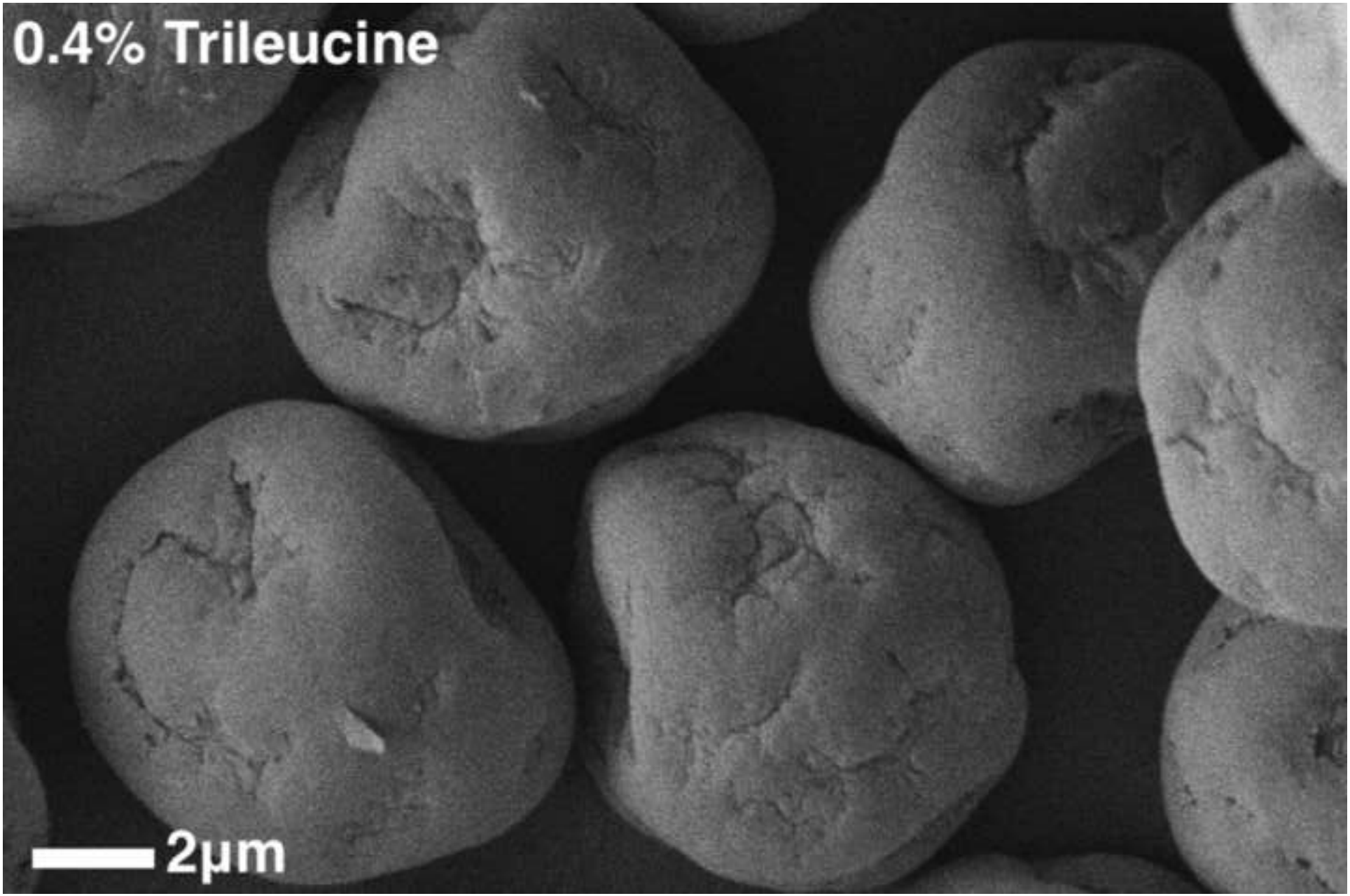

Click here to access/download;Figure;FIG03c1 - 1.0Tri-LowMag.tif

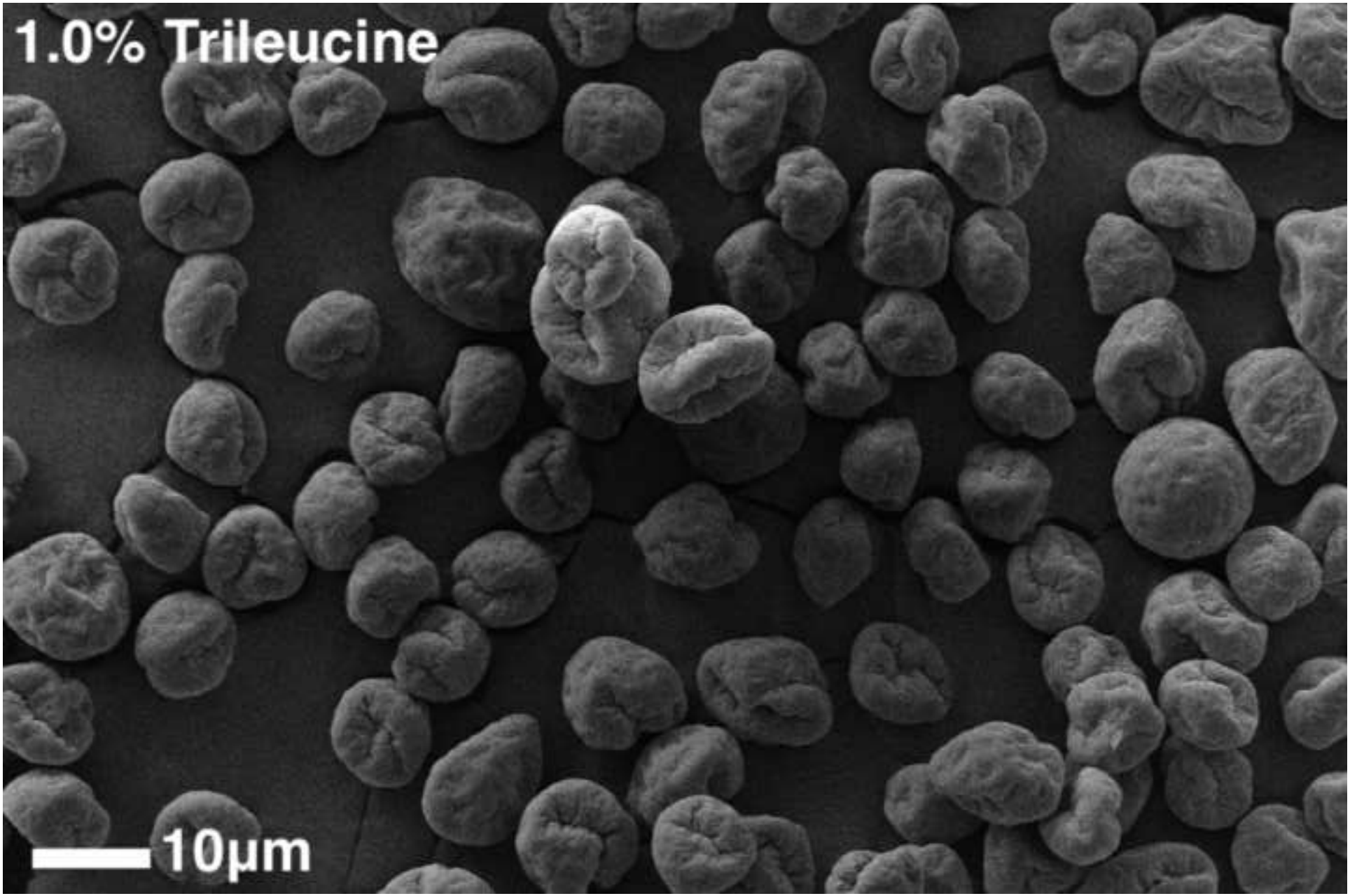

Click here to access/download;Figure;FIG03c2 - 1.0Tri-MedMag.tif

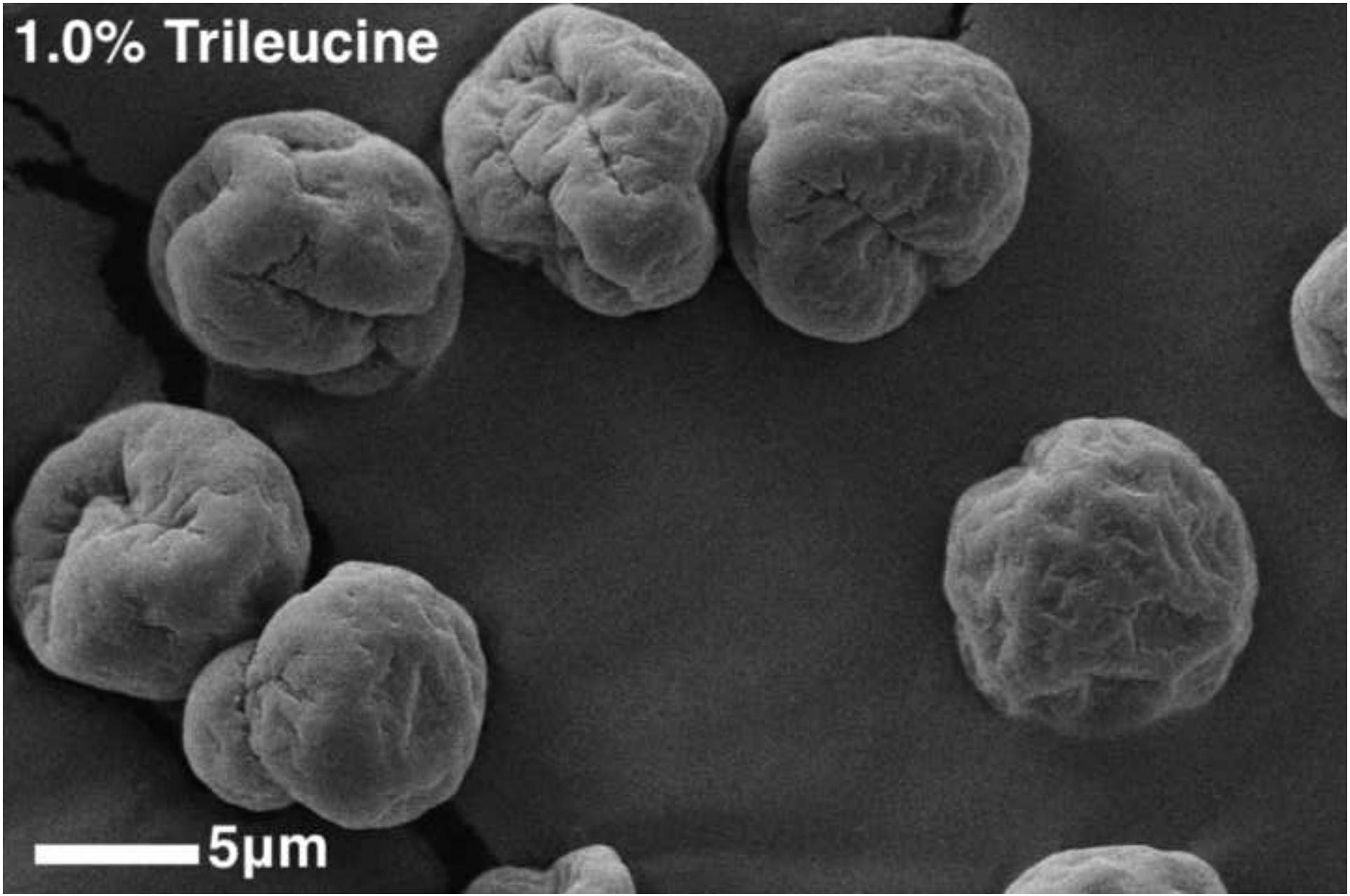

Click here to access/download;Figure;FIG03c3 - 1.0Tri-HighMag.tif

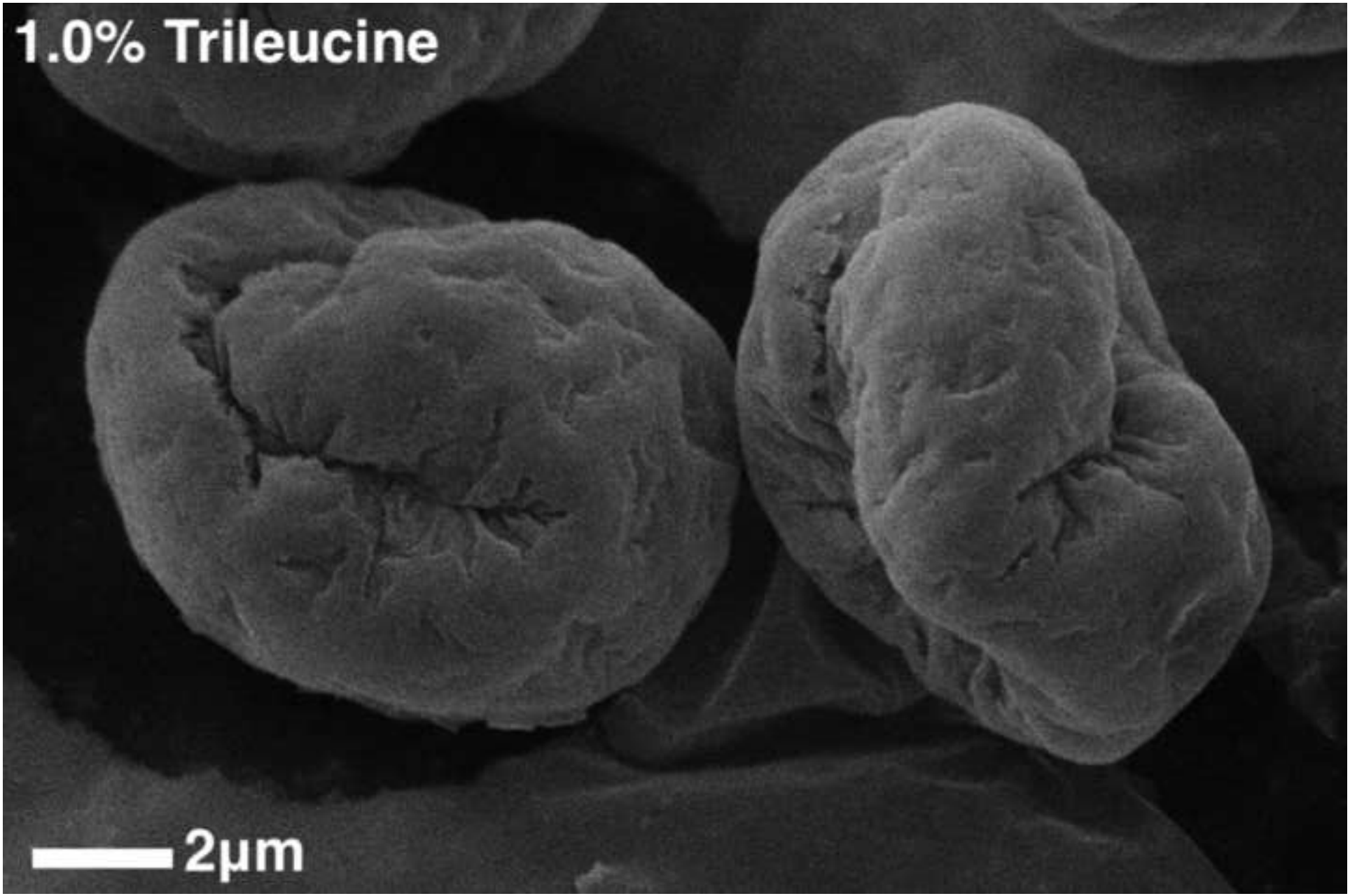

Click here to access/download;Figure;FIG03d1 - 5.0Tri-LowMag.tif

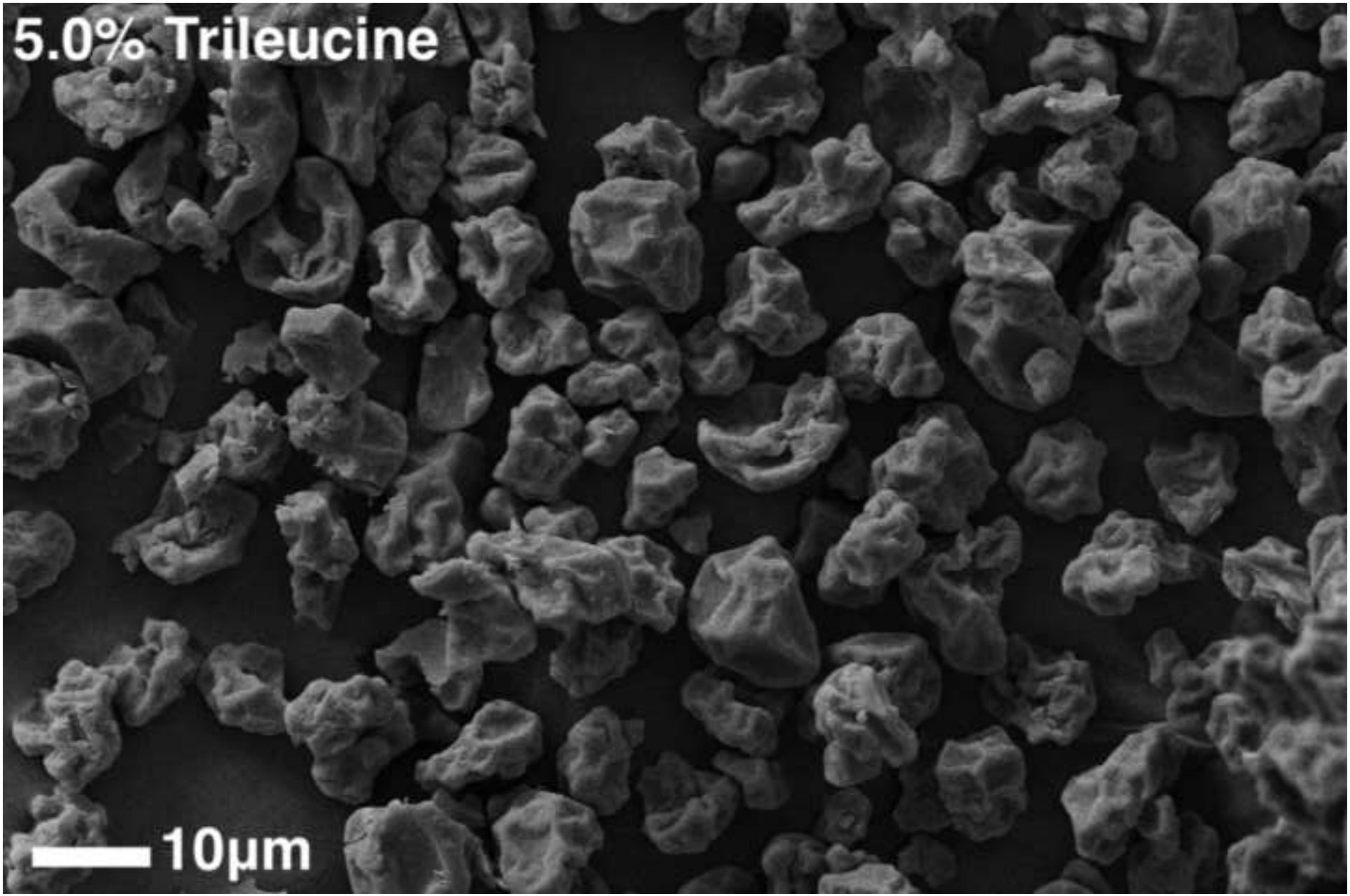

Click here to access/download;Figure;FIG03d2 - 5.0Tri-MedMag.tif

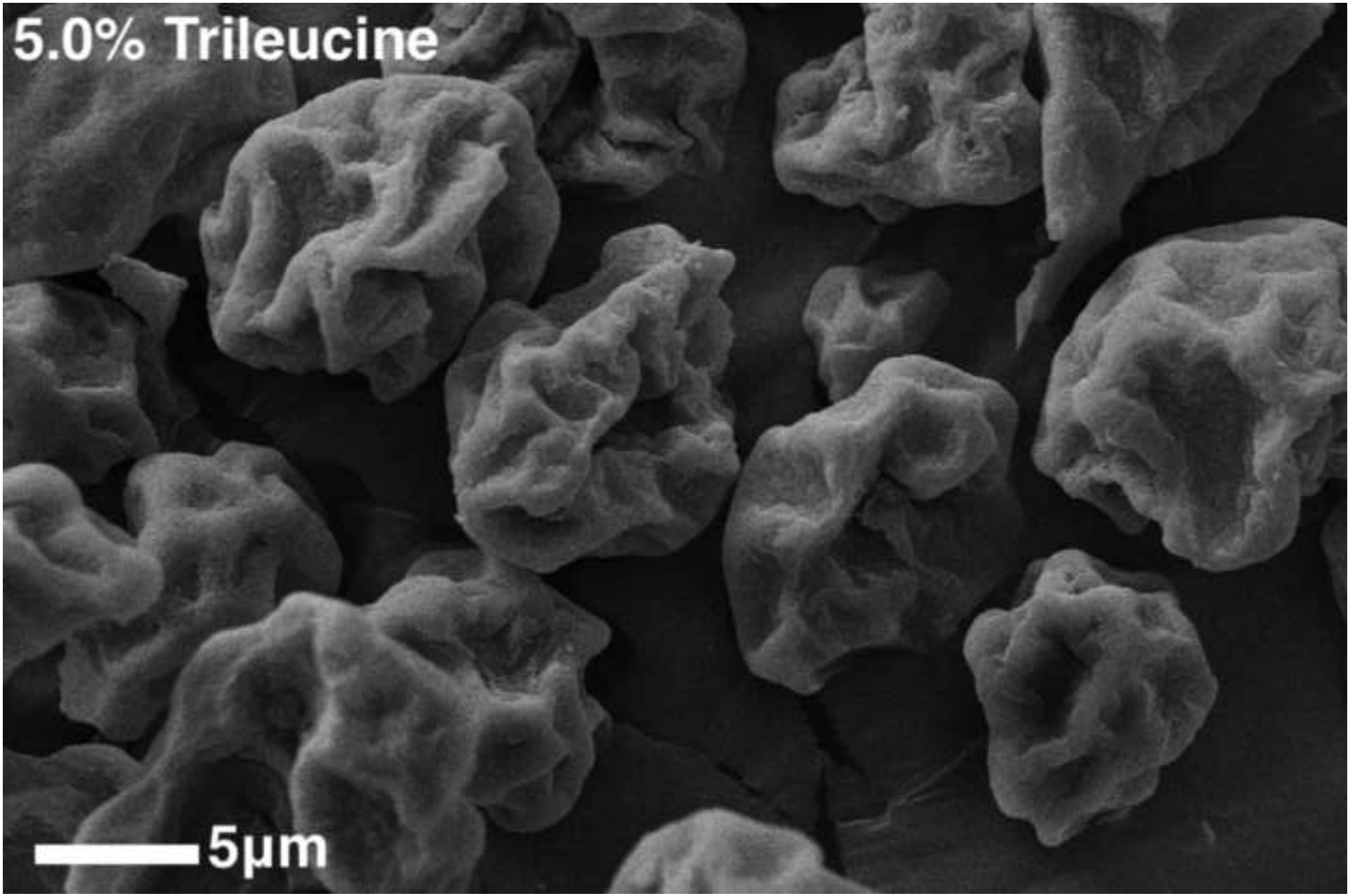

Click here to access/download;Figure;FIG03d3 - 5.0Tri-HighMag.tif

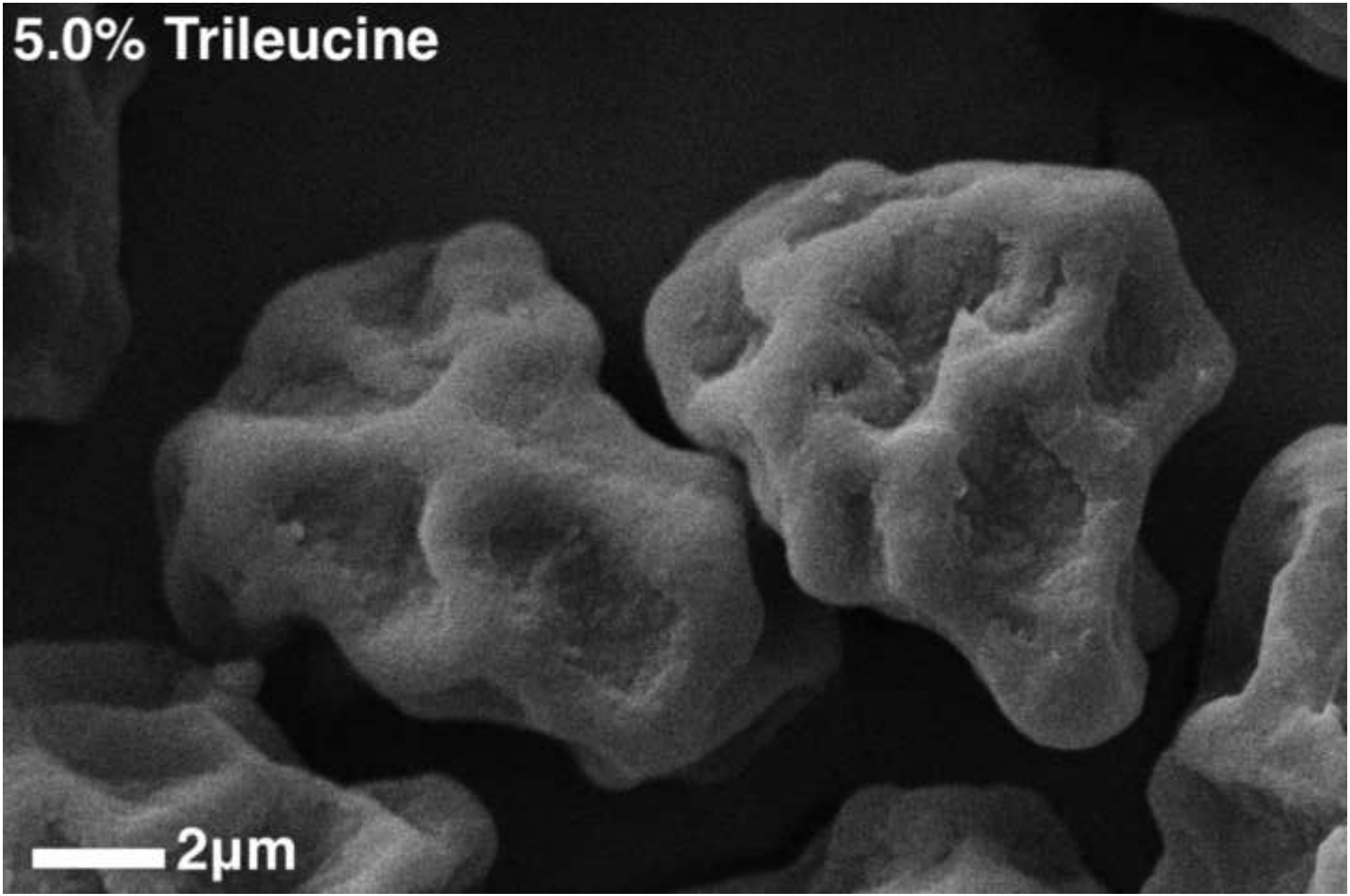

FIG04

Click here to access/download;Figure;FIG04 - Raman Spectra.tif

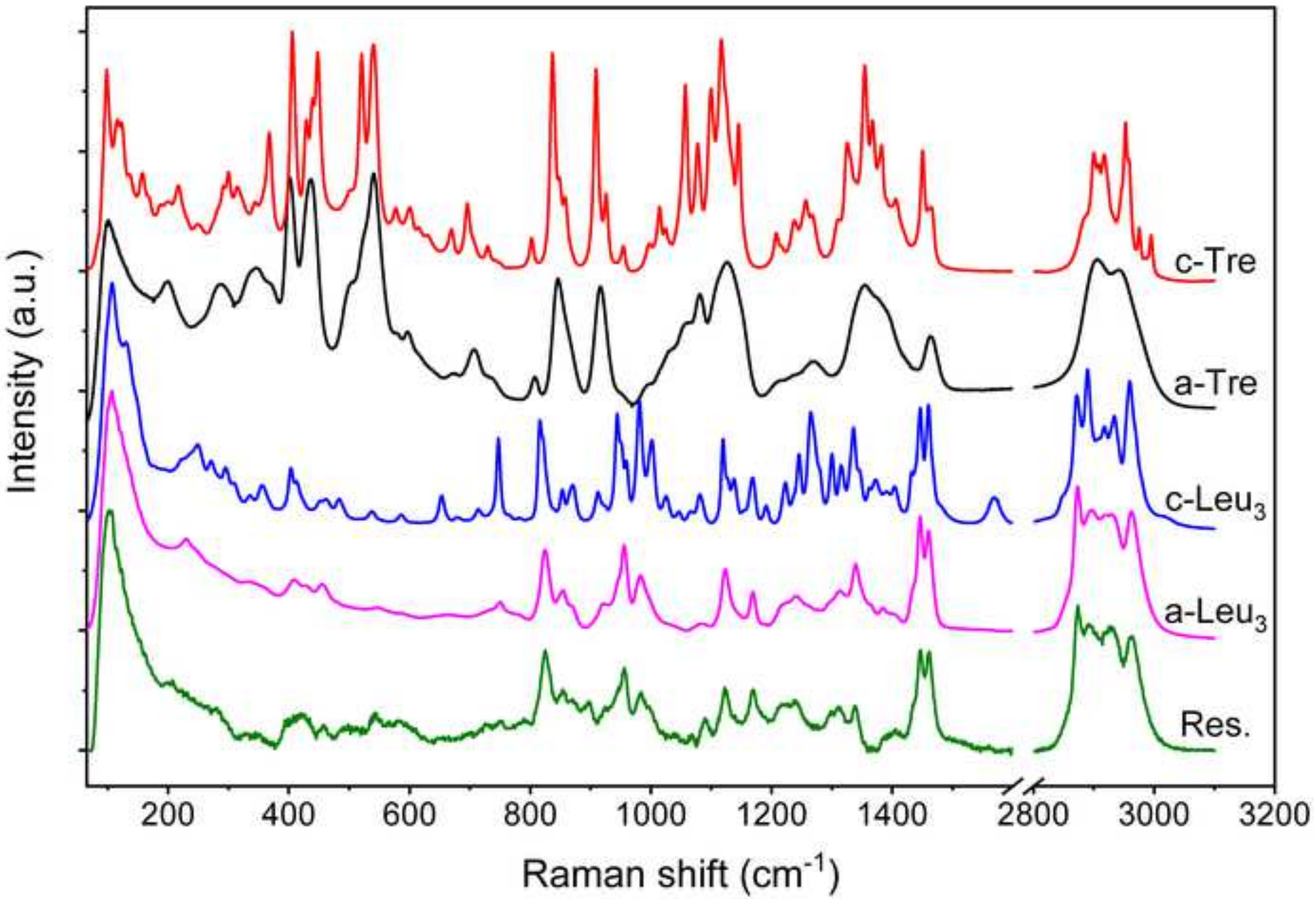

FIG05

Click here to access/download;Figure;FIG05 - Trehalose-MMAD.tif

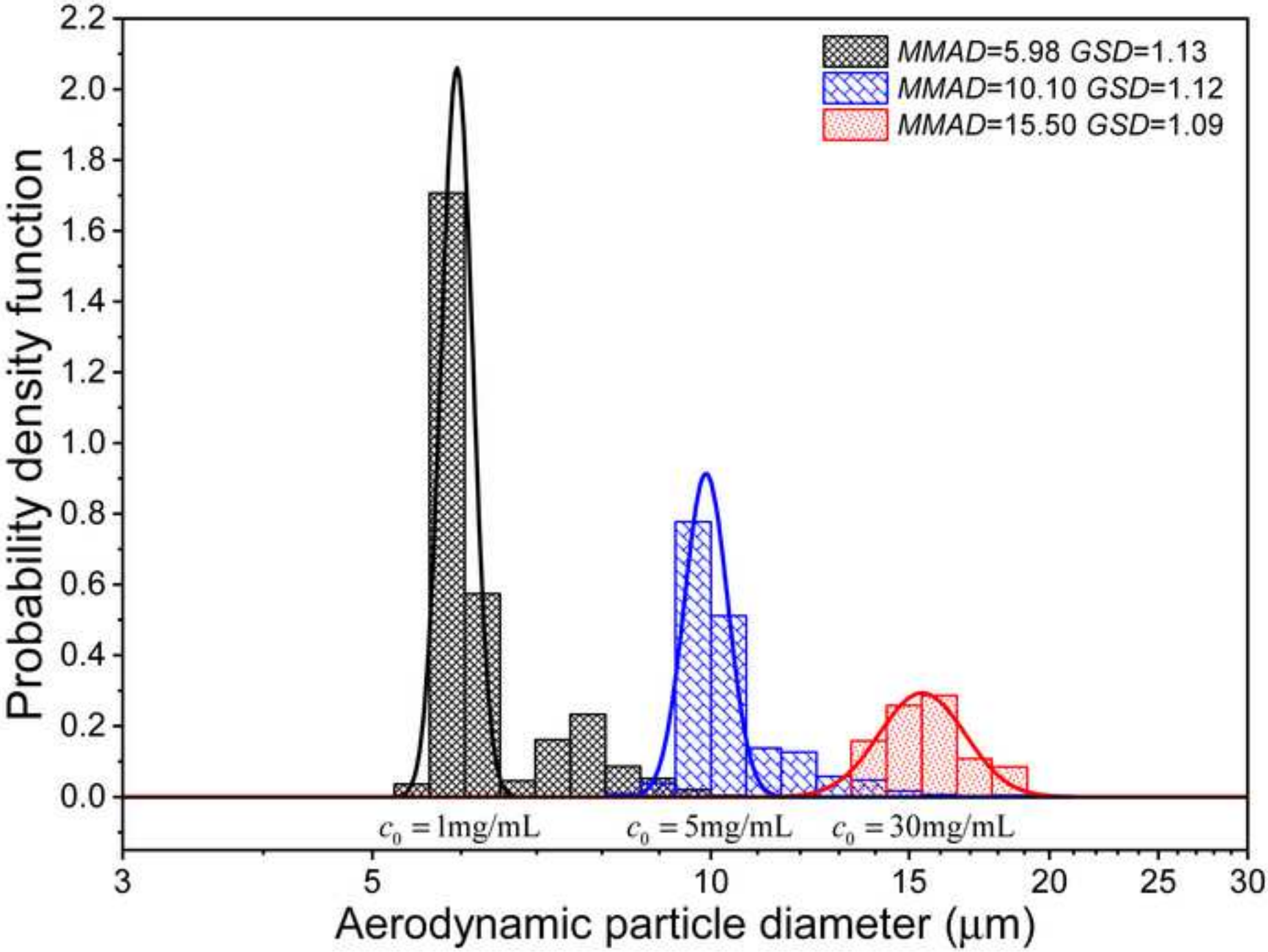

FIG06

Click here to access/download;Figure;FIG06 - Trehalose-dve.tif

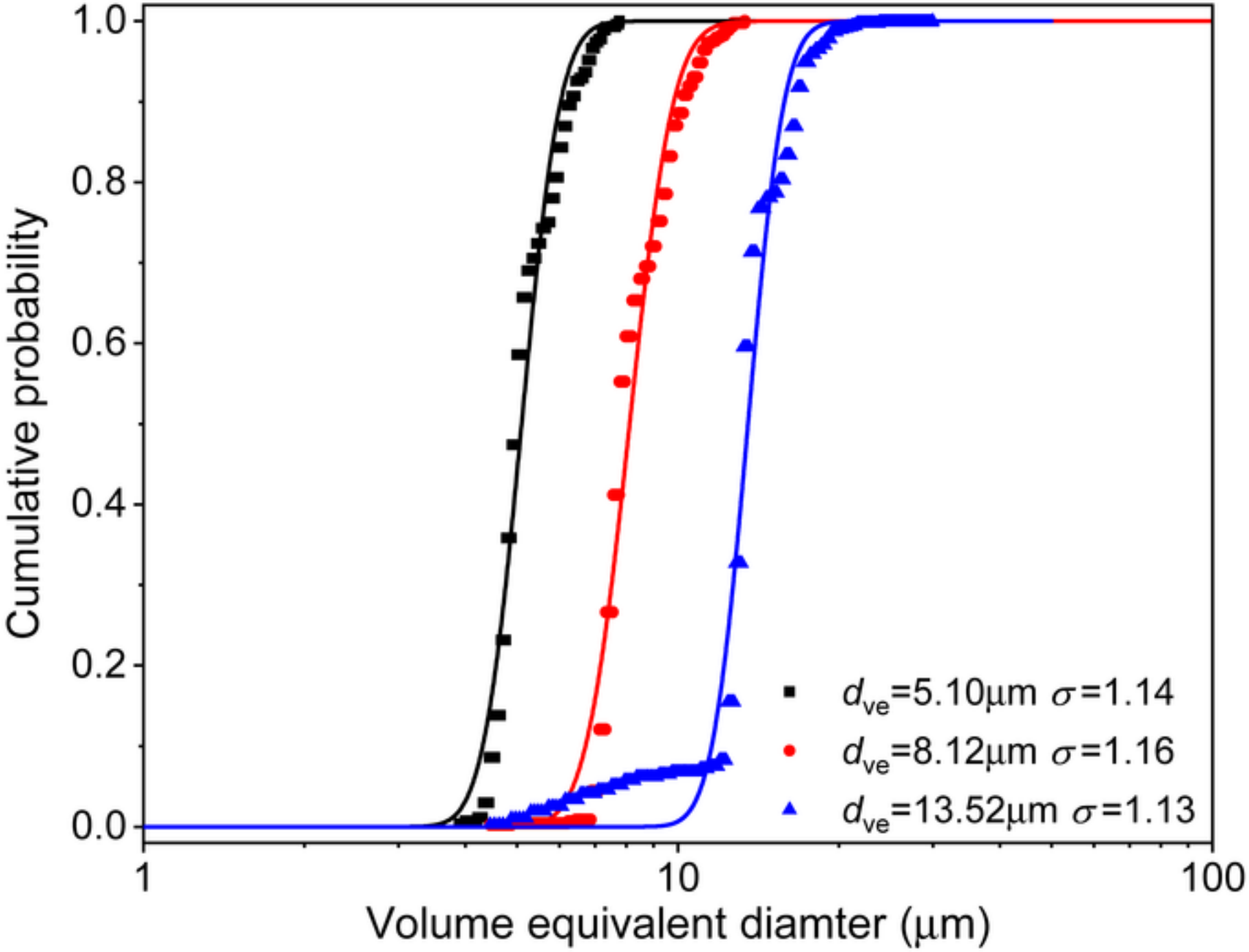

FIG07

Click here to access/download;Figure;FIG07 - Trehalose-Trileucine PSD.tif

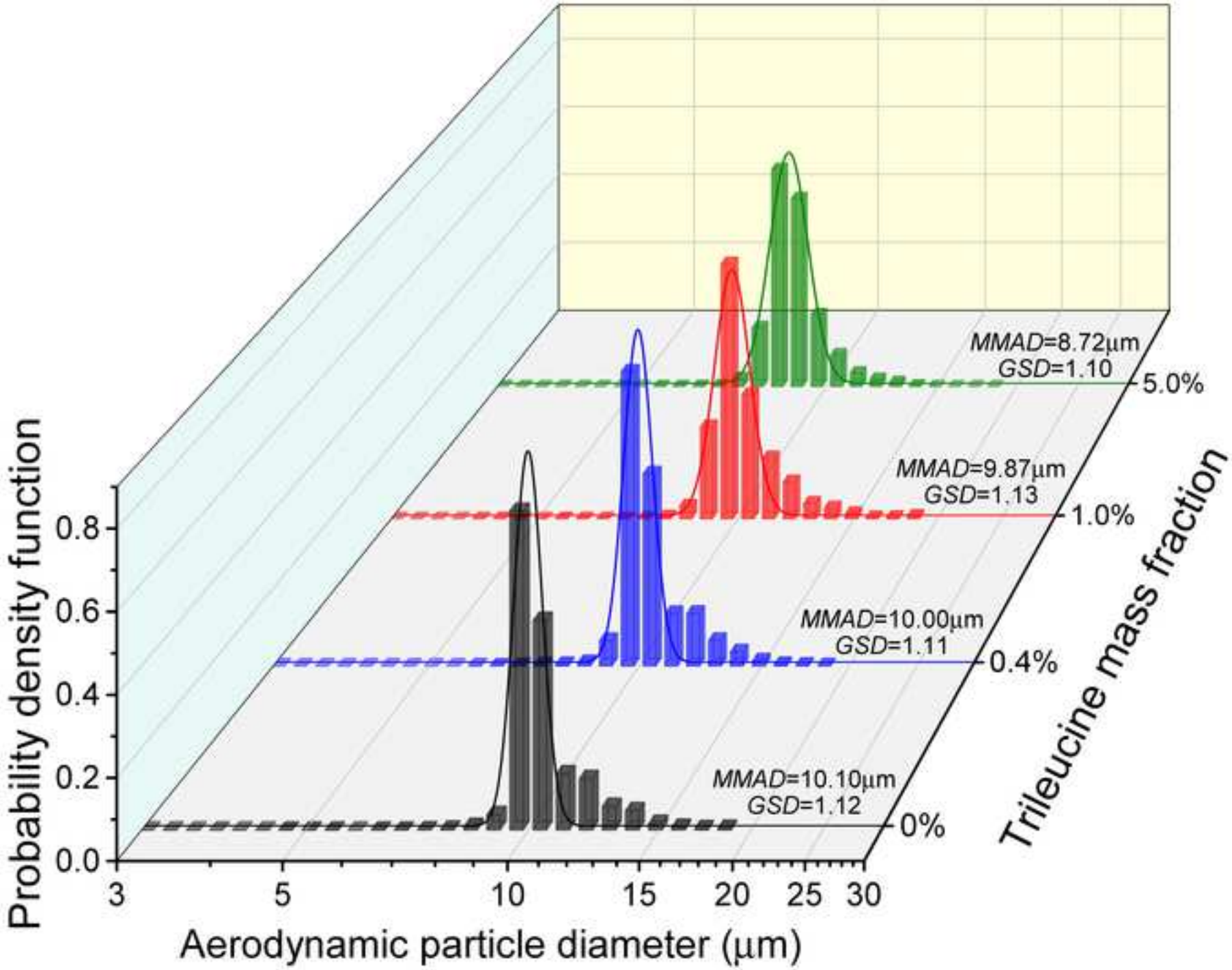

FIG08

Click here to access/download;Figure;FIG08 - Surface rugosity.tiff

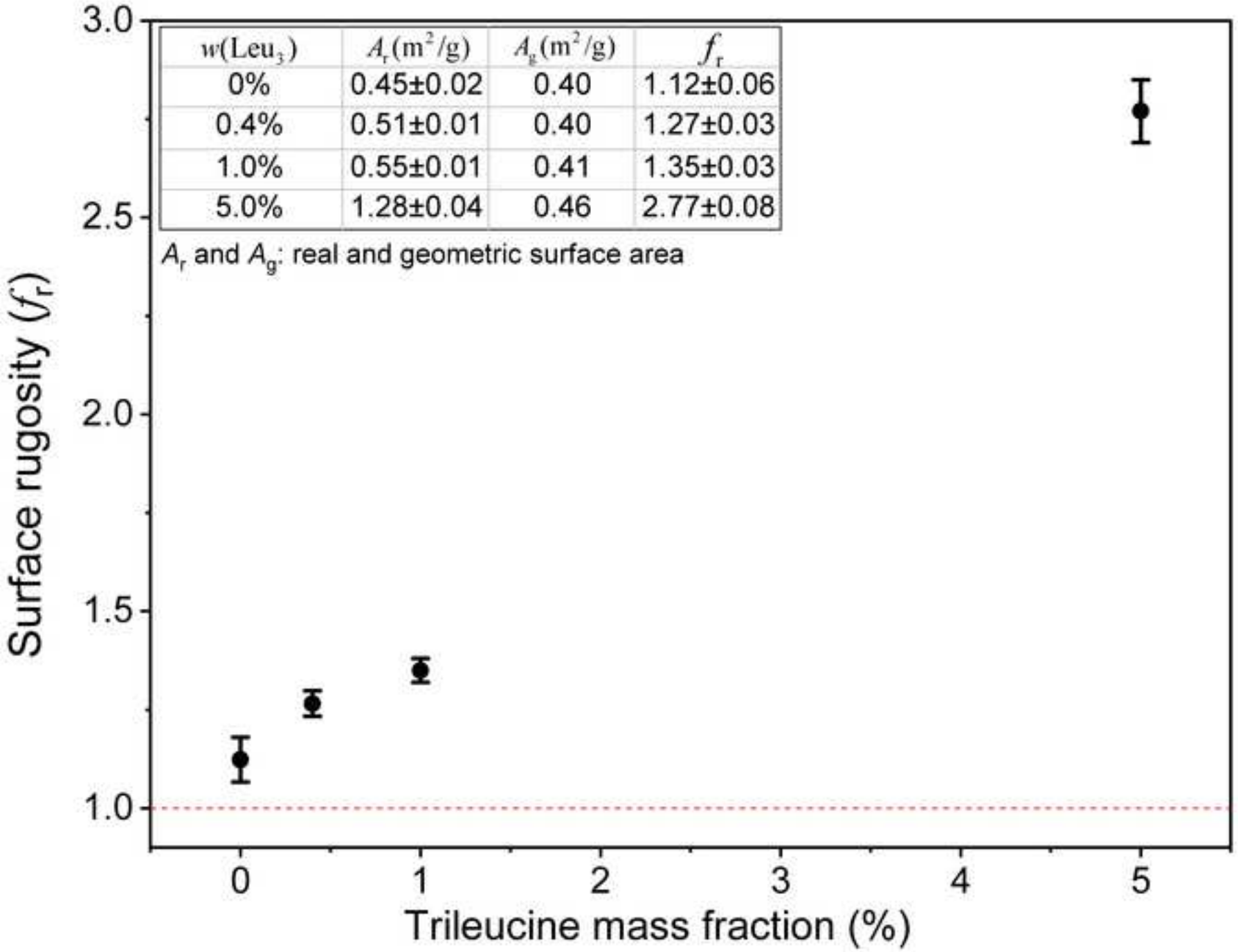

$w(Leu_3)$	A_r (m^2/g)	A_g (m^2/g)	f_r
0%	0.45±0.02	0.40	1.12±0.06
0.4%	0.51±0.01	0.40	1.27±0.03
1.0%	0.55±0.01	0.41	1.35±0.03
5.0%	1.28±0.04	0.46	2.77±0.08

A_r and A_g: real and geometric surface area

FIG09

Click here to access/download;Figure;FIG09 - Trehalose MMAD-NRTP.tiff

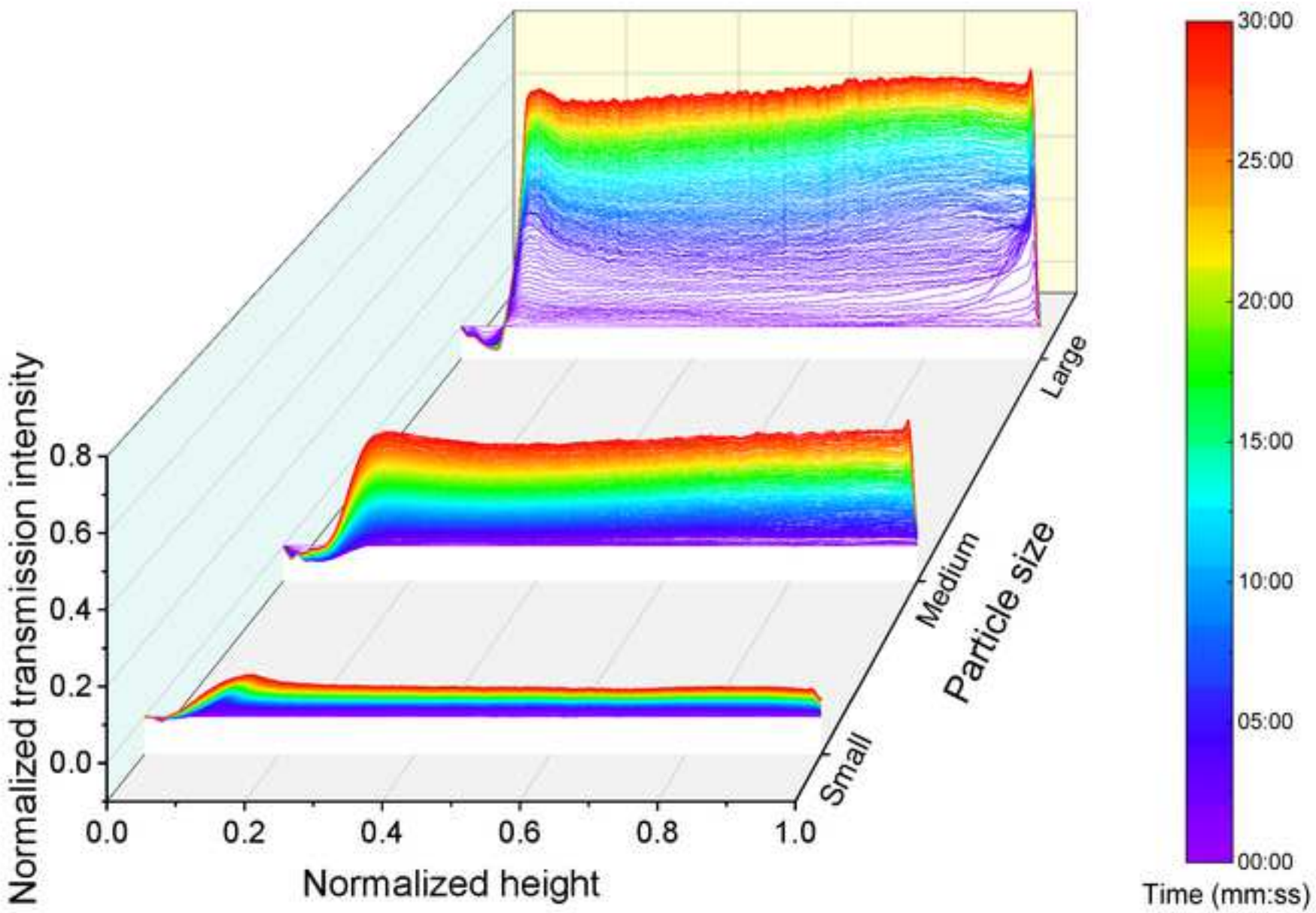

FIG10

Click here to access/download;Figure;FIG10 - MMAD Dependent IS.tif

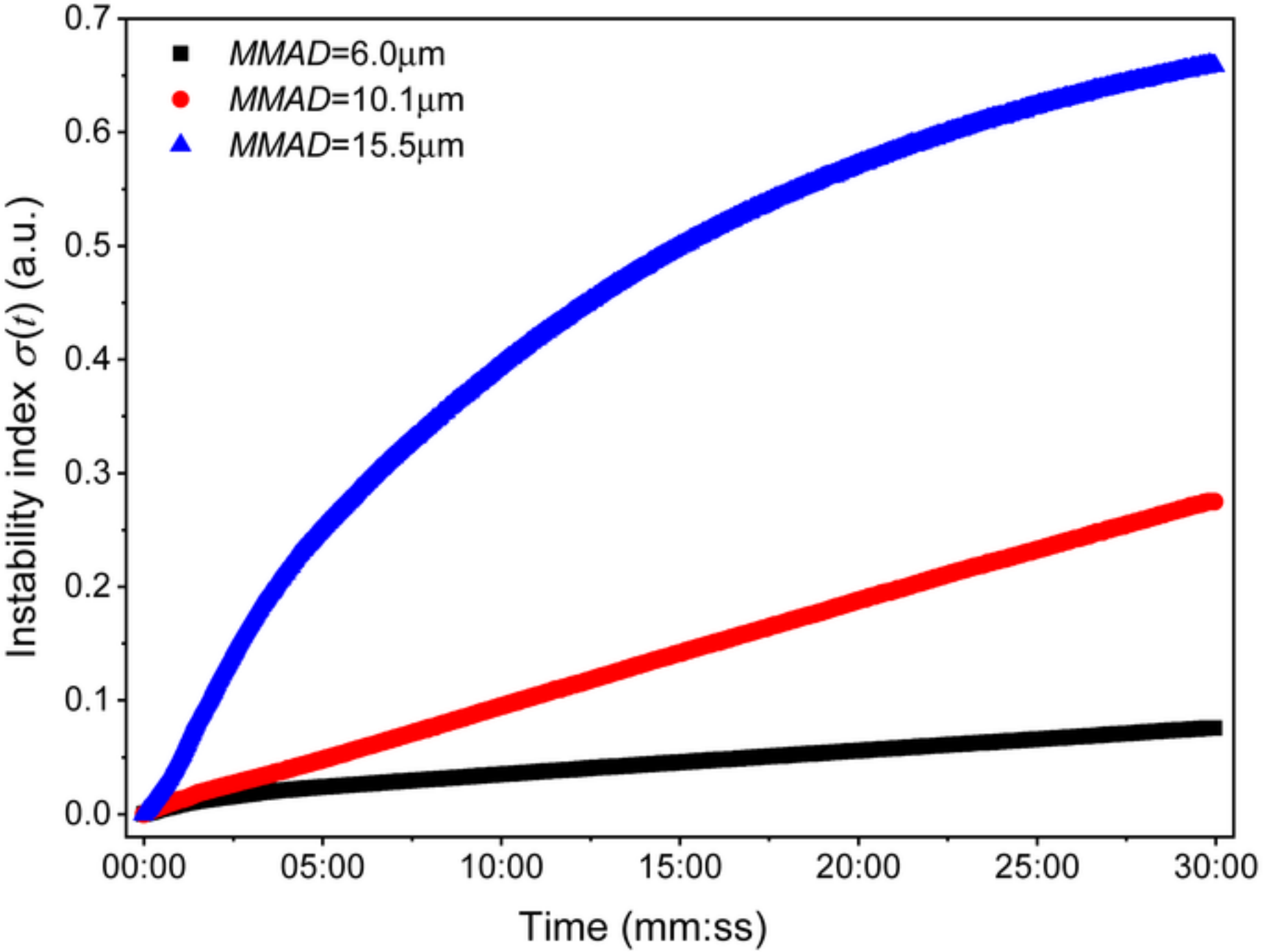

FIG11

Click here to access/download;Figure;FIG11 - MMAD-30min IS.tif

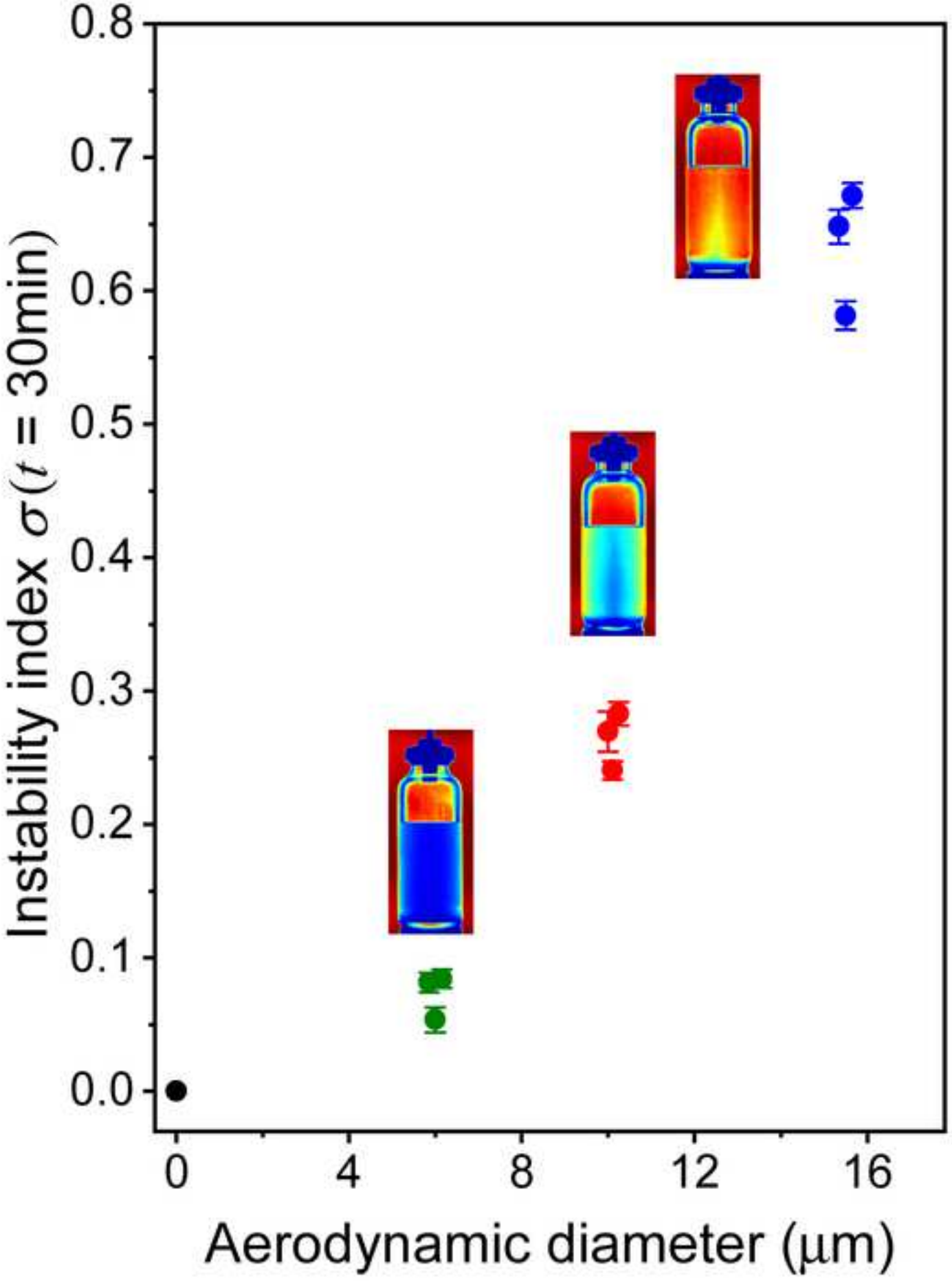

FIG12

Click here to access/download;Figure;FIG12 - Trileucine Fraction-NRTP.tiff

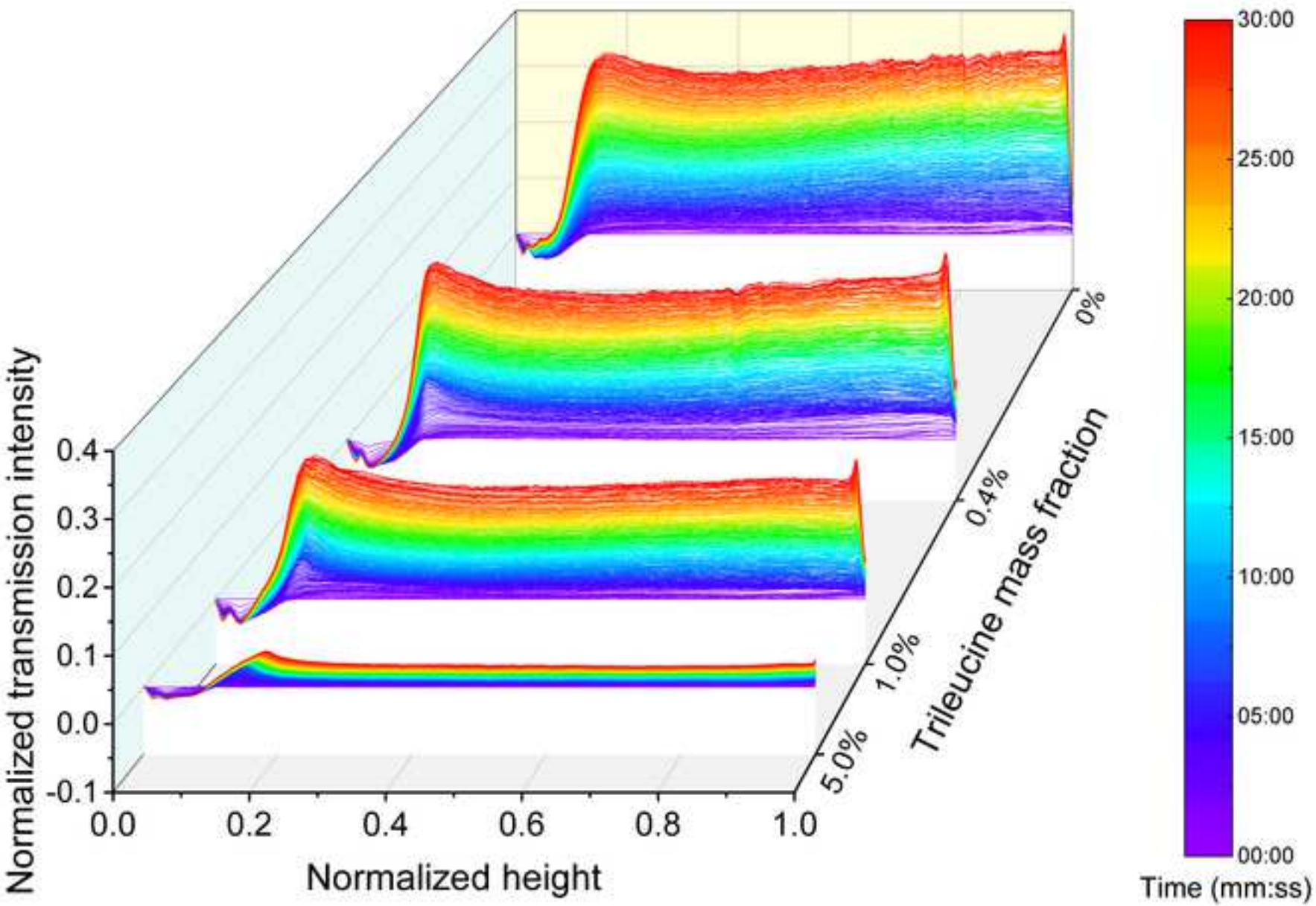

FIG13

Click here to access/download;Figure;FIG13 - Trileucine Dependent IS.tif

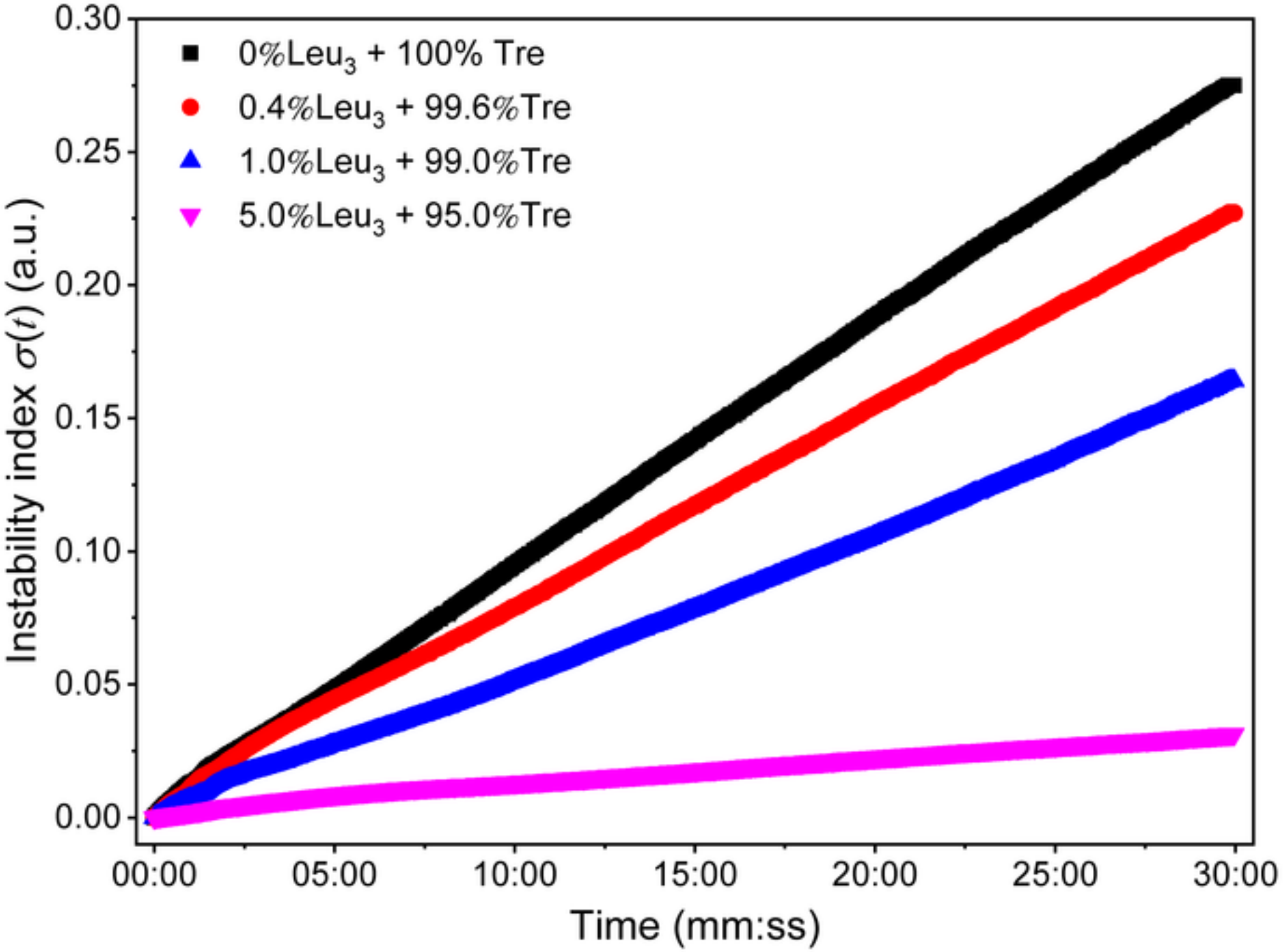

FIG14

Click here to access/download;Figure;FIG14 - Trileucine-30min IS.tif

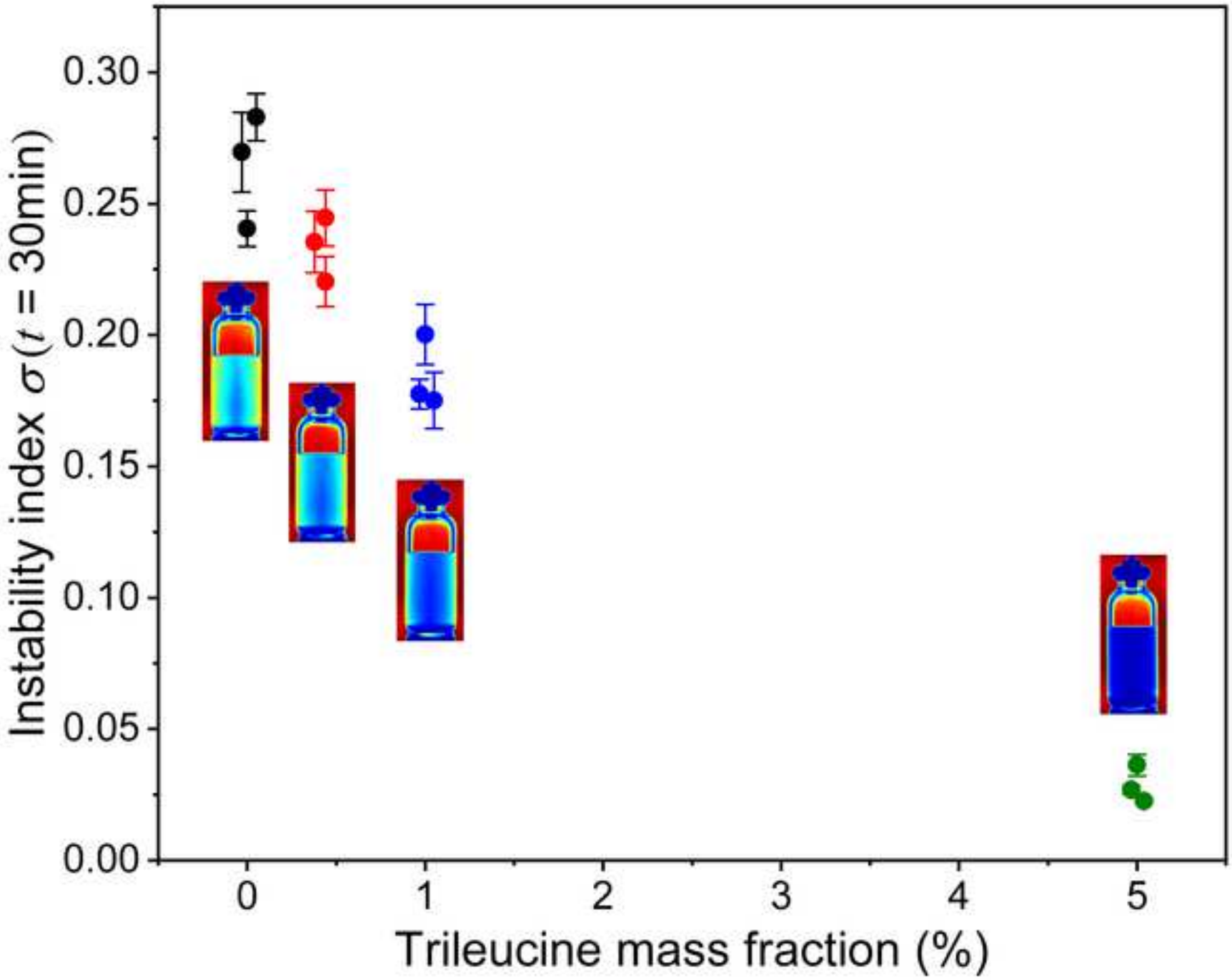

FIG-A1

Click here to access/download;Figure;FIGA1 - Adsorption isotherm.tiff

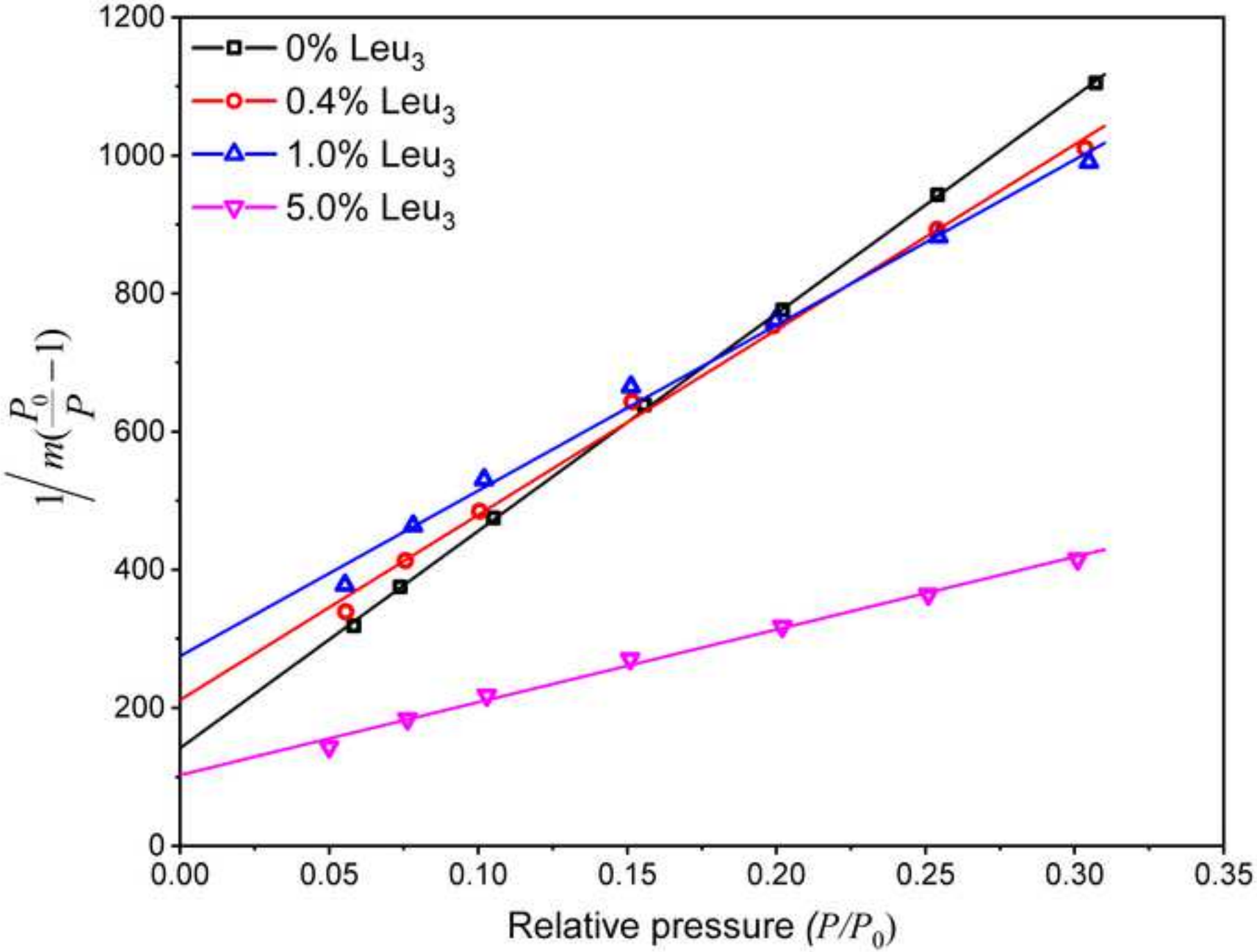

Click here to access/download;Figure;FIG-A2(a1) - Tre-LowMag.tif

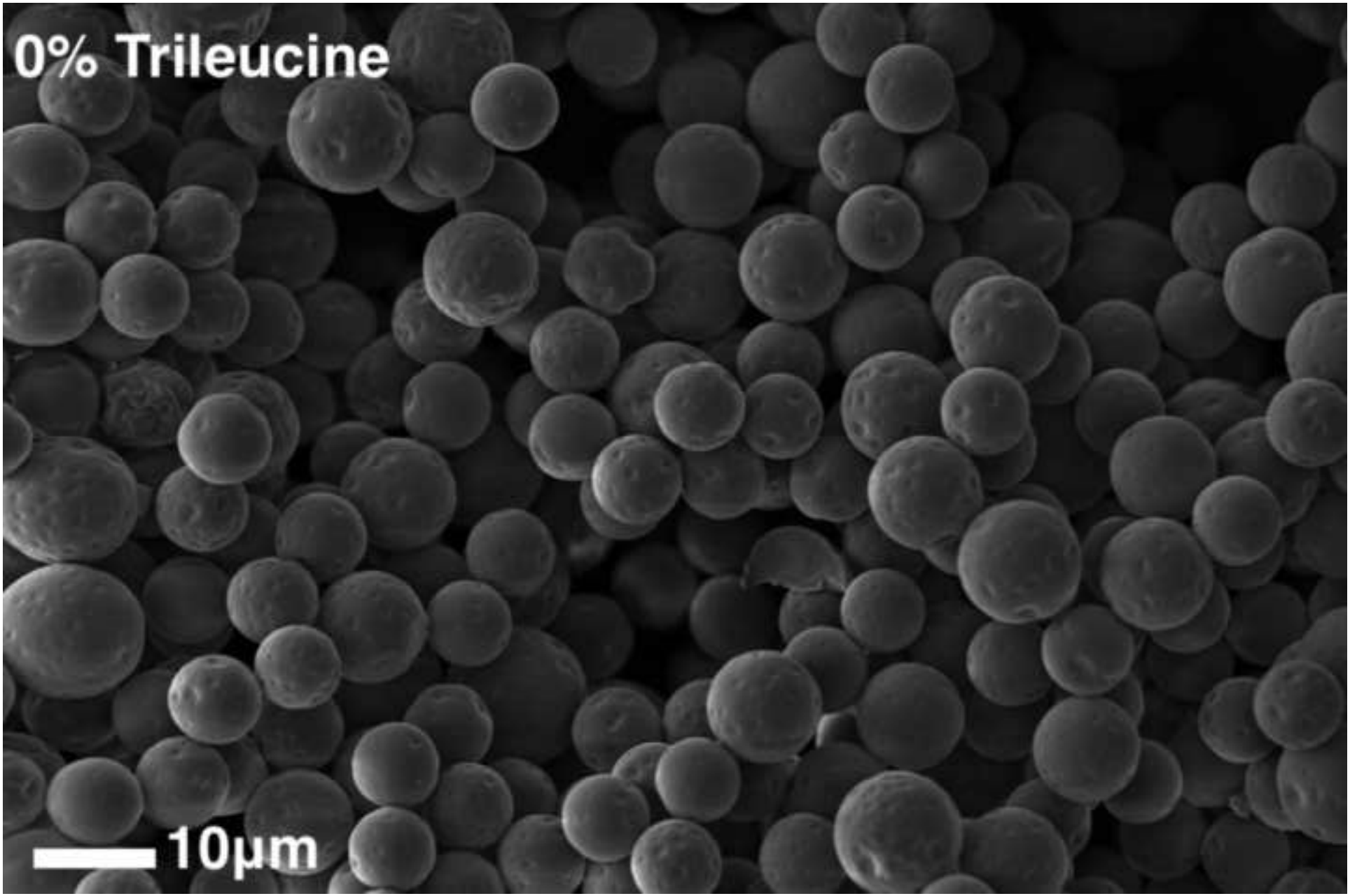

Click here to access/download;Figure;FIG-A2(a2) - Tre-HighMag.tif

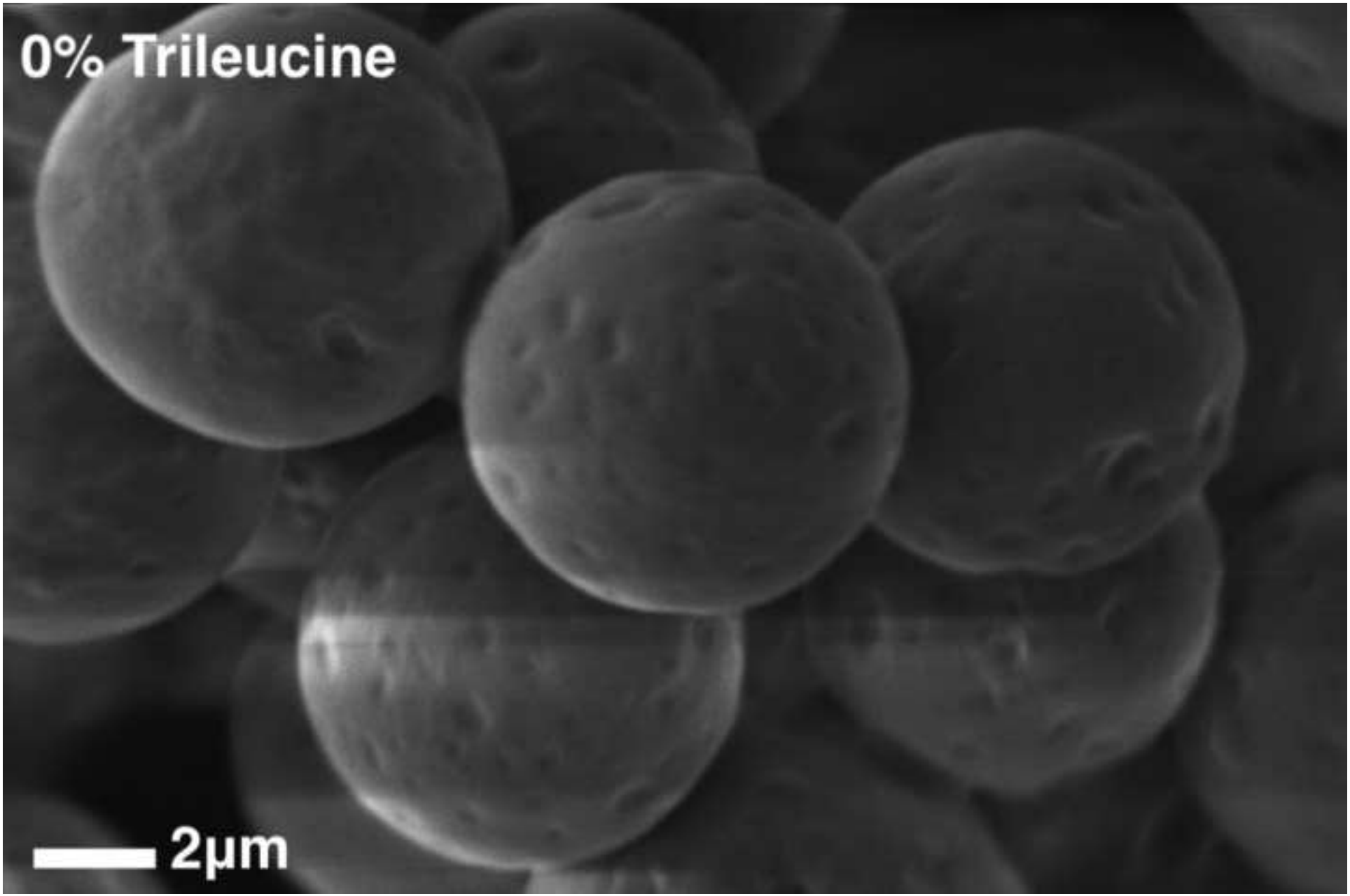

Click here to access/download;Figure;FIG-A2(b1) - 0.4Tri-LowMag.tif

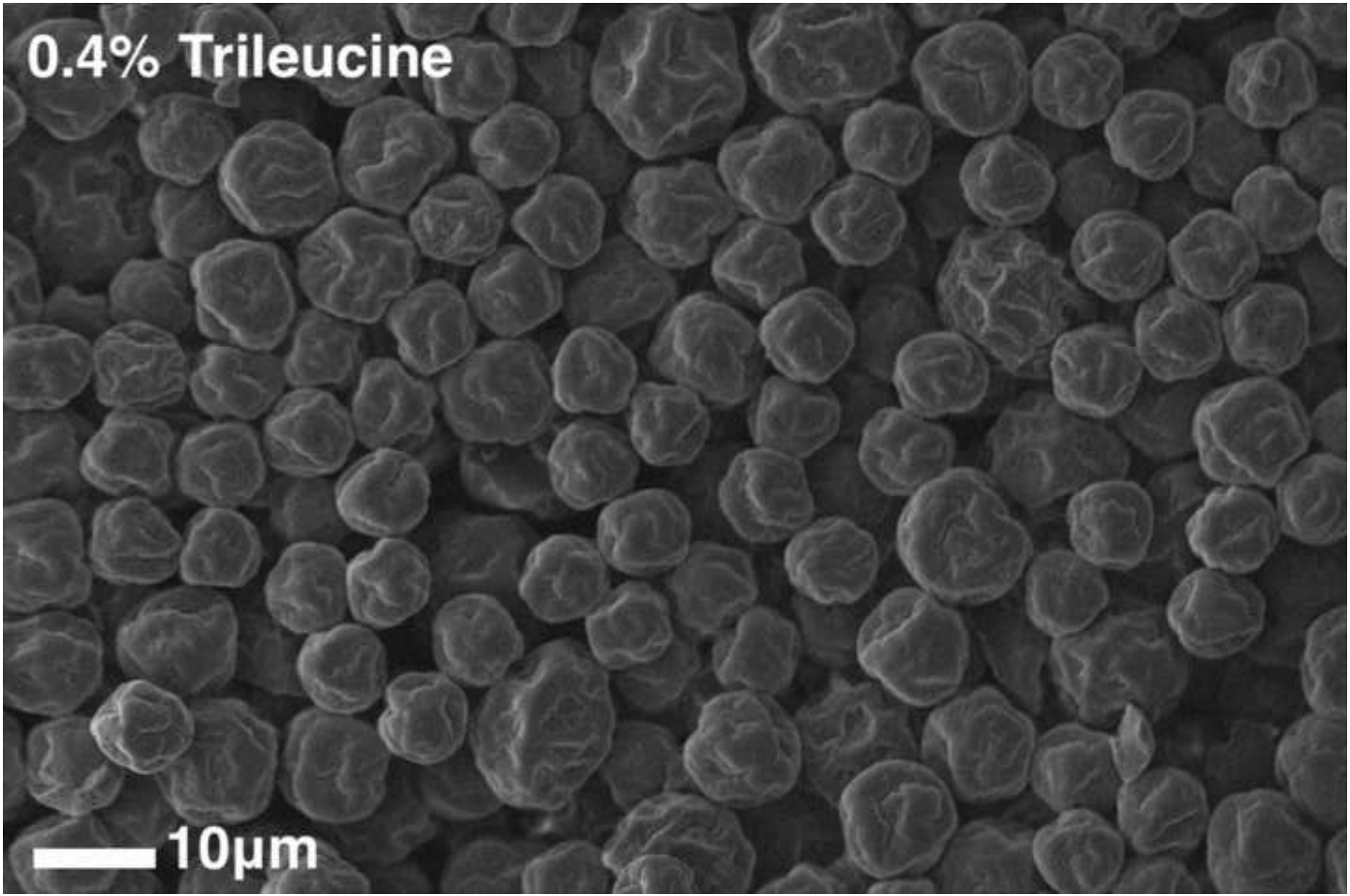

Click here to access/download;Figure;FIG-A2(b2) - 0.4Tri-HighMag.tif

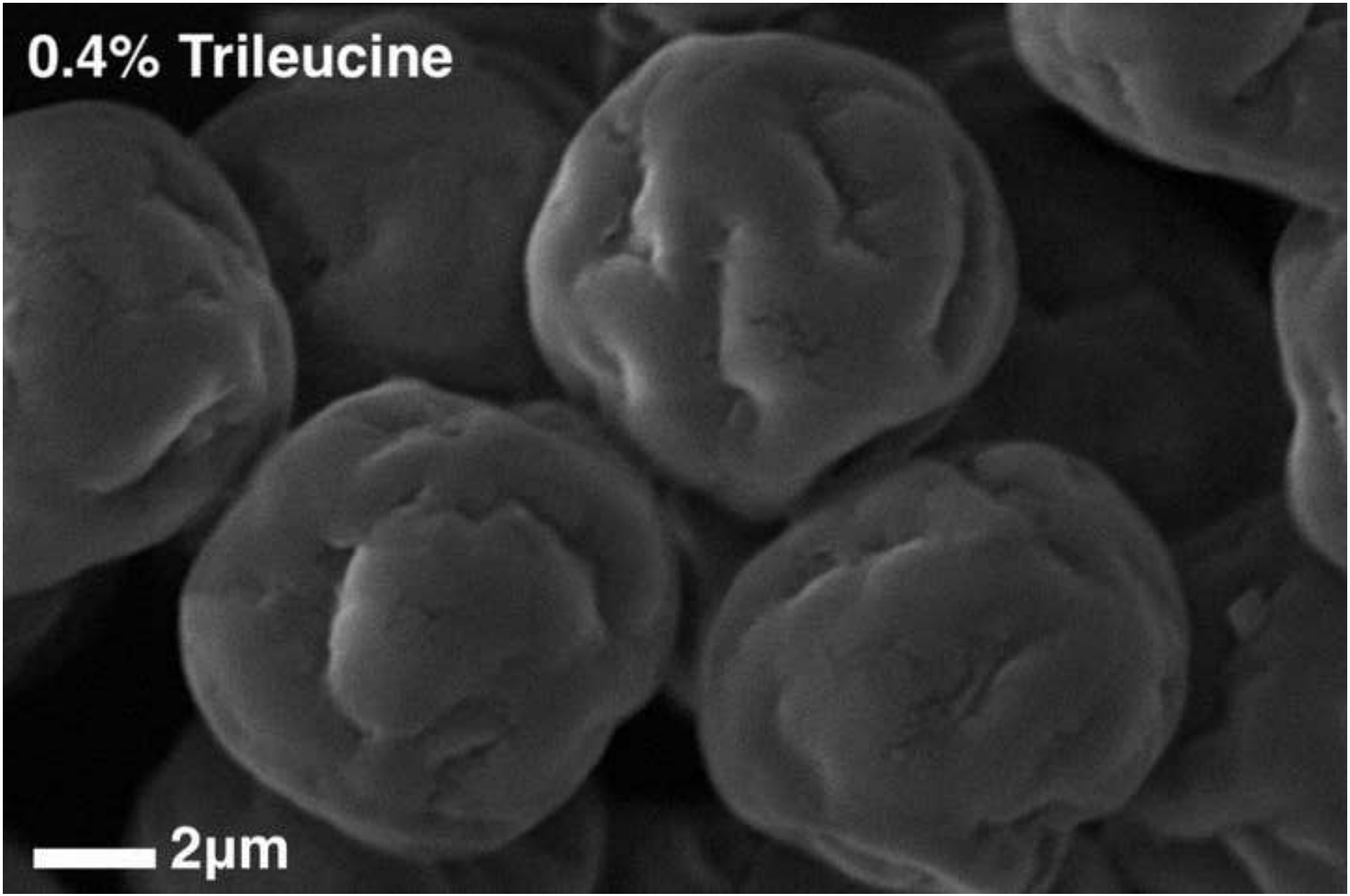

Click here to access/download;Figure;FIG-A2(c1) - 1.0Tri-LowMag.tif

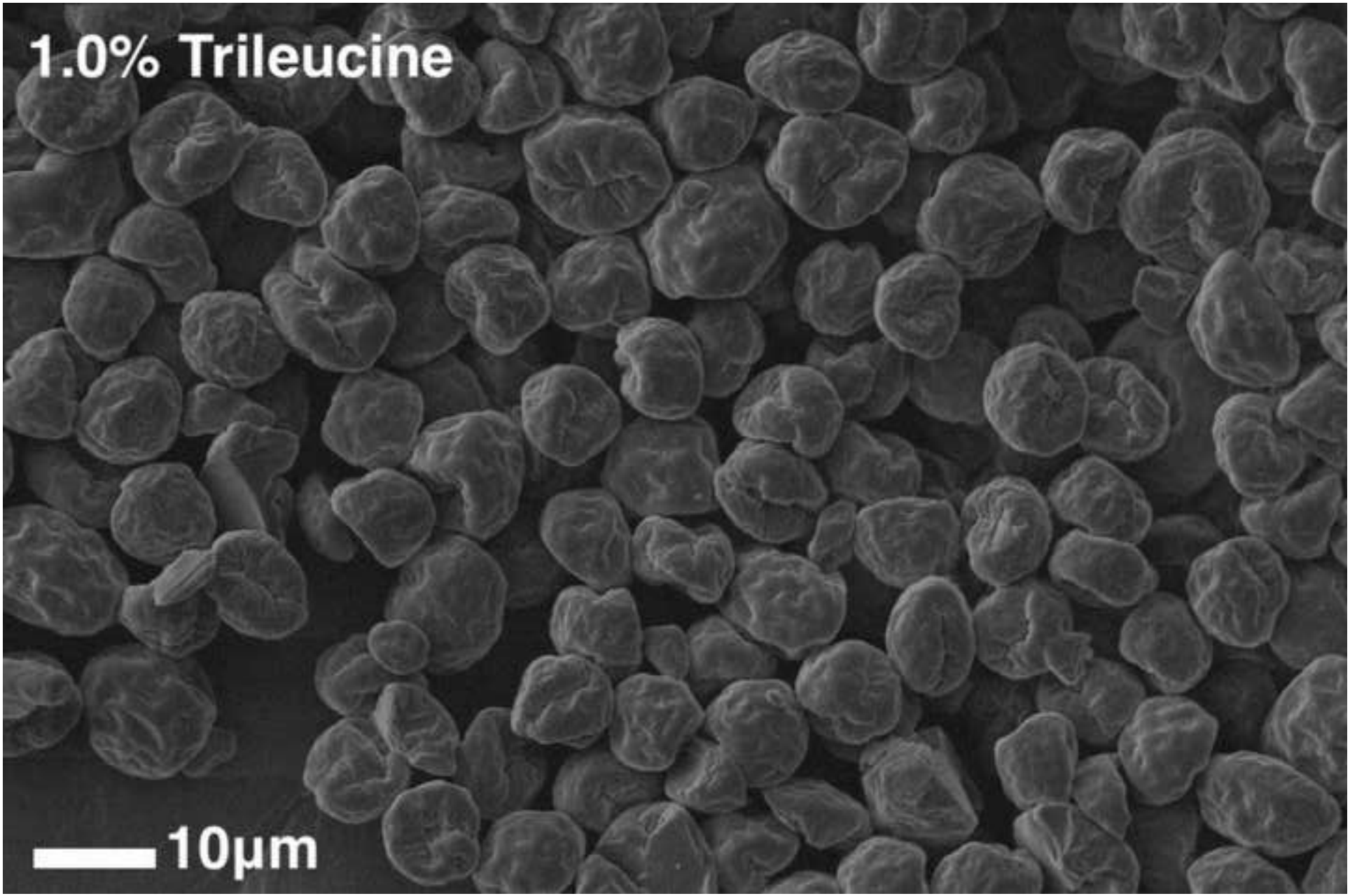

Click here to access/download;Figure;FIG-A2(c2) - 1.0Tri-HighMag.tif

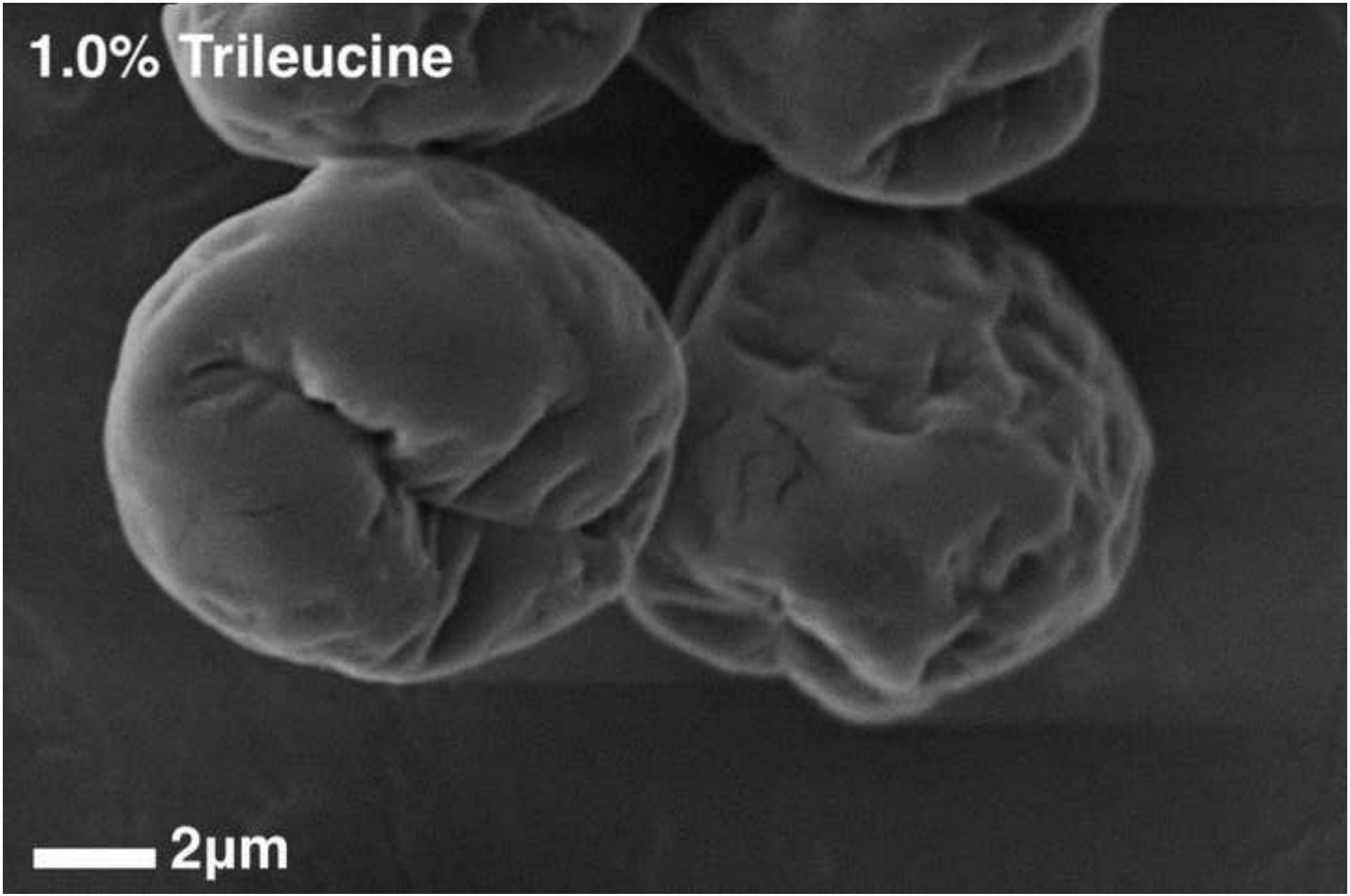

Click here to access/download;Figure;FIG-A2(d1) - 5.0Tri-LowMag.tif

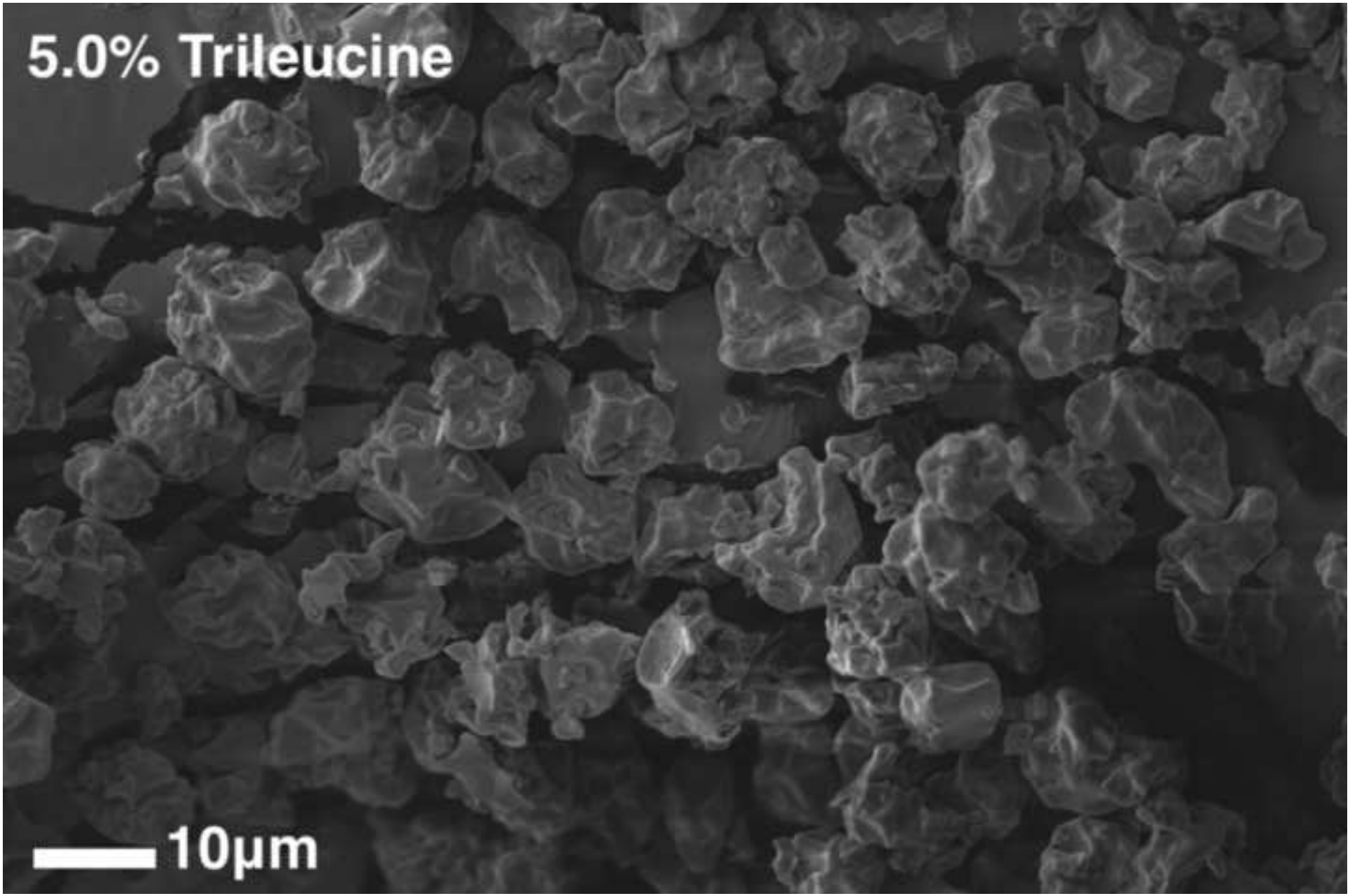

Click here to access/download;Figure;FIG-A2(d2) - 5.0Tri-HighMag.tif